Evaluation of Fracture Properties of Additively Manufactured IN-718 Under Quasi-static and Dynamic Loading Conditions

by

Alex K. Edwards

A thesis submitted to the Graduate Faculty of
Auburn University
in partial fulfillment of the
requirements for the Degree of
Master of Science

Auburn, Alabama
May 10, 2025

Keywords: Inconel-718, Digital Image Correlation, Fracture Mechanics, Additive Manufacturing, Impact Loading

Approved by

Dr. Hareesh Tippur, Chair, McWane Chair Professor of Mechanical Engineering
Dr. Jeffery Suhling, Department Chair of Mechanical Engineering
Dr. Shuai Shao, McWane Associate Professor Mechanical Engineering

Abstract

Inconel 718 is a Nickel based alloy with many applications in the aerospace and automotive industries. Due to its high strength under intense heat, IN-718 is used in extreme environments such as rocket engine manifolds and automobile exhaust systems. The focus of this work is on the fracture behavior of additively printed IN-718. Edge notched three-point bending specimens are additively manufactured using laser powder bed fusion (LPBF) and mechanically tested to evaluate the fracture performance under quasi-static and dynamic loading. Several combinations of laser process parameter, heat treatment, and shielding gas are used during manufacturing. The grain size in the microstructure can be affected by the heat treatment and the shielding gas used. Two different heat treatment procedures will be used along with two different shielding gases, namely argon (A) and nitrogen (N) gas. The laser process parameter can introduce defects into 3D printed parts. An underpowered laser causes lack of fusion (LoF) defects to occur at a higher rate, and an overpowered laser causes keyhole (KH) defects to occur at a higher rate. Three laser process parameters, one to induce more LoF defects, one to induce more KH defects, and a middle powered "recommended" (R) laser parameter not meant to induce either kind of defect, are used. Electrical discharge machining (EDM) is used to cut a crack-like notch into the edge of the specimens. A pair of EDM cut side grooves is added to the front and back surfaces along the uncracked ligament to constrain the crack growth to occur self-similarly, reduce crack tunneling effects, and suppress shear lip formation. A random speckle pattern is applied to the specimens to allow for implementing digital image correlation

(DIC)—a full-field optical technique—to measure surface deformation fields during fracture. The fracture behavior of the specimens are evaluated by conducting quasi-static and dynamic fracture experiments. Under quasi-static loading, notched three-point bend specimens are slowly loaded until the crack initiates and grows. The surface deformation are simultaneously measured by DIC. To evaluate the fracture behavior of IN-718 under dynamic loading, similarly notched three-point bend specimens are tested using a split-Hopkinson pressure bar (SHPB) apparatus to rapidly load the specimen while implementing DIC for full-field deformation measurements. The fracture event is recorded using an ultrahigh-speed camera at 400,000 frames per second. In both quasi-static and dynamic experiments, images are analyzed using DIC to measure surface displacement fields. The Energy release rate (ERR) is extracted at each load-step or time-step by computing the *J*-Integral using a hybrid DIC-Finite Element (DIC-FE) method. The methodology is applicable to both quasi-static and high strain-rate experiments and accounts for elastoplastic stress-strain behavior in the material. A modified least-squares analysis of the measured surface displacements is also used to evaluate stress intensity factors in the elastic range to further validate the DIC-FE approach. In this case, the DIC-FE method is found to be more robust than the elastic least squares method and allows for the evaluation of fracture properties beyond the point of fracture. Results for the quasi-static specimens are validated with a complementary finite element solution. It is found that the strongest manufacturing conditions are those which used argon shielding gas and heat treatment 1. The highest quasi-static critical ERR is 163.1 N/mm for the A1K (shielding gas of argon, heat treatment 1,

keyhole defects) condition. The lowest is 46.9 N/mm for the N2K (shielding gas of nitrogen, heat treatment 2, keyhole defects) condition. This pattern is found to be the same under high strain-rate loading, with the highest critical energy release rate at 140.1 N/mm for the A1 condition. The lowest energy release rate is 50.2 N/mm for the N2 condition.

Acknowledgments

Thank you to Dr. Tippur, my research advisor, for the constant guidance, mentorship, and encouragement you have provided me. You have taught me many things and poured in many hours of effort to help my academic and research endeavors. Thank you to my committee members, Dr. Suhling and Dr. Shao, for their support of my research and education. Without the help of these three professors this work would not have been possible. Thank you as well to the many Auburn engineering staff members who have helped me along the way, especially Shay Pilcher and Ryan Johnson for their brilliant machining work and for their help in teaching me new skills. Thank you to Indrajit Nandi for your hard work and contribution to this project.

Thank you to my colleagues in the lab, Jackson and Azeez. Your help and support with many different projects have been valuable and your friendship essential to my graduate school life. I would not have gotten through this work without the lunches, trips, and theology discussions we have shared. Thank you to Becky, Patrick, and Greg, and all my friends who have strengthened me throughout this. Your friendship and support have been incredibly rewarding and I am truly grateful for all that you have given me and all the help you have provided. I am thankful to have such great friends to listen to my struggles and celebrate my victories with.

Thank you to my parents, Kennedy and Barbara Edwards, for instilling in me the values of education and hard work, pushing me to be all I can be, and

reminding me to have fun, play hard. Thank you to my sisters, Camryn and Natalie. I am grateful for your constant love and support.

Thank you to God. This work would not be possible without Your many graces. May this thesis bring You greater glory. Let its failures be mine, and its successes be Yours.

Table of Contents

List of Tables

List of Figures

List of Abbreviations

IN-718	Inconel 718
LPBF	Laser Powder Bed Fusion
DIC	Digital Image Correlation
DGS	Digital Gradient Sensing
SIF	Stress Intensity Factor
ERR	Energy Release Rate
LEFM	Linear Elastic Fracture Mechanics
HIP	Hot Isostatic Pressing
AM	Additive Manufacturing
SLM	Selective Laser Melting
SA	Solution and Aging
SZW	Stretch Zone Width
FE	Finite Element
DIC-FE	Digital Image Correlation Finite Element
LPP	Laser Process Parameter
HT	Heat Treatment
SCB	Semi-Circular Beam
PMMA	Poly(methyl methacrylate)
ROI	Region of Interest
CGS	Coherent Gradient Sensing
RMSE	Root Mean Square Error

EDM	Electric Discharge Machining
XCT	X-ray Computerized Tomography
SHPB	Split-Hopkinson Pressure Bar
ASTM	American Society for Testing and Materials
AMS	Aerospace Material Specifications
SR	Stress Relief
SA	Solution Annealing
DA	Double Aging
SEM	Scanning Electron Microscope
EHT	Electron High Tension
KH	Keyhole
LoF	Lack of Fusion

Chapter 1: Introduction

In this introduction, section 1.1 will discuss the motivation of this work and introduce relevant background information. Section 1.2 will review literature on the topics of the digital image correlation (DIC) method, Inconel alloys, and the side groove method. Section 1.3 states the hypothesis, objective, and tasks of this work. Lastly, section 1.4 lays out the organization of the thesis.

1.1 Overview and Motivation

The primary objective of this research is to characterize the mechanical behavior of additively manufactured Inconel-718 alloy with a primary focus on its fracture mechanics. IN-718 is a nickel-based alloy that has many applications in high temperature environments. Inconel alloys are widely used in the aerospace industry; in jet engines, rocket engines, and exhaust systems, to name a few. It has also found many applications in energy generation in heat-critical components such as heat exchangers and pressure vessels for power plants, including pressurized water reactors in nuclear plants. IN-718 is categorized as a superalloy, a category of alloys which can withstand intensely high temperatures without losing material strength significantly. Inconel alloys can withstand temperatures as high as 800° C [1]. Other additively manufactured high temperature superalloys include Hastelloy, GRX, and Mo-Re alloys. With the advent of metallic additive manufacturing, mechanical characterization of additively fabricated IN-718 is of great interest [2]. This work seeks to characterize the fracture properties of additively manufactured IN-718 under quasi-static and dynamic load conditions.

In Laser Powder Bed Fusion (LPBF) additive manufacturing, various conditions in the creation of the parts can have a significant effect on the material properties. This includes introducing defects that can weaken the material strength [3-4]. Prior to printing, the process of atomizing the alloy into a fine powder can affect the powder particle size and cause differences in the finished part. Common atomization methods include water, gas, and plasma atomization [5]. During printing, the environment inside the printer consists of using an inert gas. Argon or nitrogen atmospheres are commonly used, and the inert gas selected can affect the properties of the resulting parts [3]. Furthermore, variation in the laser parameters such as power, scan speed, strip width, and hatch distance can change the mechanical properties of the resulting part or contribute to the presence of pores or defects [3-4]. Finally, after printing, the heat treatment procedure (if any) can also affect grain size in the part, which in turn affects the mechanical properties including fracture toughness [6-9].

To test the effects of these parameters on the fracture properties of IN-718, this work will study specimens quasi-static and high strain-rate conditions. Powder made from plasma atomization and from nitrogen gas atomization is used to manufacture fracture specimens. Plasma atomized specimens are then printed in an argon atmosphere while nitrogen gas atomized specimens are printed in a nitrogen gas atmosphere. During printing, each set of specimens are fused using one of three laser process parameters. After printing is complete, the specimens undergo one of two different heat treatment procedures. By combining these parameters, the

fracture properties of IN-718 produced under 12 manufacturing conditions are investigated in this work.

1.2 Literature Review: Measurement Techniques

Digital Image Correlation (DIC) [10-12] is a common measurement technique used in fracture mechanics studies. DIC allows an experimentalist to measure displacement fields of a specimen without needing additional equipment. Measured displacement fields can then be used to extract fracture parameters such as stress intensity factors (SIFs) and the energy release rate (ERR) or the *J*-integral.

To use DIC for fracture applications, a post-processing step is needed to evaluate the displacement fields from the recorded images. The accuracy of this step depends on the camera resolution, sub-image size and spacing, correlation software used, and quality of the random speckle pattern applied to the specimen [13-15] among others. Because DIC measures two orthogonal displacement component fields simultaneously, both can be used in conjunction with each other when extracting SIFs. Traditionally, only one component of the displacement field has been used to extract SIFs [16-17]. One approach to unite both components of the measured field is to use the radial displacement component u_r instead of the measured Cartesian components u_x or u_y leading to a more accurate mode-I SIF determination under quasi-static conditions [18]. The radial displacement will include a component of both u_x and u_y as dictated by transformation equation.

Another alternative technique for combining both orthogonal components of the displacement field is to develop the combined fields method [19] where they are used in tandem. This technique has been shown to increase the accuracy and

precision of extracted SIFs for mode-I cracks. This ensures that none of the collected data is unused; that is, all measured components of displacement are utilized in conjunction with theoretical descriptions during least-squares error minimization analysis to extract SIFs within the linear elastic fracture mechanics (LEFM) framework. This method is explored in great detail and evaluated for effectiveness in mixed mode experiments during this thesis research.

Another technique used in fracture mechanics for metals is the hybrid DIC-Finite Element technique [20]. This method allows finite element (FE) software to be used to extract the energy release rate as the *J*-integral from displacement fields measured using DIC. The data measured from DIC are used as surface boundary conditions in the finite element model to calculate the *J*-integral and then SIFs using the material properties built into the FE software. In Owens, mixed-mode semi-circular beam specimens made of rubber-toughened epoxy adhesive are tested and the DIC-FE method is compared to least-squares regression approach extraction. The author shows the DIC-FE method to be effective for mode-I and mixed-mode cracks and shows that the method is more robust than regression analysis. The DIC-FE method is also shown to be less sensitive to alterations in the selected crack tip location.

1.3 Literature Review: IN-718

Work studying the material behavior of Inconel alloys has been present in many forms in the literature. Early works prior to the advent of additive manufacturing have studied cast and forged/wrought Inconel specimens made of different alloys for manufacturing parts. In Cook, the effect of temperature and

strain ratio was tested for forged IN-718 specimens under low-cycle fatigue loading [21]. It was found that plastic strain was present throughout the fatigue specimens. Plastic strain was significant enough in some fatigue loading conditions that the mean stress in specimens would tend towards zero even when the initial mean stress was non-zero. The authors concluded that Inconel exhibits elastic-plastic behavior and employed the use of the finite element method to determine the stresses in the material in the region close to the fatigue crack.

In Matthews, three materials showing elastic-plastic behavior, including IN-718, were tested to find the critical energy release rate to estimate fracture toughness [22]. Notched specimens were loaded in three-point bending. The load and crack opening displacement are measured throughout the loading sequence. The energy release rate was then calculated in the elastic-plastic region as $J = \frac{2A}{Bb}$ where A is the area under the load vs loading pin displacement curve up to the point of crack initiation, b is the length of the uncracked ligament, and B is the thickness. The authors then used multiple points post crack initiation to estimate the critical value, J_{IC} at crack initiation. The authors estimate J_{IC} for forged IN-718 to be 12 N/mm.

In Bouse, IN-718 specimens manufactured in a variety of ways, including an experimental Microcast technique, a conventional cast, and wrought parts [23]. The cast parts are then treated with several hot isostatic pressing procedures, and then all specimens are tested under impact loading to determine the dynamic fracture toughness K_{ID}. Due to plastic yielding occurring prior to crack initiation for nearly all manufacturing processes, the extracted value of K_{ID} is not the true

fracture toughness, but a conditional value. The average conditional K_{ID} values extracted for Microcast specimens range from 110 MPa-m$^{1/2}$ to 124 MPa-m$^{1/2}$. Conventional cast and HIP specimens averaged a conditional K_{ID} of 118 MPa-m$^{1/2}$. However, the wrought specimens resulted in the highest conditional dynamic fracture toughness with a value of 133 MPa-m$^{1/2}$.

More recent works that study Inconel alloys focus on additively manufactured specimens. Additive manufacturing can lead to differing material properties in comparison to older cast, forged, and wrought specimens. Additionally, additively manufactured specimens can be made using a variety of techniques and can differ from each other. In Kassner, creep fracture behavior of additively manufactured Inconel alloys are investigated at room temperature and 650°-800° C [1]. Specifically, IN-625 and IN-718 alloys are tested. Additively manufactured (AM) specimens are treated with hot isostatic pressing (HIP) and are compared to wrought specimens of the same alloys. The results show that, while little difference exists in the creep behavior between the wrought and AM specimens at room temperature, the AM specimens show much lower ductility at 650° C. The authors also note that the HIP process given to the AM specimens results in larger grain sizes in the AM microstructure (68 microns) compared to the wrought specimens (11 microns).

In Zhao, the microstructure of LBPF IN-718 specimens is examined [9]. Multiple heat treatments were used and the specimens were tested in tension. It was found that all heat treatments improved the tensile strength compared to the as-built specimens, and that double aging heat treatment increased the hardness. The

researchers also observed embrittlement in the heat-treated specimens tested at room temperature.

In Park, the impact toughness of AM IN-718 is tested [8]. IN-718 specimens were manufactured by Selective Laser Melting (SLM) and subjected to two different heat treatments, namely a solution and aging treatment (SA) and a hot isostatic pressing treatment (HIP). The tensile properties and impact toughness are measured at room temperature and the cryogenic impact toughness is also tested. These data are compared to wrought IN-718 specimens as well. Both AM SA and AM HIP specimens were measured to have lower impact toughness than the wrought specimens at 25 C and -196 C. At room temperature, for AM SA category, the impact toughness is reported as 17.50 J/cm^2 and for the AM HIP specimens impact toughness is reported to be 21.88 J/cm^2, while the wrought impact toughness is 25.00 J/cm^2. At -196 C, the impact toughness is reported as 21.88 J/cm^2 for wrought, 16.88 J/cm^2 for AM HIP, and 14.38 J/cm^2 for AM SA.

In Vielle, the fracture behavior of cast and additively manufactured IN-718 specimens are compared directly [2]. Single edge-notched bending tests were conducted for cast specimens and for two different build orientation of LBPF specimens. It was found that the fracture toughness for both types of AM specimens was greater (666 to 790 kJ/m^2) than that of the cast specimens (400 kJ/m^2). The researchers concluded that the microstructure of the AM specimens could be an advantageous compared to the disoriented microstructure of cast specimens. Additionally, AM specimens experience crack curvature resulting in a mixed-mode

crack, rather than a mode-I crack observed in cast specimens. This also could have contributed to the higher fracture toughness seen in the AM specimens.

In Kawagoishi, IN-718 is tested for fatigue during cyclic bending at room temperature and at elevated temperatures at 300° C, 500° C, and 600° C [24]. The specimens were machined with a notch before testing. In the elevated temperature experiments, the crack began to grow after a greater number of cycles, and higher stress was needed to cause the crack to grow rapidly. At room temperature rapid crack growth occurred at stresses of 550 MPa and greater. At 500° C, rapid crack growth fracture only occurred at stresses of 700 MPa and greater. This shows the brittle properties of IN-718 at room temperature in comparison to a more ductile behavior at elevated temperatures.

In a graduate thesis by Hohnbaum, IN-718 specimens manufactured using LBPF are tested under fatigue loading to determine the threshold value, K_{thr}, the value of stress intensity factor below which the fatigue crack growth rate is zero [25]. Two different heat treatments are explored, and it is found that for conventional heat treatment specimens, K_{thr} is slightly less than 10 MPa-m$^{1/2}$ and for the modified heat treatment specimens it is slightly above 10 MPa-m$^{1/2}$. Additionally, specimens were tested in tension for the purpose of evaluating the fracture toughness. The researchers found significant plasticity in their fracture experiments and this caused their experiments to be invalid for estimating fracture toughness since LEFM was assumed in the method used. Additionally, the authors observed crack front curvature behavior, also called crack tunneling, where the

crack front internal to the specimen was growing ahead of the crack front at the surface.

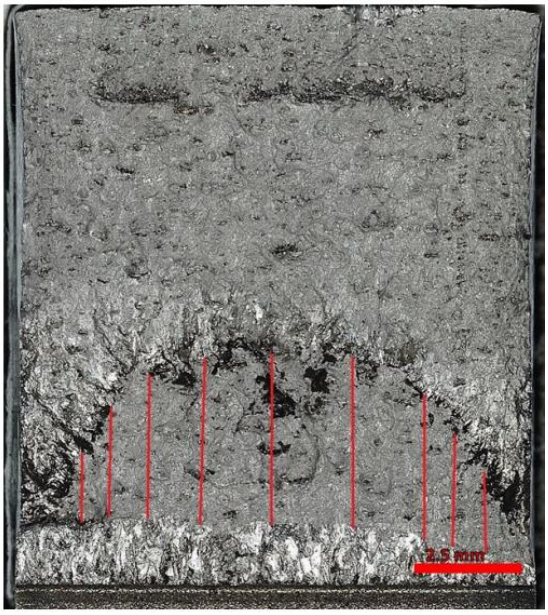

Figure 1.1: Crack front curvature on the fractured surface [25]

This invalidated the fracture toughness measurements. The author concluded based on crack mouth opening displacement measurements that the modified heat treatment may lead to an increase in fracture toughness, but this could not be quantified. The author recommended that future work to adopt a crack groove geometry to mitigate plasticity and allow the fracture properties to be quantified with less ambiguity.

Grooved geometries are discussed in Anderson [26]. He discusses techniques for fracture toughness testing in metals. It is noted that specimens are sometimes manufactured with side grooves (see, Fig. 1.2) to ensure straight crack growth and to prevent crack tunneling similar to the one shown in Fig. 1.1. It is also noted that shear lip formation adjacent to the two surface occurs in specimens

without side grooves. The author recommends that the groove thickness (B_N) should be about 80% of the total thickness (B) to ensure the groove is be effective, and to prevent rapid crack growth on the outer edges of the specimen.

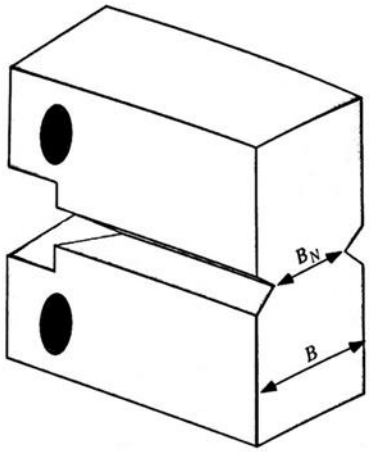

Figure 1.2: Side groove schematic for mitigating shear lips and crack tunneling [26]

In Nalawade, various side groove techniques are evaluated for use in fracture experiments with steel compact tension specimens [27]. It was determined that side grooves with depths up to 0.25B were effective. It was also determined that the root radius of side grooves can affect the performance. Side grooves with root radius less than 100 microns were found to drastically reduce the critical Stretch Zone Width (SZW) and are not recommended.

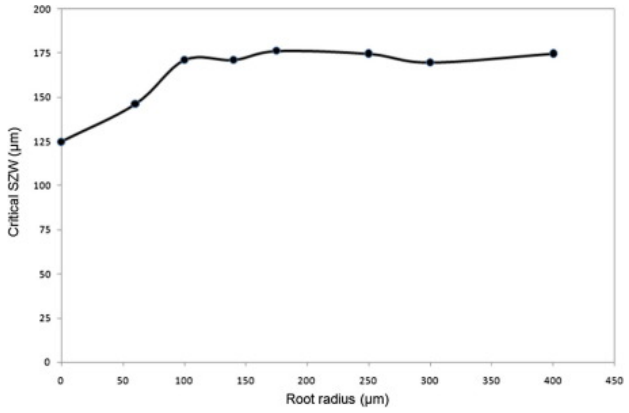

Figure 1.3: The effect of side-groove tip radius on critical stretch zone width. [27]

1.4 Research Objectives

As is clear from the literature review, the study of the fracture behavior additively manufactured Inconel is of great interest. The effect of the additive manufacturing process, such as by the laser powder bed fusion or LPBF approach, and specific manufacturing variables used during manufacture are of interest. Selection of shielding gas and heat treatment procedures affect the grain size in the printed part. Laser Process Parameters (LPP) can introduce defects into the part and become sources of mechanical failure. Therefore, it is hypothesized that shielding gas, heat treatment, and laser process parameter will significantly affect the critical fracture and crack growth resistance behavior of additively manufactured IN-718 specimens in both quasi-static and high strain-rate loading conditions and needs to be examined. Thus, the primary objective of this work is to evaluate the fracture

behavior of IN-718 specimens made under different manufacturing conditions. The specific tasks to complete this are:

- Investigate fracture behavior of IN-718 specimens using full-field optical method of DIC,
- Devise a combined fields least-squares error minimization method for extracting stress intensity factors (SIFs),
- Evaluate the robustness of this method in comparison to the legacy (single-field) extraction method,
- Prepare additively manufactured specimens for different manufacturing conditions
- Insert crack-like defects into the specimens,
- Conduct quasi-static three-point bending fracture experiments using DIC,
- Conduct dynamic high-strain rate fracture experiments in a split-Hopkinson pressure bar apparatus using DIC and ultrahigh-speed photography,
- Extract results using least-squares and DIC-Finite Element (DIC-FE) methods and evaluate the effect of shielding gas, heat treatment, and LPP on critical fracture parameters and crack growth resistance behavior.

1.5 Thesis Organization

This thesis, including this introductory chapter, contains six chapters. Chapter 2 explains the combined field DIC extraction method in detail. Chapter 3 describes the specimen design process for both quasi-static and high strain-rate Inconel-718 specimens to be made with laser powder bed fusion (LPBF) and the various manufacturing conditions to be tested. Chapter 4 describes the experiment

procedures and methods used. Chapter 5 explains the results collected from both the quasi-static and dynamic experiments, the DIC-FE extraction method used to extract results from the collected data and displays the results. Lastly, Chapter 6 discusses the conclusions of this thesis, the objectives accomplished, and potential areas of interest for related future work.

Chapter 2: DIC and Data Extraction Methodology

This chapter contains sections from the publication "Extracting Mixed-Mode Fracture Parameters Using Two Vision-based Methods: Comparison of Combined Fields Method with Legacy Approach" by Edwards, Cho, and Tippur in *Experimental Mechanics* [28]. This chapter will introduce the methodology of digital image correlation (DIC) used throughout this work and will discuss two different data extraction methods. The experiments used in this chapter are described in section 2.2. The extraction methods to be evaluated, called the legacy method and combined fields method, are explained in detail in 2.3. A comparative analysis is conducted, and the results are discussed in 2.4.

2.1 Introduction

Over-deterministic least-squares methods of extracting SIFs from measured full-field quantities in conjunction with asymptotic fields has been the mainstay of experimental fracture mechanics. The vision-based method of Digital Image Correlation (DIC) to determine displacements has played an important role in this regard. In DIC, two or more orthogonal fields are measured simultaneously. Yet, while extracting SIFs, often only one of the components is picked based on intuition/legacy. This could result in erroneous SIF values under mixed-mode conditions. Robustness of SIF extraction by utilizing all components in tandem is demonstrated over a wide range of pure- and mixed-mode conditions. An edge-notched semi-circular specimen geometry is used to create different mode-mixites. The data from DIC are processed using both the combined fields and legacy approaches. The accuracy and robustness of the former relative to the latter is

demonstrated for (a) different number of higher order terms in the asymptotic series, (b) crack tip location uncertainty, and (c) different regions of data extraction. An order of magnitude reduction in standard deviation and root-mean-squared error in mixed and pure mode SIFs are seen for DIC and the combined fields method. Robustness of extracting mixed-mode SIFs accurately by employing all measured fields concurrently in an over-deterministic least-squares approach is superior to using a single component based on intuition/legacy.

2.2 Semi-circular beam (SCB) experiments

Mixed-mode fracture conditions of different mode-mixities ranging from pure mode-I to pure mode-II are difficult to induce in a controlled fashion in a single edge-cracked specimen geometry. In the literature, there are examples of geometries and loading configurations commonly used to accomplish this task. For example, the edge-cracked four-point asymmetric beam geometry, centrally cracked Brazilian disk geometry, and edge or centrally cracked specimens tested using Arcan fixtures are designs where the specimen geometry remains the same, but the loading configuration is altered to achieve the desired mode-mixities. There are other designs where the loading configuration remains the same but the specimen geometry (e.g., crack angle) is altered between tests to achieve the full range of mode-mixites. In the latter category, a simple yet highly versatile edge cracked Semi-Circular Beam (SCB) geometry with a single crack tip has been popular; see, Fig. 2.1. It can be used for both quasi-static and dynamic brittle fracture studies. Chong and Kuruppu (1984) devised this geometry to allow a simple three-point bend loading of specimens obtained from cored geological or

cementitious samples [29]. In the SCB geometry, wide ranging mixed-mode conditions can be achieved using a three-point bending configuration [30-33] and by only varying the angle the crack makes relative to the loading direction. The same geometry can be extended to dynamic conditions either in a one-point or three-point impact loading configuration [30] as well.

In this work, SCB specimens made of PMMA were used for creating the complete range of mixities from pure mode-I to mode-II. Using a laser cutter, specimens with different crack angles β were cut out of a single sheet of commercially purchased material. The nature of these experiments is such that the cracks will not be initiated during the analysis. Any heat effects due to the implementation of the laser cutter will occur close to the inserted notch can be considered negligible due to the Region of Interest (ROI) utilized in this analysis, which is expounded on in later sections. An important consideration when utilizing this geometry was that the loading pin had to be aligned carefully to avoid asymmetric loading from affecting the results. The mixed-mode SIFs for this geometry are expressed as [30],

$$K_I = Y_I \frac{P}{2RB}\sqrt{\pi a} \tag{2.1}$$

$$K_{II} = Y_{II} \frac{P}{2RB}\sqrt{\pi a} \tag{2.2}$$

where Y_I and Y_{II} are geometric factors. The previous investigators have used finite element analysis to evaluate Y_I and Y_{II} for different crack angles [30]. By utilizing their work, five crack angles were selected for experimentation and are listed in

Table 2.1. These provide a theoretical baseline value of K_I and K_{II} to compare the legacy and the combined fields techniques.

Table 2.1: Geometric factors for the selected crack angles

Crack Angle, β	Y_I	Y_{II}	Mode
0°	2.00	0.00	Mode-I
15°	1.75	0.55	Mixed Mode
30°	1.00	0.90	Mixed Mode
40°	0.45	0.85	Mixed Mode
50°	0.00	0.65	Mode-II

a) b)

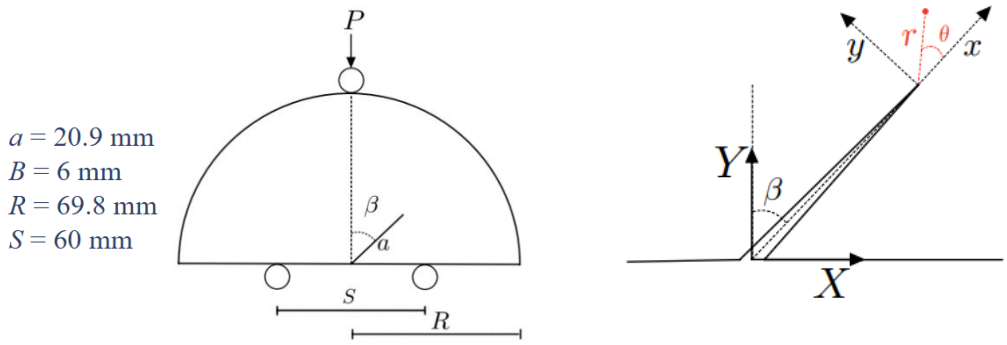

Figure 2.1: a) Semi-Circular Bend (SCB) specimen geometry. b) The local and global coordinate systems adopted.

In this work, a local Cartesian crack tip coordinate system (x, y) is defined such that the crack is oriented in the positive x-direction, see Fig. 2.1b. A global coordinate system is also defined as the X- and Y-directions such that the load is applied in the negative Y-direction. Additionally, since the specimen thickness used is relatively small when compared to the planar dimensions, plane stress assumptions were adopted.

2.3 Digital Image Correlation

2D Digital Image Correlation (DIC) is an optical method that utilizes a random pattern of black and white speckles on a specimen surface in order to evaluate the local displacements during a loading sequence. As the specimen deforms, speckle images are recorded at load-steps of 100 N to be compared with the one at a reference load. The recorded grayscale images are then segmented into sub-images or facets during the post-processing step. The size of the sub-images and the spacing between them is determined by a number of factors including the camera pixel resolution, size of the speckles, and the optical magnification (or the scale factor) used while recording. Upon performing image correlation, the location of the sub-images in the deformed state relative to their positions in the reference state are determined to obtain displacements in two orthogonal directions (say, x- and y-directions). The measured deformations are typically visualized at a load-step as a contour map, a color map or both. Due to the immense popularity of this method in recent years, further details are avoided here for brevity and can be found in many reports [11-12] and monographs [10]. The DIC method is discussed in more detail in section 4.1.

2.4 Data Extraction Approaches

As noted earlier, this work will compare two approaches of extracting SIF values from the same measured data set. These extraction approaches are applicable to both DIC and DGS methods. For DIC, extracting SIFs utilizes Williams' asymptotic expressions for in-plane displacement components [34]:

$$u_x = \sum_{n=1}^{N} \frac{(K_I)_n r^{n/2}}{2\mu\sqrt{2\pi}} \left[\kappa \cos\frac{n\theta}{2} - \frac{n}{2}\cos\left(\frac{n}{2} - 2\right)\theta + \left(\frac{n}{2} + (-1)^n\right)\cos\frac{n\theta}{2} \right] + \sum_{n=1}^{N} \frac{(K_{II})_n r^{n/2}}{2\mu\sqrt{2\pi}} \left[\kappa \sin\frac{n\theta}{2} - \frac{n}{2}\sin\left(\frac{n}{2} - 2\right)\theta + \left(\frac{n}{2} + (-1)^n\right)\sin\frac{n\theta}{2} \right] + P \tag{2.3}$$

$$u_y = \sum_{n=1}^{N} \frac{(K_I)_n r^{n/2}}{2\mu\sqrt{2\pi}} \left[\kappa \sin\frac{n\theta}{2} + \frac{n}{2}\sin\left(\frac{n}{2} - 2\right)\theta - \left(\frac{n}{2} + (-1)^n\right)\sin\frac{n\theta}{2} \right] + \sum_{n=1}^{N} \frac{(K_{II})_n r^{n/2}}{2\mu\sqrt{2\pi}} \left[-\kappa \cos\frac{n\theta}{2} - \frac{n}{2}\cos\left(\frac{n}{2} - 2\right)\theta + \left(\frac{n}{2} + (-1)^n\right)\cos\frac{n\theta}{2} \right] + Q \tag{2.4}$$

In the above, u_x and u_y are displacement components in the x- and y-directions, respectively, $(K_I)_n$ and $(K_{II})_n$ are the nth mode-I and mode-II coefficients of the expansion, r and θ are the crack tip polar coordinates of the data points on the specimen (Fig. 2.1b), μ is the shear modulus, and κ is the Kolosov constant defined as $(3 - \nu)/(1 + \nu)$ for plane stress where ν is the Poisson's ratio. The coefficients associated with the leading term (n = 1) are the mode-I and mode-II SIFs K_I and K_{II}, respectively. The higher order terms (n > 1) and the associated coefficients describe the far-field effects due to the specimen geometry and loading

configuration utilized. Successful extraction of accurate K_I and K_{II} is key to single-parameter LEFM-based analysis and design. It is worth noting that post-processing of speckle images in DIC typically results in a very large data set (of the order of 10^3-10^4) corresponding to different locations near the crack tip. Furthermore, each data point is affected by different amounts of far-field/boundary effects when finite specimen geometries and loading configurations are used. Therefore, to extract accurate values of SIFs using all the data in the ROI, an over-deterministic linear least-squares error minimization is performed. Using the Dugdale plastic zone calculation, for the maximum observed K_I in the experiments, the radius of the plastic zone is $\sim 100\ \mu m$. As the ROI has a minimum diameter of 1.5 mm, these effects can be safely ignored. For simplicity, let the Williams' asymptotic expressions in Eqs. 2.5 and 2.6 can be rewritten as:

$$u_x = \sum_{n=1}^{N} f_{I_n}(r,\theta)(K_I)_n + f_{II_n}(r,\theta)(K_{II})_n + P \tag{2.5}$$

$$u_y = \sum_{n=1}^{N} g_{I_n}(r,\theta)(K_I)_n + g_{II_n}(r,\theta)(K_{II})_n + Q \tag{2.6}$$

Here, the functions $f(r,\theta)$ and $g(r,\theta)$ have subscripts I or II denoting that the function is multiplied by a mode-I or mode-II coefficient, respectively. The subscript *n* denotes the number of the term in the expansion from *n* = 1 to *N* terms. The functions $f(r,\theta)$ and $g(r,\theta)$, depend on polar coordinates r and θ with the origin centered at the crack tip. In both of these methods, the location of the crack

tip is typically identified using the recorded images and/or the contour plots of the correlated data representing the measured field to define the local coordinate system.

2.4.1 Legacy Extraction Approach

The legacy approach of extracting SIFs involves a single component of the measured field even when multiple components are available. This practice is rooted in the fact that the analog methods such as moiré or coherent gradient sensing (CGS) employing traditional setups typically yield only one component of the displacement or stress gradient fields instead of multiple orthogonal components as in the vision-based methods such as DIC and digital gradient sensing (DGS). As a result, a mechanical field judged by the operator as suitable (say, u_y from moiré method for mode-I) is measured and used subsequently in an over-deterministic least-squares analysis for SIF extraction. Although this approach has generally produced satisfactory results for the dominant SIF (for example, K_I in mode-I dominant cases), the accuracy of the less dominant SIF (K_{II}) can be poor and often not addressed or ignored. Given this, the legacy approach becomes questionable in situations involving arbitrary mode-mixity where dominance of one SIF over the other is unclear. Furthermore, for a measured field component, the accuracy of SIF obtained depends also on the region of interest from where the full-field data is extracted, as shown in [35] for mode-I experiments using CGS. Even with the widespread adoption of vision-based methods, the legacy approach of choosing a single field component for SIF extraction has continued despite multiple components being readily available.

Considering u_y as the chosen displacement for analysis in the legacy method, using the functions defined in Eq. 2.7, a set of simultaneous equations can be established [34] as:

$$\{d\} = [g]\{K\}, \tag{2.7}$$

where,

$$\{d\} = \begin{Bmatrix} \Sigma g_{I_1} u_y \\ \Sigma g_{I_2} u_y \\ \vdots \\ \Sigma g_{I_N} u_y \end{Bmatrix}, \quad \{K\} = \begin{Bmatrix} K_{I_1} \\ K_{I_2} \\ \vdots \\ K_{I_N} \\ K_{II_1} \\ K_{II_2} \\ \vdots \\ K_{II_N} \end{Bmatrix}, \text{ and}$$

$$[g] = \begin{bmatrix} \Sigma g_{I_1} g_{I_1} & \Sigma g_{I_2} g_{I_1} & \cdots & \Sigma g_{I_N} g_{I_1} & \Sigma g_{II_1} g_{I_1} & \Sigma g_{II_2} g_{I_1} & \cdots & \Sigma g_{II_N} g_{I_1} \\ \Sigma g_{I_1} g_{I_2} & \Sigma g_{I_2} g_{I_2} & \cdots & \Sigma g_{I_N} g_{I_2} & \Sigma g_{II_1} g_{I_2} & \Sigma g_{II_2} g_{I_2} & \cdots & \Sigma g_{II_N} g_{I_2} \\ \vdots & \vdots & \ddots & \vdots & \vdots & \vdots & \ddots & \vdots \\ \Sigma g_{I_1} g_{I_N} & \Sigma g_{I_2} g_{I_N} & \cdots & \Sigma g_{I_N} g_{I_N} & \Sigma g_{II_1} g_{I_N} & \Sigma g_{II_2} g_{I_N} & \cdots & \Sigma g_{II_N} g_{I_N} \\ \Sigma g_{I_1} g_{II_1} & \Sigma g_{I_2} g_{II_1} & \cdots & \Sigma g_{I_N} g_{II_1} & \Sigma g_{II_1} g_{II_1} & \Sigma g_{II_2} g_{II_1} & \cdots & \Sigma g_{II_N} g_{II_1} \\ \Sigma g_{I_1} g_{II_2} & \Sigma g_{I_2} g_{II_2} & \cdots & \Sigma g_{I_N} g_{II_2} & \Sigma g_{II_1} g_{II_2} & \Sigma g_{II_2} g_{II_2} & \cdots & \Sigma g_{II_N} g_{II_2} \\ \vdots & \vdots & \ddots & \vdots & \vdots & \vdots & \ddots & \vdots \\ \Sigma g_{I_1} g_{II_N} & \Sigma g_{I_2} g_{II_N} & \cdots & \Sigma g_{I_N} g_{II_N} & \Sigma g_{II_1} g_{II_N} & \Sigma g_{II_2} g_{II_N} & \cdots & \Sigma g_{II_N} g_{II_N} \end{bmatrix}.$$

Here, N is the number of terms in the expansion, $\{d\}$ contains the measured displacement data, $[g]$ is a matrix of size 2N × 2N and contains the functions from Williams' asymptotic expressions, and $\{K\}$ contains the two SIFs and other higher order coefficients that must be solved for using the over-deterministic analysis. To isolate $\{K\}$, the inverse of $[g]$ is to be evaluated:

$$\{K\} = [g]^{-1}\{d\} \tag{2.8}$$

In the legacy approach, the size of the matrices is determined by the number of terms used in the expansion. Using a different number of higher order terms can affect the SIF values in the legacy approach. Additionally, the summation of the $g(r,\theta)$ functions in the $[g]$ and matrices represent the summation of the functions across the number of data points in the region of interest. Altering the region of data points included in the analysis affects the extracted SIF values as well. Finally, as stated previously, these functions depend on r and θ centered at the crack tip. Therefore, identifying a precise location for the crack tip is crucial for extracting correct SIF values.

2.4.2 Combined Fields Approach

The combined fields approach for extracting SIFs utilizes all available components of the measured field concurrently. For 2D DIC, this involves using both components of measured displacement in conjunction with the Williams' asymptotic expressions. It leads to a matrix relationship [19]:

$$\{u\} = [g']\{K'\} \tag{2.9}$$

where,

$$\{u\} = \begin{Bmatrix} u_{x_1} \\ u_{x_2} \\ \vdots \\ u_{x_m} \\ u_{y_1} \\ u_{y_2} \\ \vdots \\ u_{y_m} \end{Bmatrix}, \{K'\} = \begin{Bmatrix} K_{I_1} \\ K_{I_2} \\ \vdots \\ K_{I_N} \\ K_{II_1} \\ K_{II_2} \\ \vdots \\ K_{II_N} \\ P \\ Q \end{Bmatrix}, \text{ and}$$

$$[g'] = \begin{bmatrix} f_{I_1}^{1} & f_{I_2}^{1} & \cdots & f_{I_N}^{1} & f_{II_1}^{1} & f_{II_2}^{1} & \cdots & f_{II_N}^{1} & 1 & 0 \\ f_{I_1}^{2} & f_{I_2}^{2} & \cdots & f_{I_N}^{2} & f_{II_1}^{2} & f_{II_2}^{2} & \cdots & f_{II_N}^{2} & 1 & 0 \\ \vdots & \vdots & \ddots & \vdots & \vdots & \vdots & \ddots & \vdots & \vdots & \vdots \\ f_{I_1}^{m} & f_{I_2}^{m} & \cdots & f_{I_N}^{m} & f_{II_1}^{m} & f_{II_2}^{m} & \cdots & f_{II_N}^{m} & 1 & 0 \\ g_{I_1}^{1} & g_{I_2}^{1} & \cdots & g_{I_N}^{1} & g_{II_1}^{1} & g_{II_2}^{1} & \cdots & g_{II_N}^{1} & 0 & 1 \\ g_{I_1}^{2} & g_{I_2}^{2} & \cdots & g_{I_N}^{2} & g_{II_1}^{2} & g_{II_2}^{2} & \cdots & g_{II_N}^{2} & 0 & 1 \\ \vdots & \vdots & \ddots & \vdots & \vdots & \vdots & \ddots & \vdots & \vdots & \vdots \\ g_{I_1}^{m} & g_{I_2}^{m} & \cdots & g_{I_N}^{m} & g_{II_1}^{m} & g_{II_2}^{m} & \cdots & g_{II_N}^{m} & 0 & 1 \end{bmatrix}.$$

Here, *N* is the number of terms in the expansion and *m* is the number of data points in the region of interest. The matrix $\{u\}$ contains both the *x*- and *y*-field components of the measured displacement data and rigid body terms P and Q, and the matrix $\{K'\}$ contains the SIFs and the higher order coefficients that are solved for by performing the over-deterministic linear least-squares error minimization. The matrix $[g']$ contains functions $f(r,\theta)$ and $g(r,\theta)$, and a series of 1 and 0 coefficients for the P and Q rigid body terms. Again, the subscripts *I* and *II* denote mode-I or mode-II functions, respectively, and the subscript *N* denotes the higher order term the function relates to. In the legacy method, the functions in the matrix are summed across all terms in the region of interest. In the combined fields method, this summation occurs as a result of evaluating Eq. 2.10 rather than occurring in the matrix directly. Because of this, an additional superscript is added to denote the data point that each function is related to for all points in the region of interest. The superscripts numbered 1 through *m* in the $[g']$ matrix correspond to the subscripts in the $\{u\}$ matrix. The coefficients in $\{K'\}$ can be solved as,

$$([g']^T[g'])^{-1}[g']^T\{u'\} = \{K'\} \tag{2.10}$$

Note that because $[g']$ generally has a different number of rows ($2m$) than columns ($2N+2$), a standard matrix inversion is not possible. By multiplying $[g']$ and its transpose $[g']^T$ a new matrix that can be inverted is made for solving $\{K'\}$ and extract values of all the coefficients.

The size of the matrices is determined by both the number of terms N and the number of data points m in the region of interest. This is unlike the legacy method where the matrix sizes are determined only by the number of terms N. Therefore, the value of N chosen in the analysis and the number of data points m included in the region of interest will both influence the extracted SIFs. Additionally, the functions $f(r,\theta)$ and $g(r,\theta)$, depend on the polar coordinates r and θ, which are in the coordinate system with the origin centered at the crack tip. Therefore, imprecise location of the crack tip can affect the values of SIFs.

2.5 Experimental Setup

For performing experiments using DIC, a random speckle pattern was applied to one of the two faces of the SCB specimen by spraying black and white paints successively. The specimen was subsequently subjected to three-point bending. Two white light sources were used for illuminating the specimen uniformly and the recording was done using a Point-Grey 4 Mpx camera. The schematic of the experimental setup is shown in Fig. 2.2.

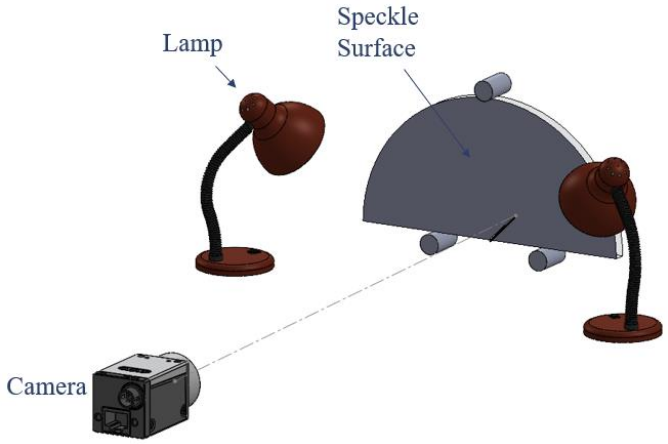

Figure 2.2: Schematic of the experimental setup for DIC

An Instron-4455 mechanical testing machine was used to load the specimen from 0 - 1500 N in the displacement control mode with a crosshead speed of 0.5 mm/s. During ramp loading, both the load and loading-pin displacement data were recorded. Simultaneously, the speckle images from the specimen surface were captured at specific load steps at a rate of 2 fps. Images were then selected that correspond to load steps of 100 N. The images were then post-processed using ARAMIS image analysis software with the no-load image as the reference image. Examples of the resulting displacement contours are shown in Fig 2.3 for two different crack angles at the maximum load level of 1500 N. The camera parameters and image analysis software specifics are listed in Table 2.2.

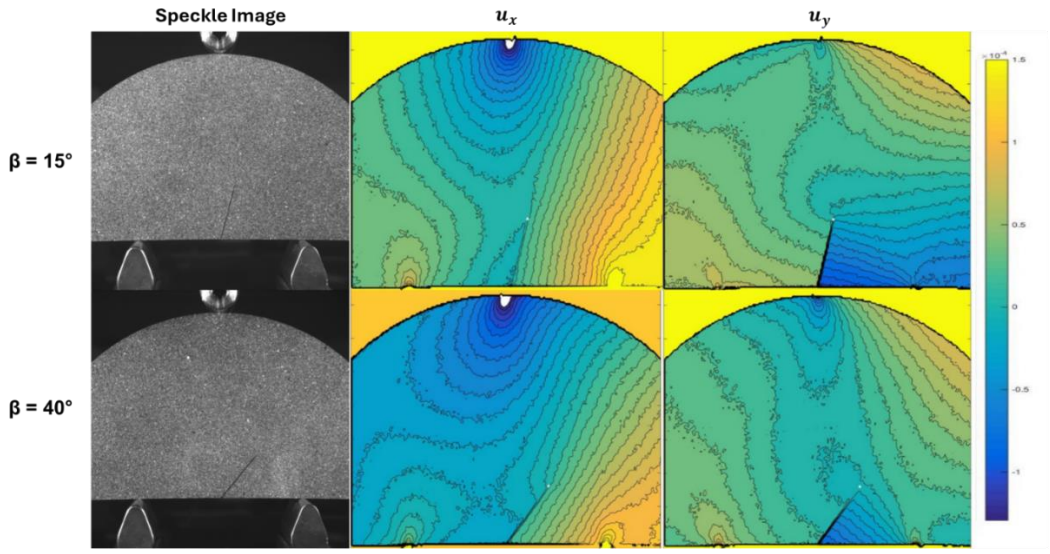

Figure 2.3: The recorded speckle images (column 1), displacement components u_x and u_y Contours (in local coordinates) from DIC (columns 2 and 3) (contour increments: 10 μm/contour)

The contour plots in Fig. 2.3 show the measured displacement fields in the *local* crack tip coordinates. All four plots have a contour spacing of 10 μm/contour. Both sets show mixed-mode crack tip deformations and the influence of the loading pin and the two supports. For β = 15° geometry, the u_y contours show a larger crack opening displacement relative to β = 40° case as it is relatively mode-I dominant. In β = 40° case, on the other hand, the contours show a larger crack sliding displacement u_x as mode-II conditions are more pronounced.

Table 1.2: Camera Specifications and Image Analysis Features

Hardware Parameters		**Analysis Parameters**	
Camera Manufacturer	Point Grey	Software Package	ARAMIS v6.3.1

Camera Model	Grasshopper3 GS3-U3-41C6M	Software Manufacturer	GOM
Image Resolution	2048 x 2048 px	Image Filtering	None
Lens Manufacturer	Computar Lens	Sub-image Size	20 px
Focal Length	18 - 108 mm	Step Size	10 px
Field of View	98 x 98 mm	Subset Shape Function	Affine
Image Scale	0.048 mm/px		
Stand-off Distance	1 m		
Image Acquisition Rate	2 fps		
Patterning Technique	Spray Painted		
Approx. Feature Size	5 px		

2.6 Results and Discussion

The values of SIFs K_I and K_{II} extracted from the DIC experiments using both the legacy and the combined fields approaches are compared with each other in Fig. 2.4, with each row for a different crack angle and the second and third columns showing the two SIF extraction approaches. As noted earlier, the five crack angles chosen cover the entire range of mode-mixities, from pure mode-I to mode-II.

In Fig. 2.4, the solid and open symbols (rectangles and circles) correspond to mode-I and mode-II SIF values, respectively. The predicted results are shown as solid and dotted lines. Each plot covers the SIF values over the loading range of 0-1500 N. The measured data in the range $0.5 < r/B < 1.5$ (B = thickness) and $-135° < \theta < 135°$ was used for both the legacy and the combined fields approaches. This was to exclude any crack tip triaxial deformation and free surface effects in the region too close to the crack flanks, as well as for excluding the effects of the loading and support pins. In addition, both the legacy and the combined fields methods used $N = 4$ terms. The improvements seen by utilizing both orthogonal displacement field components in tandem is evident in all of the plots, with an overall increase in accuracy and precision relative to the theoretical solution. For the legacy approach, there is noticeable scatter in the K_I values and substantial scatter for K_{II} values across all crack angles. That said, the legacy K_I values are close to the expected theoretical ones. On the other hand, when using the combined fields approach, both SIF values show a consistent, more precise and linear progression. More importantly, the values of both SIFs closely match the respective predictions with greater accuracy and precision. The deviations that exist in the data are due to inherent noise in the measured data, likely error in selecting a crack tip location, selected region of interest, or a combination of these factors. For all angles, the effect from these sources of error is visibly more significant when using the legacy approach than the combined fields approach.

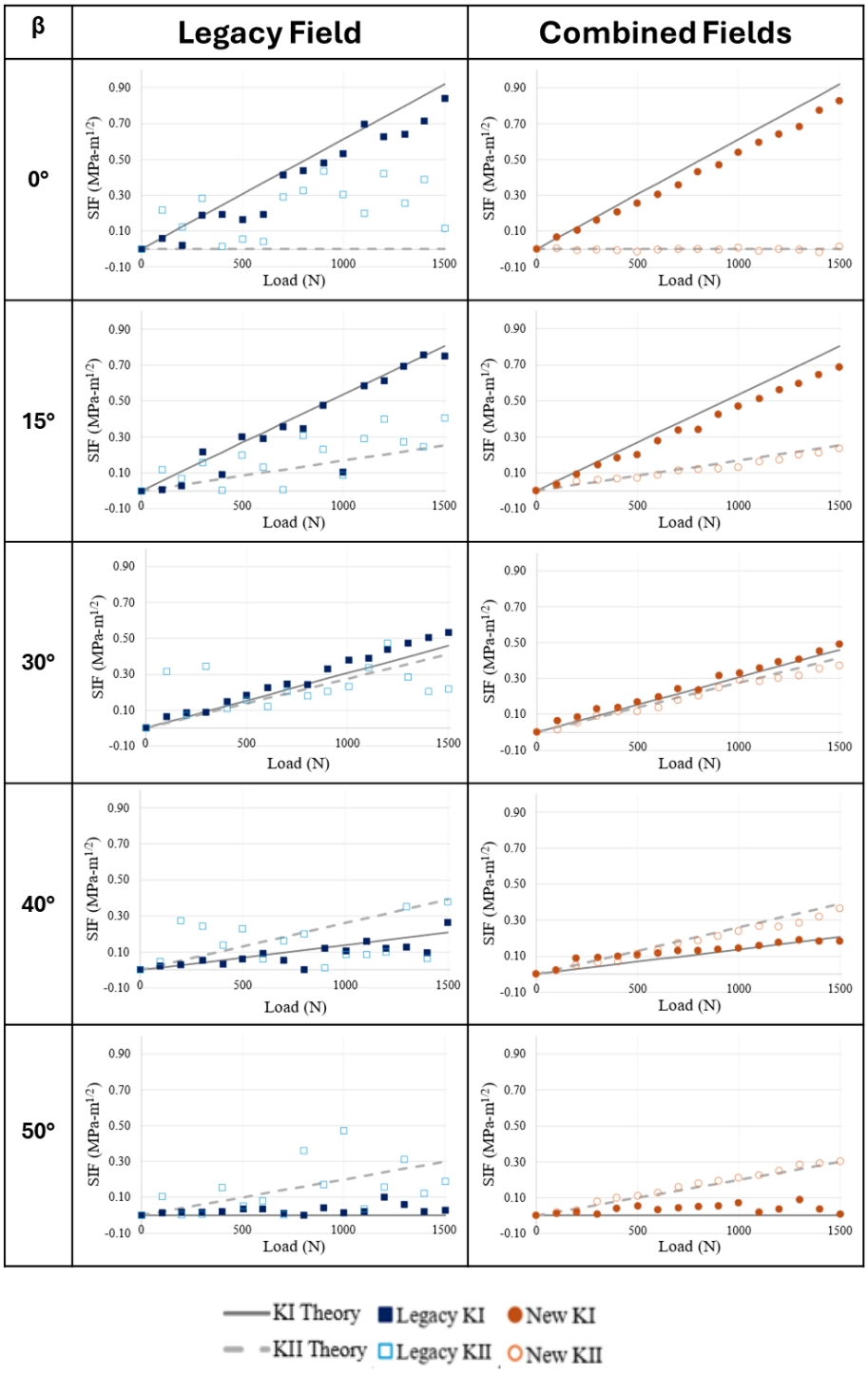

Figure 2.4: SIFs at different loads for different crack angles and different extraction approaches using measured displacements from DIC. (Legacy method uses u_y field in the analysis.)

In order to further characterize the improvement of the combined fields method, additional analysis parameters were varied to demonstrate its robustness relative to the legacy approach. For brevity, the results corresponding to only the maximum load (1500 N) are shown here. The selected parameters during analysis were the number of higher order terms used, the location of the crack tip that was selected, as shown in Fig. 2.5a and the region of interest utilized in the analysis (Fig. 2.5b). When an extraction method is robust, the effects of altering these parameters will be minimum. The variation in the extracted SIF values from these parametric variations were compared qualitatively and quantitatively to determine the better of the two approaches.

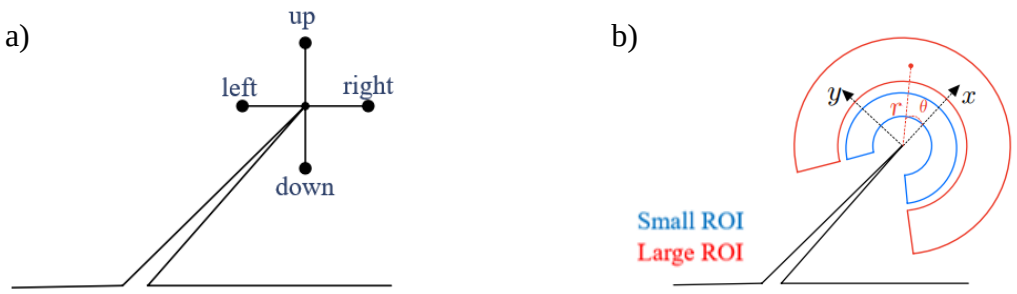

Figure 2.5: Schematic representation of varying a) crack tip position (left), b) region of interest during analysis (right)

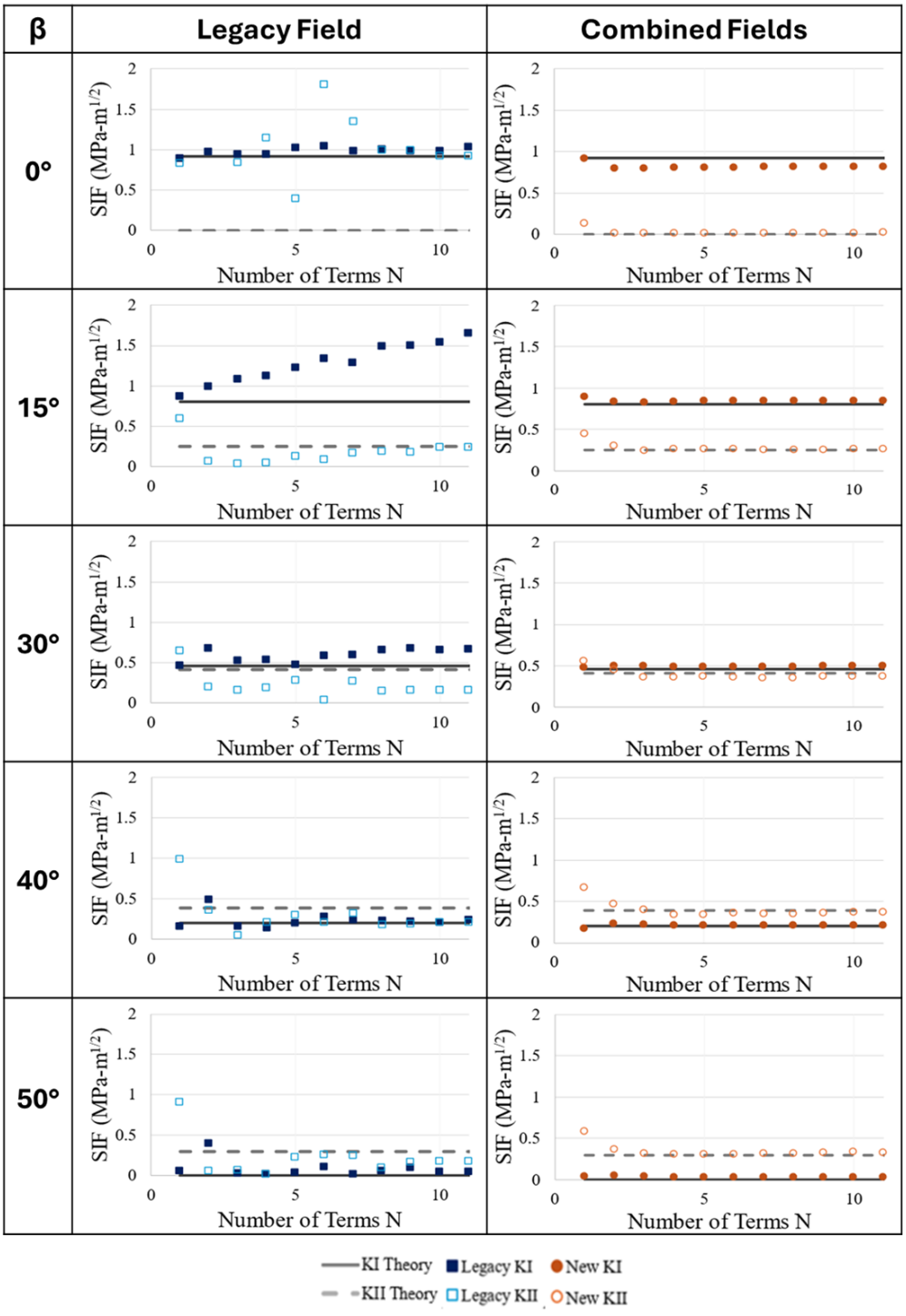

Figure 2.6: Variation of SIFs for different higher order terms in the asymptotic expansion for the legacy and combined fields approaches using DIC. (Legacy method used u_y field in the analysis.)

For a method to be considered robust, it should be capable of extracting consistent and accurate values of SIFs across multiple different parameterized iterations, indicating that the results that are produced are not merely due to an operator input but are displaying the experimental outcome accurately. To assess this, the highest load-step is iterated across different numbers of higher order terms N in the asymptotic series. By truncating the series after a different number of terms, we can also identify if there is an ideal number of higher order terms to use in the analysis for the geometry, or if the method is robust enough to successfully extract SIFs for a range of N values. These results are shown in Fig. 2.6.

By comparing the plots in Fig. 2.6, the two extraction techniques can be contrasted for the same specimen geometry at a fixed load. Note that for each row of plots, the second and third columns describe the results from the same experimental data but a different extraction approach. The gray solid and dashed lines represent the predicted values. The solid symbols (squares and circles) represent the extracted values for K_I and the open symbols represent K_{II}. It is noteworthy that the experiments may not have perfectly replicated the predictions due to experimental and post-processing errors, and therefore deviations of less than 5% from the predictions are considered acceptable. By comparing the combined fields method to the legacy approach, the improvements become rather clear. Although both methods produce similar data trends, the combined fields approach does a significantly better job of extracting the trend consistently across any number of terms N of the experiment with deviations of less than 2%. While K_I for the legacy approach is acceptable, the K_{II} values vary significantly with load

(standard deviation $\approx$ 1 MPa$\sqrt{\text{m}}$) and seem to not adhere to an explainable trend. In contrast, the tight grouping of values of both K_I and K_{II} in the combined fields method shows the robustness and gains in both accuracy and precision. As can be seen, the legacy method performs poorly while extracting consistent values of SIFs in comparison to the combined fields method. For $\beta = 0^o$ case, even though the K_I values are close to the predicted value, K_{II} values are far from the prediction. For every subsequent geometry, the deviation between the extracted values of the same experiment as N is increased indicates scenarios where two operators working with the same data set could extract values as much as 50% different from the legacy method. In contrast, with the values being very similar for $N \geq 3$ as well as K_I and K_{II} are both accurate, once again the precision of the combined fields method is clear. This difference indicates once again that using all orthogonal fields simultaneously is more robust to changes in the number of higher order terms than the legacy method, resulting in SIFs having greater consistency.

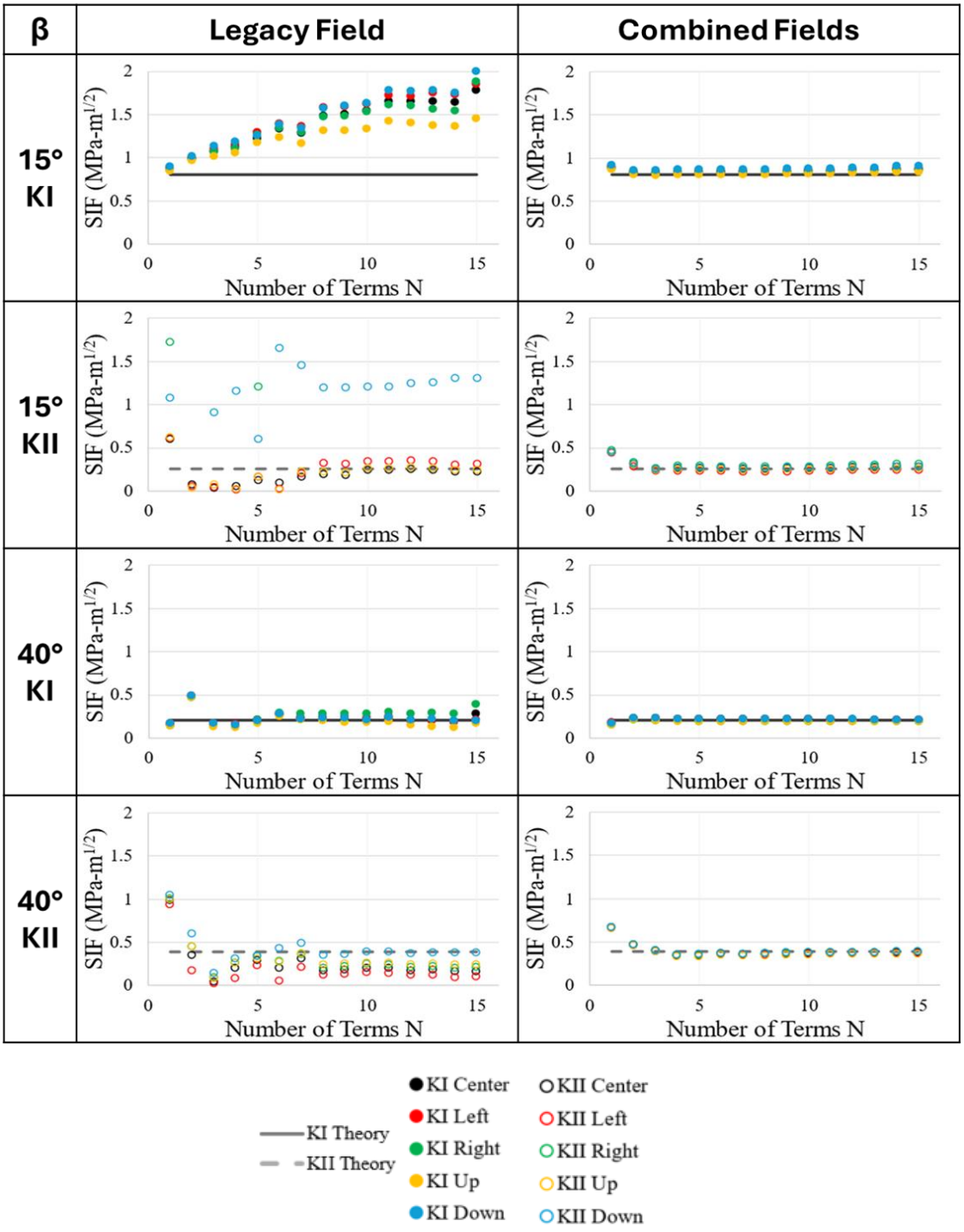

Figure 2.7: Variation of SIFs due to different crack tip position selection in the legacy and combined fields approaches using DIC. (Legacy method uses u_y field in the analysis.)

Next, the robustness of the method to crack tip selection errors was assessed at a fixed load of 1500 N. In Fig. 2.7, five sets of SIF results are shown on each plot. These five sets were acquired by altering the position of the crack tip as shown in Fig. 2.5b. This variation in crack tip selection is meant to simulate an experimental error that could occur due to operator error during analysis. The crack tip location was intentionally altered by a distance of 10 pixels in each of the four directions: up, down, left, and right, as shown, relative to the initial pick. Including the original crack tip selection, the outcomes consist of five distinct SIF data series. Each of these are displayed in Fig. 2.7 for the number of terms N up to 15. Closed symbols are used to denote K_I and open ones denote K_{II}. Again, the solid and dashed lines represent the predicted values. The columns two and three show results for the legacy and the combined fields approach. Since the same observation occurs in all geometries, only β = 15° and β = 40° are shown here as representative examples. For the β = 15° geometry, the legacy approach of extracting K_I drifts away from the prediction for a higher number of terms N and has a significant amount of variation (standard deviation $= 0.258$ MPa$\sqrt{\text{m}}$). In addition, the legacy method has a large spread when extracting K_{II} (standard deviation $= 1.099$ MPa$\sqrt{\text{m}}$). On the other hand, the combined fields approach extracts a consistent value for K_I and K_{II} for all five crack tip selections. The variation for the new approach (standard deviation < 0.025 MPa$\sqrt{\text{m}}$) is an order of magnitude lower than the legacy approach. For the β = 40° the new method again extracts much more consistent values for SIFs. The standard deviation in the data extracted using the new approach is more than 50% lower than the legacy counterpart. Additionally, the extracted

values of SIFs using the new method match the predicted values more closely. This overall results in a significantly lower cumulative crack tip error for the combined fields method in comparison to the legacy method.

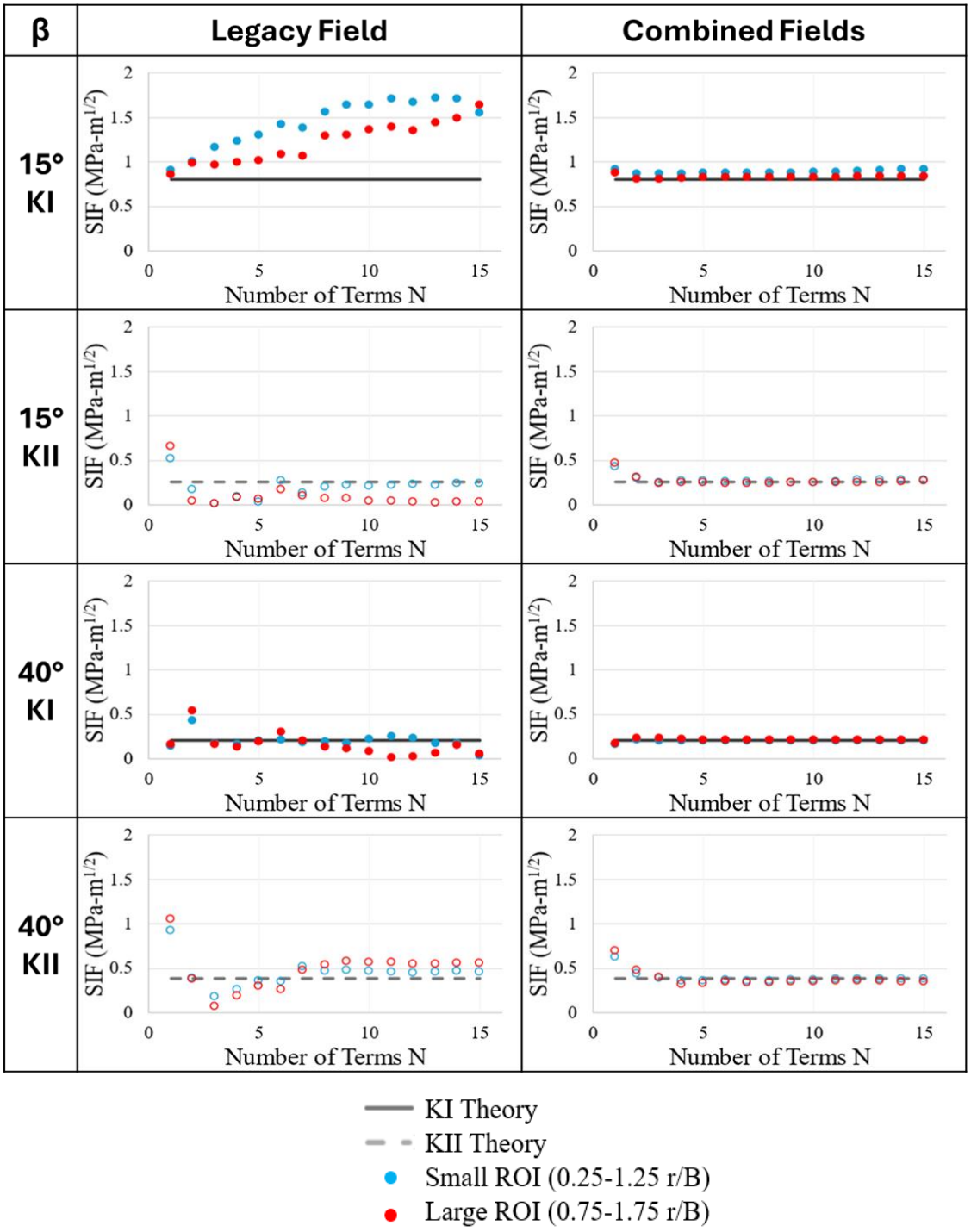

Figure 2.8: Variation of SIFs for two different regions of interest for the legacy and combined fields approaches using DIC. (Legacy method uses u_y field in the analysis.)

In Fig. 2.8 two sets of results are shown on each plot representing data extraction in the large and small regions of interest (Fig. 2.5a). The original region of interest was $0.5 < r/B < 1.5$ and $-135° < \theta < 135°$. Additional regions of interest were created with the limits on θ unchanged, but the r/B range was decreased and increased relative to the original. For the smaller region of interest, the range was $0.25 < r/B < 1.25$ and for the larger region of interest, the range was $0.75 < r/B < 1.75$. The results extracted using both regions of interest are displayed in Fig. 2.8 at 1500 N and for a number of terms up to $N = 15$. Note that the results for the original region of interest are not repeated here for brevity and clarity of plots.

As before, the closed symbols are used when plotting K_I and open symbols for K_{II}. The solid and dashed lines represent the predicted values. The same trend is seen in all five geometries but for brevity the ones for $\beta = 15°$ and $\beta = 40°$ are shown as representative examples. In the $\beta = 15°$ case, the legacy approach extracts K_I with a standard deviation of $0.250\ \text{MPa}\sqrt{\text{m}}$ and K_{II} with standard deviation of $0.087\ \text{MPa}\sqrt{\text{m}}$. This is significantly improved in the combined field approach which extracts K_I with standard deviation of $0.058\ \text{MPa}\sqrt{\text{m}}$ and K_{II} with a standard deviation of $0.017\ \text{MPa}\sqrt{\text{m}}$. For the $\beta = 40°$ geometry, similar improvements are seen as well.

To summarize the improvements in robustness seen by using the combined field method, Tables 2.3 and 2.4 include the standard deviation and root mean square error (RMSE) for the SIF results shown in Fig. 2.7 and 2.8, respectively. The standard deviation represents the average deviation in the extracted SIF without

regard to the predicted value, while the RMSE represents the average error SIFs have from the predicted value. In a perfectly robust technique, the standard deviation and RMSE would both be zero, as there would be no deviation regardless of the changes to the parameters. For both of these quantities, the new approach consistently has lower deviation and lower error for all crack angle geometries and mode-mixities.

Table 2.3: SIF Variation Due to Crack Tip Selection in DIC

Geometry	Approach	Standard Deviation ($MPa\sqrt{m}$)	RMSE ($MPa\sqrt{m}$)
$\beta = 15^{\circ}$	Legacy K_I	0.2579	0.8499
	Legacy K_{II}	1.0992	1.2777
	Combined K_I	0.0235	0.0475
	Combined K_{II}	0.0240	0.0251
$\beta = 40^{\circ}$	Legacy K_I	0.0847	0.1238
	Legacy K_{II}	0.1147	0.1828
	Combined K_I	0.0117	0.0119
	Combined K_{II}	0.0303	0.0393

Table 2.4: SIF Variation Due to Region of Interest Selection in DIC

Geometry	Approach	Standard Deviation ($MPa\sqrt{m}$)	RMSE ($MPa\sqrt{m}$)
$\beta = 15^{\circ}$	Legacy K_I	0.2500	0.6243
	Legacy K_{II}	0.0866	0.1490
	Combined K_I	0.0279	0.0525
	Combined K_{II}	0.0172	0.0182
$\beta = 40^{\circ}$	Legacy K_I	0.1055	0.1054
	Legacy K_{II}	0.1570	0.1602
	Combined K_I	0.0083	0.0085
	Combined K_{II}	0.0315	0.0394

In this chapter, extraction of SIFs from multiple orthogonal mechanical fields used in tandem is assessed relative to the legacy approach of selectively employing one of the measured fields. The over-deterministic least-squares error minimization of measured fields to extract SIFs are examined over a wide range of mixed-mode conditions from pure mode-I to mode-II. The fields assessed are crack tip displacements n two orthogonal planar directions in semi-circular beam (SCB) geometries with five different crack angles. In all, the combined fields method results in a clear and consistent improvement over the legacy approach. Furthermore, as the over-deterministic linear least-squares analysis is a post-processing step, the combined fields approach can be implemented for any prior data as long as data for both the fields has been preserved.

For DIC experiments, the improvement in the accuracy and robustness of the method, and its ability to withstand potential operator errors in all mixed-mode cases is strongly evident. The number of higher order terms of the asymptotic crack tip field used in the analysis, the positional error of the crack tip by the operator, and the region of interest where the data are selected from, all have minor effect on the extracted value of SIF when using the combined fields approach. These improvements are especially clear for the mode-II SIF. Additionally, an order of magnitude reduction in the standard deviation and root mean squared error in the SIF values are quantified in the mixed-mode examples considered.

Chapter 3: Specimen Design

This chapter will discuss the geometry and design of specimens used in the experiments. The design of specimens for quasi-static tests and the process by which they were manufactured are described in section 3.1. The high-strain rate specimen geometry and its design is discussed in section 3.2. Lastly, section 3.3 will discuss the material conditions used during the LPBF additive manufacturing process and the different variables which are being tested for their effect on the fracture behavior of IN-718 alloy.

3.1 Quasi-Static Specimens

The geometry for the quasi-static specimens is a rectangle with a span of 80mm and width of 22mm. The thickness is 3mm. At the midspan, a 5mm crack-like notch is introduced into the specimen, as shown in Fig. 3.1. This notch is machined to be as thin as possible to simulate a crack-like behavior. Ideally, the notch tip would have an infinitesimally small root radius. Using wire electric discharge machining (EDM), very thin notches can be machined. Wire EDM also allows for very precise cuts to be made. EDM wires are available in a variety of sizes less than 500 microns in diameter. In this work, notches were inserted using a Mitsubishi MV1200S wire EDM with a wire rated as 0.004 inches (~100 microns) was used. The resulting notch was measured using an optical microscope and was found to be approximately 90-110 microns wide. It should be noted that the notch has a rounded crack tip using this method, rather than a square tip as seen in alternative methods such as abrasive-impregnated diamond saw cutting. Another

advantage of using wire EDM is the high replicability of the notch produced due to the cut being made automatically with a machine rather than by hand.

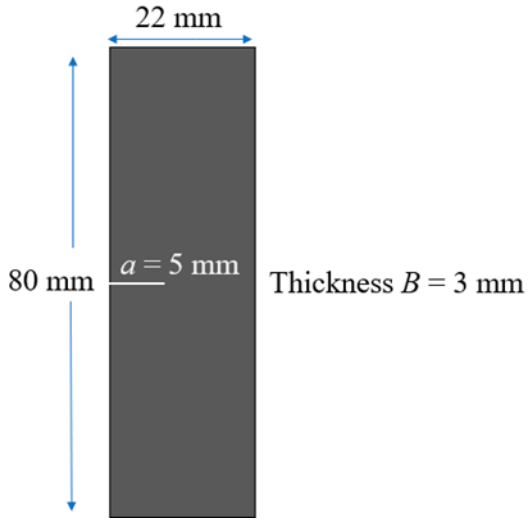

Figure 3.1: Schematic diagram of quasi-static fracture specimen geometry

When using EDM, considerations for specimen alignment are needed so that all the notches inserted are identical to each other. A custom steel fixture was made to assist in aligning the specimens in the EDM. This fixture allowed for a stack of four specimens to be cut at the same time. This also allowed the specimens to be positioned farther from the edge of the base than simply mounting them to the base directly, which aided wire alignment and ensured that the cut could be made without the wire reaching the limit too close to the base.

The size of the specimen was chosen carefully with due consideration for the 3-point bend loading configuration. That is, the dimensions were such that stress concentrations from the loading pin and the supports would not be too close to overlap with that due to the crack tip when loaded. This is for the purpose that the measurements are to be affected primarily from the crack-tip without undue interference from loading pin stress concentrations. However, widening the

specimen requires more energy to cause crack-initiation, thus making a smaller specimen more desirable for ease of experimentation. Also, smaller specimens are prone to out-of-plane bending or buckling effects. After trials with 15mm, 20mm, 22mm, and 25mm wide specimens, it was found that 22mm was the a good width to minimize loading pin effects on the crack tip.

The original design for the specimen geometry had a flat face on the front and back of the specimen. However, early experiments resulted in a non-planar crack front referred to as the 'crack tunneling' behavior. This causes the true crack front tip inside the specimen to tunnel ahead of the visible crack tip on the surface. This behavior is further discussed in detail in section 3.1.1. The crack tunneling behavior was resolved by incorporating a side-groove to the front and back faces of the specimen at the midspan tracing from the EDM notch tip to the point of contact with the loading pin, as shown in Fig. 3.2. The groove depth was 0.5mm on either side such that the minimum specimen thickness is 2mm at the deepest part of the groove. The rest of the specimen's thickness was left unchanged as 3mm.

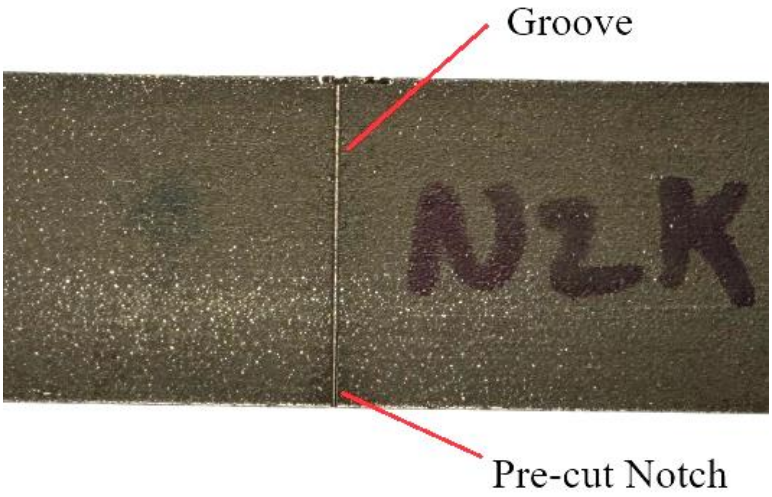

Figure 3.2: Photograph of the crack groove on the front face of the quasi-static specimen

The groove along the front and back surface of the specimen is also added using wire EDM. Due to the need for greater precision in aligning the groove with the notch, a wider wire 0.010 inches (~250 micron) in diameter was used. This increased accuracy in the alignment of the groove and ensured that the cut was inserted consistently in all specimens. Before cutting the groove, the surface of the specimen was polished with 80 grit sandpaper to allow the wire to make a uniform contact with the face of the specimen. Great care was exercised to remove very little material so that the polishing process did not change the thickness of the specimen. The polishing was done only to smooth out the surface texture of the specimen. After polishing, the specimens were rinsed in water and then were ready to be cut in the EDM machine.

3.1.1 Crack Tunneling Behavior

After early experiments using ungrooved specimens examining the Load vs. Load-Point Deflection behavior of the 3-point bend specimen (see Fig. 3.3) revealed an expected monotonic increase with a distinct decrease/drop in the load prior to the crack growth visibly seen initiating on the surface. This suggested the possibility of crack tunneling, a behavior often seen in ductile materials where the crack at the midplane/mid-thickness of the specimen will grow internally ahead of the crack on the surface, resulting in a non-planar crack front with a significantly advanced crack tip on the mid-plane while not being visible on the surface. Adding side grooves removed this sudden drop indicating crack tunneling had been mitigated by the grooved geometry, as seen in Fig. 3.3b.

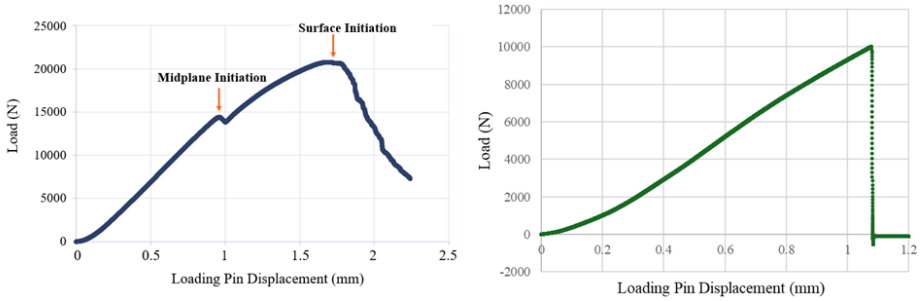

Figure 3.3: Load and deflection plots a) with flat faced specimen showing an unexpected dip, b) with grooved specimen showing monotonic loading

Further evidence of this behavior was seen when examining the fracture surface, which contained significant inclined shear lips adjacent to the front/back specimen faces and a triangular region in the interior showing possible crack tunneling behavior. These shear lips also cause the crack to kink to one side rather than growing in a self-similar fashion. In order to use the DIC method to assess fracture parameters associated with crack initiation and growth behaviors, locating the crack tip precisely at various stages of crack growth is essential. Therefore,

crack tunneling introduces a significant amount of error in the extraction of fracture parameters and limits the ability of existing closed form 2D solutions to be useful in that task.

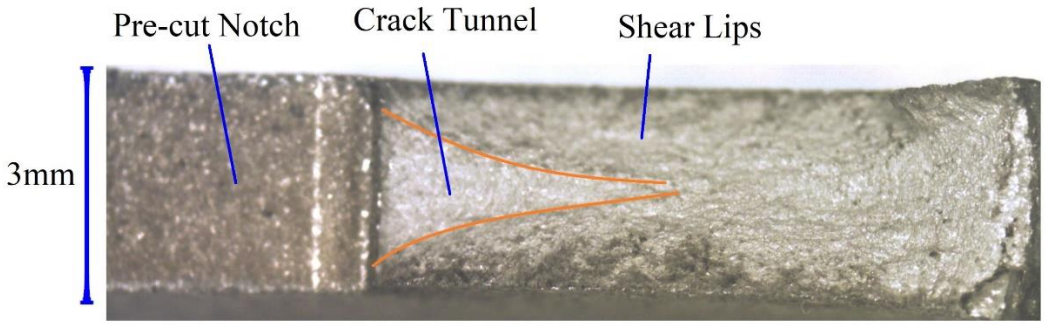

Figure 3.4: Fractured surface of specimen revealing crack tunneling behavior

The crack tip location is best identified by examining the speckle images of the specimen photographed by a camera during the experiment in conjunction with deformation contour plots from DIC data after the recorded images are correlated relative to the reference image. Looking at the crack tip in the speckle images as the load increases allows an experimentalist to identify the load and time-step when the crack begins to initiate. This estimate can then be confirmed using the contour plots generated from the correlated displacement field data. The crack tip location on the contour plot can be typically identified by observing the convergence of the deformation contours. Additionally, by recording the location of the observed crack tip in the contour plots for increasing load levels, a clear identification of crack initiation instant can be determined when the crack tip location begins to change visually. By this supervised method, the crack tip can be located to an error of approximately half a sub-image/facet. Increasing the size of the sub-images decreases the precision with which the crack tip can be located because the crack

tip location is captured by a greater number of sub-images, but measurement noise in contours decreases with larger sub-image size. The effect of sub-image size and other DIC parameters is detailed in section 4.1.

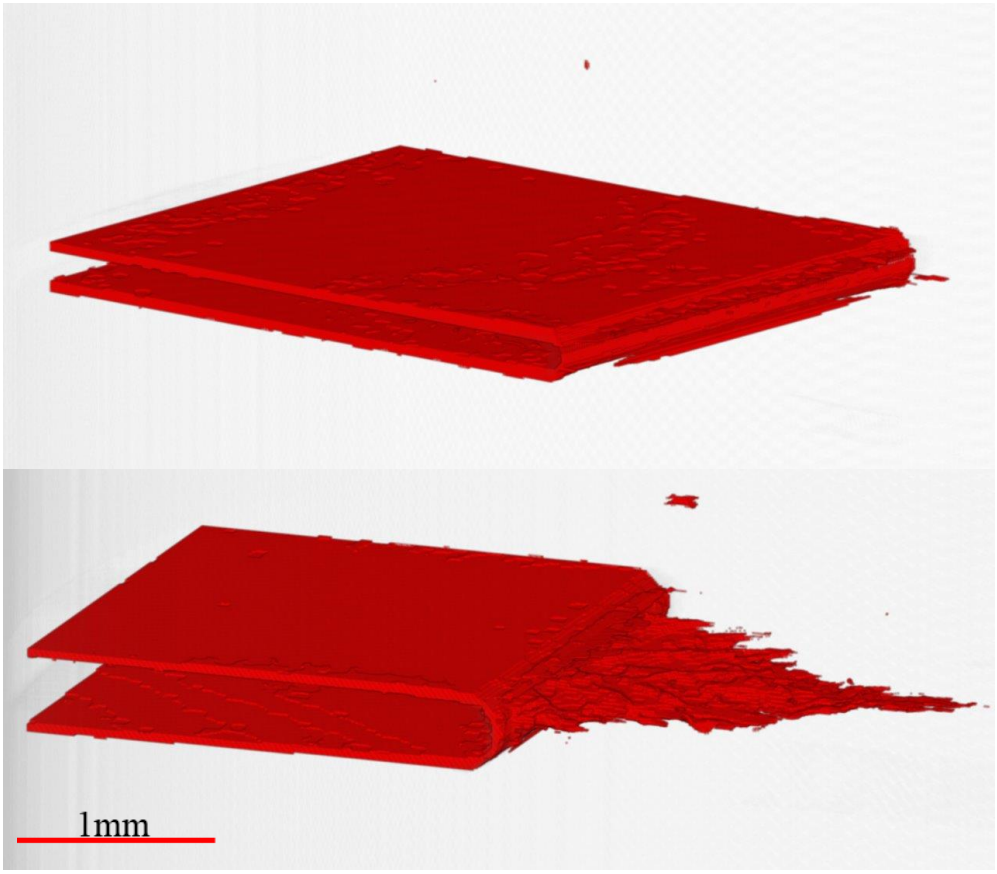

Figure 2.5: XCT scans showing crack tunneling behavior. a) Low load before crack initiation, b) Crack has initiated at the mid-plane, but growth is not visible at the surface

To confirm the crack tunneling behavior, a series of tests using X-ray Computed Tomography (XCT) scans were carried out for posthumous observation of the internal crack front profile. A high voltage of 150 kV was used due to the large size of the specimen. A voxel size of 10 microns was used for imaging. In Fig. 3.5a, a 3D image of the internal crack is shown under a small amount of load

prior to crack initiation. The pre-cut notch is highlighted in the figure. After a sufficiently large load has been applied so that the tunneling occurs, but not cause initiation at the surface, Fig. 3.5b shows the crack tunnel approximately 2mm ahead of the crack on the surface.

To mitigate these problems, the grooved specimen geometry was adopted [26]. The recommended groove thickness is approximately 80% of the total thickness. In this work a groove was cut so that the groove thickness is 66% of the total thickness in order to ensure the EDM could properly cut the groove with sufficient consistency. The revised grooved geometry minimized prevented crack kinking adjacent to the surface to produce shear lips. Additionally, the crack tunneling was minimized as seen by the flat and symmetric fracture surface seen of the specimen. Experiments after the groove was added did not result in crack kinking. Unlike the non-grooved specimens, the load vs. load-point displacement plot was smooth and increased monotonically up to visible crack initiation on the surface. Examination of the fractured surface did not show large-scale shear lips adjacent to the specimen surfaces or other indication of crack tunneling. Therefore, it was resolved that the side grooves successfully minimizes the crack tunneling behavior. While some challenges related to elastic-plastic effects remained making the LEFM model not suited for this work despite the side grooves, the identification of the correct crack tip location is now possible with precision by observing the surface of the specimen.

3.2 Specimens for Dynamic Study

Unlike quasi-statically loaded the three-point bend specimens, the geometry for the high-strain rate specimens is constrained by the available high-strain rate testing equipment namely, the split-Hopkinson Pressure Bar (SHPB). A geometry with built-in loading pins was used previously for high strain rate fractures to study additively fabricated Ti-6Al-4V alloy [36]. In light of this, the loading and support pins are printed into the specimen directly to allow for use with a flat loading surface of SHPB. Because of the design on these pins, the imposed pressure on the specimen must be uniform to ensure the pins do not bend or break during experiments without producing crack initiation. If too little pressure is used the specimen will not have enough energy to cause the crack to deform, initiate and propagate. The correct pressure is between these two extremes and can be found using trial and error. Additionally, increasing the length of the notch inserted into the specimen as needed can help the specimen fracture with less energy. In this work, a 5mm length notch was found to be appropriate. The dimensions of the dynamic specimen and the attached loading pins are shown in Fig. 3.6.

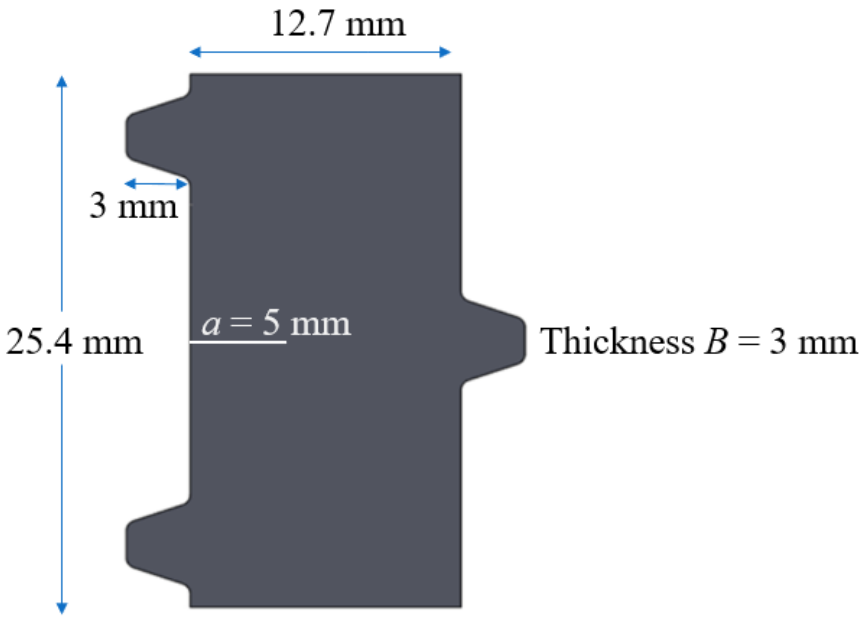

Figure 3.6: Schematic diagram of the high strain-rate specimen geometry

Like in the quasi-static test specimens, the notch was added using wire EDM. A wire with a rated diameter of 0.004 inches (~100 microns) was used to cut the notches. The resulting notch was approximately 100 microns wide. The crack tunneling behavior seen in the early static experiments was also present under dynamic conditions. Fracture parameter history (measurement details to be discussed in Chapter 4) also showed a distinct drop prior to the appearance of the crack on the surface. Crack kinking and shear lip formation were also visibly present by posthumously examining the specimen. Therefore, a pair of side grooves was added to the front and back faces at the mid-span. Crack tunneling was thus mitigated by these grooves. The same procedure as in the quasi-static counterparts was used for the dynamic ones to machine the grooves. The specimens were carefully polished using 80 grit sandpaper, rinsed, and then cut with a 0.010 inch (~250 micron) diameter wire. The depth of the groove was 0.5 mm on each side resulting in a minimum thickness of 2 mm.

3.3 Manufacturing Conditions

IN-718 specimens are manufactured using laser beam powder bed fusion (LPBF) additive manufacturing in a EOS M290 printer. This process requires the material to be turned into a powder through a process called atomization. Two atomization processes were used in this work: plasma atomization and nitrogen atomization. These atomization processes result in metal powders with an average particle size of 15-53 microns. The chemical composition of these powders was made to be in accordance with the constraints of ASTM standard F3055 [37]. The

specific composition is shown in Table 3.1. The chemical composition of the powder was measured using ASTM testing method standards E1097 and E1019 [38-39].

Table 3.1: Chemical Composition of IN-718 used in this work, from ASTM standard F3055

Ni	Fe	Cr	Nb + Ta	Mo	Ti	Al	Other[1]
52.5%	19.0%	18.5%	5.0%	3.0%	0.9%	0.6%	< 0.1%

Additionally, the hatch distance, stripe width, layer thickness, and build orientation are controlled during printing. These parameters are displayed in Table 3.2. The build orientation is horizontal such that the side of the specimen that receives the loading pin is oriented towards the build plate, and the side where the notch is inserted is facing away from the build plate. This is the same for both the quasi-static and high strain-rate specimens.

Table 3.2: Controlled Manufacturing Parameters

Build Orientation	Horizontal
Hatching Distance	110 microns
Stripe Width	10 mm
Layer Thickness	40 microns

The effect of three different manufacturing variables is tested in this work: shielding gas, heat treatment, and laser process parameter. Specimens that were manufactured from plasma atomized powder used argon as the shielding gas during production. Specimens from nitrogen atomization used nitrogen gas as the shielding gas during production. After printing, the specimens are heat treated to

[1] Other elements included in descending order are: Co (< 0.1%), Cu (< 0.1%), C (0.04%), Si (0.04%), O (0.017%), N (0.012%), Mn (0.01%), P (0.005%), Bo (0.004%), and S (< 0.001%)

remove any residual stress. Heat treatment procedures were determined based on ASTM standard F3055 and AMS 2774 [37, 40]. The heat treatment process has three steps: Stress Relief (SR), Solution Annealing (SA), and Double Aging (DA). Two different heat treatment processes were conducted as shown in Table 3.3 and are visually compared in Fig. 3.7.

Table 3.3: Heat Treatment Procedures

Heat Treatment	Stress Relief	Solution Annealing	Double Aging
Heat Treatment 1	1065° C, 1.5hr	1065° C, 2hr	760° C, 10hr + 649° C, 20hr
Heat Treatment 2	1065° C, 1.5hr	970° C, 2hr	760° C, 10hr + 649° C, 20hr

The Laser Process Parameter (LPP) is varied as well. In LPBF, two kinds of defects form as a result of the LPP. Keyhole defects form as a result of an overpowered laser that melts through more than a single layer of the material.

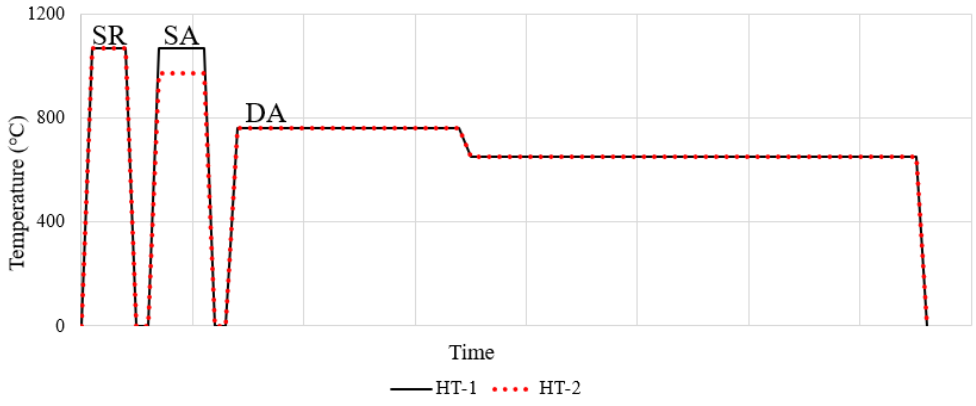

Figure 3.7: Three-phase heat treatment procedures

Lack of fusion defects occur when the laser is underpowered and fails to properly melt and fuse the layers together. Fig. 3.8 shows images of these defects

taken at 500X magnification and EHT = 5.00 kV with a scanning electron microscope (SEM).

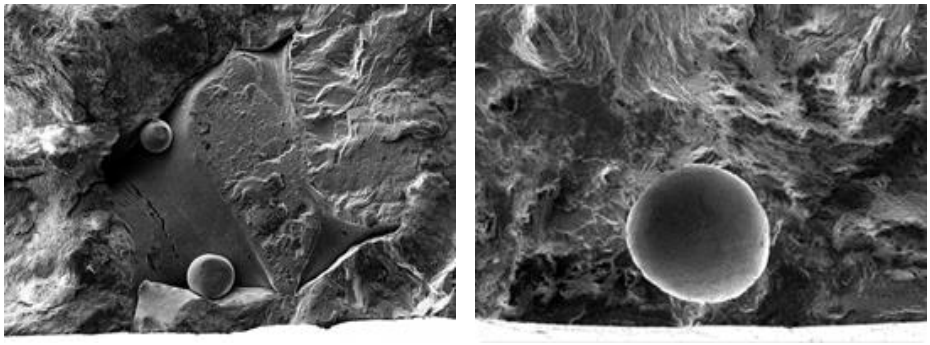

Figure 3.8: SEM images of a) lack of fusion defect, b) keyhole defect, taken at 500X magnification

To study the effect of these defects, three laser parameters are chosen: An overpowered LPP for keyhole defects, and underpowered LPP for lack of fusion

defects, and a middle LPP called “recommended.” Increasing the power output of the laser itself as well as slowing the scanning speed induces more keyhole defects and fewer lack of fusion defects. Decreasing the power output of the laser or increasing the scan speed reduces the number of keyhole defects and induces more lack of fusion defects. By varying these two parameters, an LPP to induce defects approximately equal in size (50-100 microns) in Argon and Nitrogen gas specimens can be found. Defect size was measured using X-ray computed tomography (XCT) scanning. By visual inspection of the XCT scans the number of defects present is approximately equal for both shielding gases. Defect size and count were measured in test coupons in as-built conditions, prior to heat treatment. The LPP settings are shown in Table 3.4.

Table 3.4: Laser Process Parameter Settings

Defect Induced	Laser	Ar Scan Speed	N2 Scan Speed

Keyhole (KH)	313.5 W	768 mm/s	768 mm/s
Lack of Fusion (LoF)	199.5 W	1056 mm/s	960 mm/s
None (Recommended)	285 W	960 mm/s	960 mm/s

There are 12 unique specimen manufacturing conditions that are created by varying the shielding gas, heat treatment and laser parameter. The effect of these 12 manufacturing conditions on the fracture properties of IN-718 will be studied in quasi-static and high-strain rate fracture. The objective is to determine the importance of each manufacturing parameter and to evaluate which settings are advantageous in comparison to the others. In this work, the manufacturing conditions will be abbreviated using a three-character shorthand. The first character will be A or N to denote the Argon or Nitrogen shielding gas used. The second character is 1 or 2 to denote the heat treatment. The third character is R, L, or K to denote the laser process parameter as recommended, lack of fusion, or keyhole. For example, a specimen manufactured with the condition A1R is made using Argon shielding gas, heat treatment - 1, and the recommended laser parameters.

Chapter 4: Experiment Details

The experiment setup and procedure for both quasi-static and high-strain rate tests are detailed in this chapter. Photographs and schematic diagrams are included to show the equipment used in each experiment. There are several considerations that ensure correct capture of DIC data which are explained in detail in section 4.1. The quasi-static experiments are described in section 4.2, and the high-strain rate experiments are described in section 4.3.

4.1 Digital Image Correlation

Digital Image Correlation (DIC) is an optical technique for measuring surface deformations using a digital camera and subsequent post-processing of recorded gray scales. There are many advantages to using DIC over alternative methods. Because DIC is an optical method it is a non-contact technique and does not require any transducers that come in contact with the specimen. Additionally, DIC is a full-field method which records the deformations at a large number of discrete points on the specimen simultaneously and records this deformation in two dimensions in the plane of the specimen or in three dimensions if stereo DIC is used. Strain gages and extensometers, on the other hand, typically make measurements only over a small area and hence are pointwise methods. Finally, with the use of ultrahigh-speed cameras, DIC is capable of measuring data previously unattainable in high strain-rate experiments. For these reasons, DIC is widely used and is employed in this work.

The rise of DIC in popularity has led to a variety of DIC-based measurement techniques, namely 2D DIC and stereo (3D) DIC. In 2D DIC, a single camera is used to capture planar or in-plane surface deformations of the specimen. This method is sufficient for many applications where specimens 2D, or where out-of-plane deformations are not present or are negligible. Stereo DIC utilizes two cameras offset from each other to record the specimen surface. This method operates on the same principle as binocular depth perception and can measure the out-of-plane and planar deformations by combining the recorded data of both cameras. The advantage of this method is that measurements can be taken along an additional out-of-plane axis, which can be beneficial if the recorded specimen does not have a flat surface or if out-of-plane displacements are large. A drawback of this is that two cameras are required, needs to be calibrated for each case and can be expensive with specialized high-speed camera equipment typically used during high strain-rate testing. In this work, only 2D DIC is used for both quasi-static and high strain-rate experiments.

The DIC method measures the deformation of a specimen by subdividing the recorded image into sub-images (also called facets) in the reference state to be correlated with their location in the image corresponding to the deformed state. In this work, the reference image was taken to be the one in the no-load state. The specimen being recorded is coated with a random pattern so that each sub-image contains a unique pattern. The DIC method has been used with a variety of different random patterns. Common techniques include the use of spray paint to generate random speckles, as well as random speckle generators that can be printed onto a

specimen. Rollers and stamps have also been used to apply a pattern using ink. With any method of applying a DIC pattern, an important consideration is the size of the features applied and variation in the gray scale between neighboring pixels. Speckles or dots should be large enough to span across multiple pixels in the image, but small enough so that multiple speckles will be contained in a single sub-image. Therefore, the speckle size must be carefully controlled so that they are neither too large nor too small. Typically, for a chosen magnification, speckles that span 3-6 pixels is considered optimal. Additionally, the gray scale resolution of the camera sensor (typically 8-bit to 12-bit range) is useful in the image correlation.

After images are recorded at different load-steps, an image analysis software is used to correlate the deformed images with the reference image. The computer code will take each individual sub-image from the reference image and find the corresponding location of the same sub-image (group of pixels with different gray scales) in the deformed image by matching the pattern of gray scales in the image, as shown in Fig. 4.1. This procedure starts by correlating each image with a specifically chosen sub-image called the start point sub-image. Once the location of the start point sub-image is found in the deformed image, the subsequent sub-images—starting with the sub-images adjacent to the start point and continuing outward as the process completes—are identified by the pattern of speckles and their position relative to the start point sub-image to speed up the correlation program. Once the location of every sub-image has been found in the deformed image, comparing its position to the position in the reference image allows the displacement of that point to be calculated. The units of pixels in the image are

converted to the actual scale by multiplying by a scale factor or magnification factor.

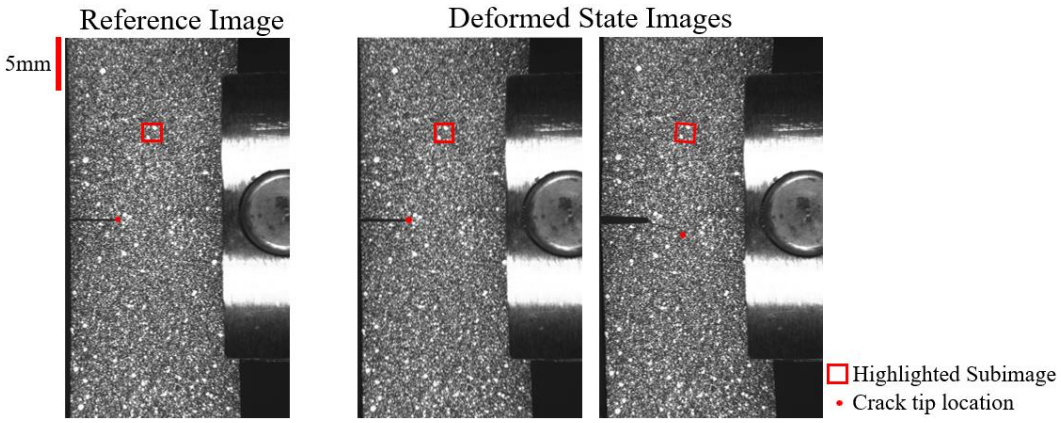

Figure 4.1: Correlation of an example sub-image using DIC

In this work, a random speckle pattern was applied to the surface of the specimen using black and white spray paints. Rust-oleum semi-gloss protective enamel spray paints in pressurized aerosol cans were used in this work. These paints were effective for DIC because it can be applied easily to the specimens and correlated well in the lighting environment for these experiments. Images were recorded throughout the experiments so that the displacement of each sub-image can be correlated at various stages of specimen deformation. The paint was sprayed from a distance of approximately 50 cm to create a fine speckle pattern with features 100-500 microns in size. The size of the speckles can be controlled by the distance between the target surface and the nozzle tip because smaller particles of paint will reach a farther distance. The resulting features cover approximately 5-25 pixels in the images captured. The paints are balanced so that an even amount of black and white speckles is present throughout the region of interest on the specimen.

In DIC, the sub-image size and spacing can also be critical for extracting useful data from the image series. To determine the best inputs for experiments, sub-image size was varied for one experiment until a size could be found that minimized noise. Taking a N1K quasi-static experiment as the trial case, the same image series was correlated choosing a sub-image size of 20×20, 30×30, 40×40, and 50×50 pixels. The spacing and overlap of neighboring subsets were kept constant at 10 pixels for all of these analyses. The resulting displacement data was then used to extract the energy release rate for each of these subset sizes. For the smaller subset sizes of 20×20 and 30×30, there is a higher degree of noise in the data than for larger subset sizes of 40×40 and 50×50. There is no significant reduction in noise when increasing the subset size from 40×40 pixels to 50×50 pixels. Therefore, a subset size of 40×40 pixels was used for all quasi-static experiments. Because of the lower resolution and higher scale factor of the ultrahigh-speed camera used for high-strain rate experiments, the sub-image size was reduced to 30×30 pixels and the spacing was reduced to 5 pixels for the high-strain rate experiments.

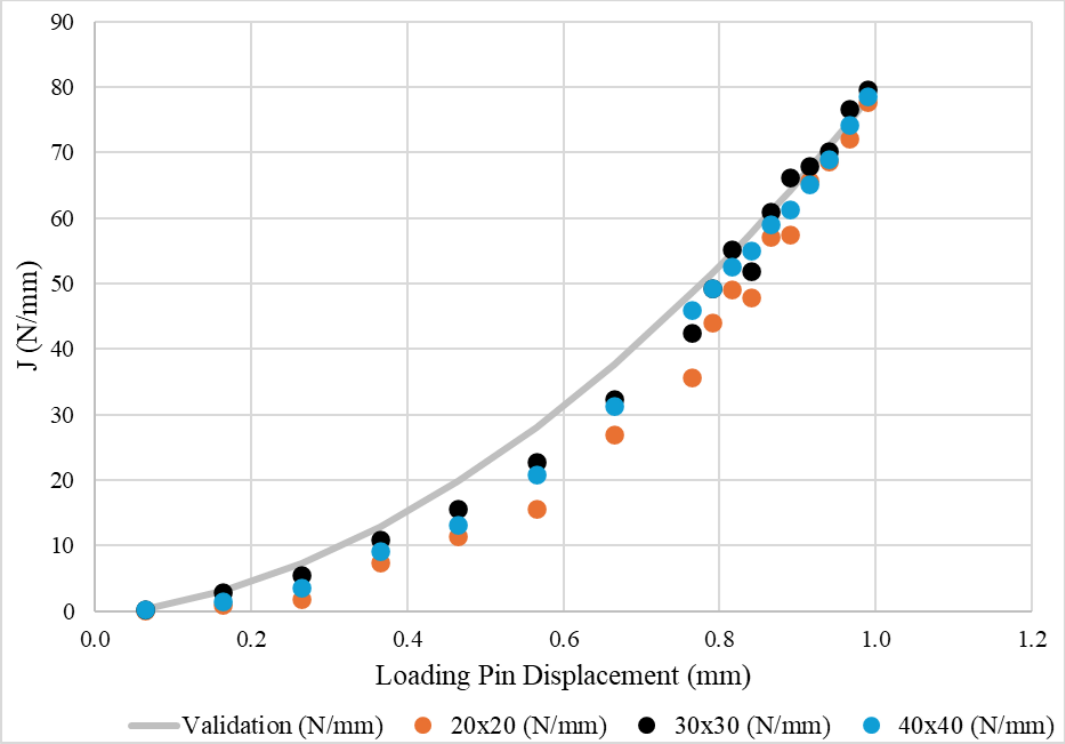

Figure 4.2: Comparison of sub-image size for 20×20, 30×30, and 40×40 sub-images.

In DIC, uniform lighting is important for accurately correlating the captured images. If some parts of the specimen surface are poorly lit or in the shadow, a region of speckles may deform from a brightly lit area to an area covered in shadow. This causes white speckles to suddenly appear dimmer, and as a result that region may not correlate accurately. Therefore, uniform lighting across the entire surface of the specimen is needed. While ambient lighting may be bright enough for most cameras with a sufficiently low frame rate, this is not recommended because it leads to uneven lighting. Using a lamp to illuminate the specimen helps resolve this, but having only a single light source can lead to bright and dim regions. It is best practice to use at least two lamps positioned close to the specimen and arranged to illuminate the specimen evenly. For high strain-rate experiments when an

ultrahigh-speed camera is used, high-energy flash lamps are needed to illuminate the specimen surface with sufficient brightness to achieve satisfactory exposure over a short period.

Brightly illuminating the specimen has the added benefit of allowing the camera lens to be set with a small aperture opening. Alternatively, if a specimen is poorly lit, the aperture needs to be opened wide to achieve satisfactory exposure. A wide aperture results in a smaller depth of focus. This results in the edges of the image to have poor focus. In order to capture an image that is well-focused throughout, a small aperture and bright illumination is needed. Magnification must also be considered while setting up a camera for DIC. Increasing the magnification often decreases noise and increases the clarity of a particular region of interest. However, this can increase the number of pixels a feature covers and therefore requires a larger sub-image size during the post-experiment correlation step. Magnification factor must also be balanced with the depth of focus to make sure the entire region of interest on the surface of the specimen is captured without the edge of the image being out of focus.

Once these factors are taken into consideration, DIC is a powerful optical technique for measuring surface deformations. It can be readily applied to many experiments on a wide range of materials. The many benefits of using DIC rather than other experimental methods has led to its widespread use now.

4.2 Quasi-Static Experiments

To test the fracture behavior of specimens under quasi-static loading conditions, a three-point bending setup is used. An Instron 5982 mechanical testing

machine with a 100 kN load cell was used to measure the load as the specimen bends. Specimens are tested at room temperature and elevated temperature effects are not considered in this work. The specimen is positioned symmetrically between two support pins with a span of 70mm. The specimen is precisely aligned in the loading apparatus so that the loading pin is directly in-line with the notch and grooves at the mid-span of the specimen and the base supports are equidistant from the notch. The loading pin displaces the specimen at a rate of 0.05 mm/s throughout the loading sequence. During the loading sequence and fracture event, the specimen is illuminated with a pair of fluorescent lamps and recorded by a digital camera at 2 fps. It should be noted that the camera records as a 10-bit camera, but images are exported as 8-bit .jpeg images for compatibility with the ARAMIS software used. The lighting was adjusted such that the grayscale image of the specimen has an average brightness of approximately 60%, ensuring an even balance and a normal distribution in the brightness of speckles. The optical details of the imaging device and image correlation can be found in Table 4.1. When the crack initiated, it propagated along the path of the groove in a self-similar fashion, successfully restricting the crack growth to mode-I and preventing macroscale crack kinking, tunneling and mitigating shear lip formation.

Table 4.1: Image details for quasi-static experiments

Hardware Parameters		Analysis Parameters	
Camera Manufacturer	Point Grey	Software Package	ARAMIS v6.3.1
Camera Model	Grasshopper3 GS3-U3-41C6M	Software Manufacturer	GOM
Image Resolution	2048 x 2048 px	Image Filtering	None
Lens Manufacturer	Computar Lens	Sub-image Size	40 px

Focal Length	18 - 108 mm	Step Size	10 px
Field of View	40 x 40 mm	Subset Shape Function	Affine
Image Scale	0.02 mm/px		
Stand-off Distance	50 cm		
Image Acquisition Rate	2 fps		
Patterning Technique	Spray Painted		
Approx. Feature Size	5 px		

For many of the grooved specimens, the fracture occurred abruptly and the crack propagated all the way through the specimen quite rapidly. In these cases, no post-initiation data could be recorded due to the crack speed and the slow recording rate. However, in a few cases, the crack initiated and propagated somewhat slowly so that the post-initiation behavior could be captured and subsequently analyzed. The post-initiation crack resistance results are discussed in detail in section 5.3.

These experiments show a high degree of repeatability. Two N1R specimens are shown in Fig. 4.3. The final fracture load is approximately 10kN for both specimens, within >1% deviation. This shows that the experimental procedure is repeatable for quasi-static specimens.

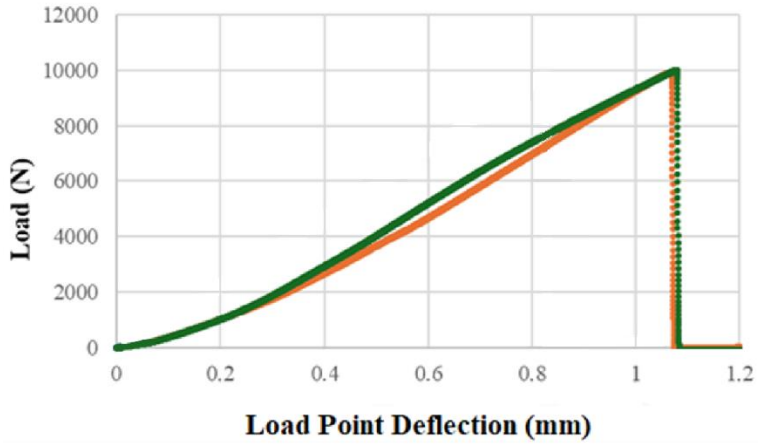

Figure 4.3: Repeatability of N1R quasi-static specimens

After the experiments were conducted and the data was recorded, selected images are correlated using ARAMIS image analysis software. Analyzing all recorded images would have resulted in excessive data processing, so one in every ten images was selected to analyze the recorded data. The reference image was taken as the first image captured in the series, before the loading pin started to displace and subject the specimen to bending moment. To account for slack and tolerances built into the loading fixture, images prior to the load of 0.3 kN are ignored. Therefore, the point of contact of the loading pin onto the specimen is considered to be the point where the nominal load is 0.3 kN. Subsequent load and loading pin displacement values are normalized relative to this point. Most specimens failed at a load of approximately 10 kN and hence any error due to 0.3 kN treated as the reference is assumed negligible. The analyzed results are presented and discussed in greater detail in Chapter 5.

4.3 High Strain Rate Experiments

In high strain rate experiments, specimens are tested in a compression split-Hopkinson pressure bar (SHPB) apparatus. This is shown by a schematic diagram

in Fig. 4.6. The incident and transmitted bars are made of maraging steel and are 8 feet in length each. The diameter is 1 inch. The bars are held in place by pillow block bearings and lubricated using graphite powder to allow them to slide without significant friction.

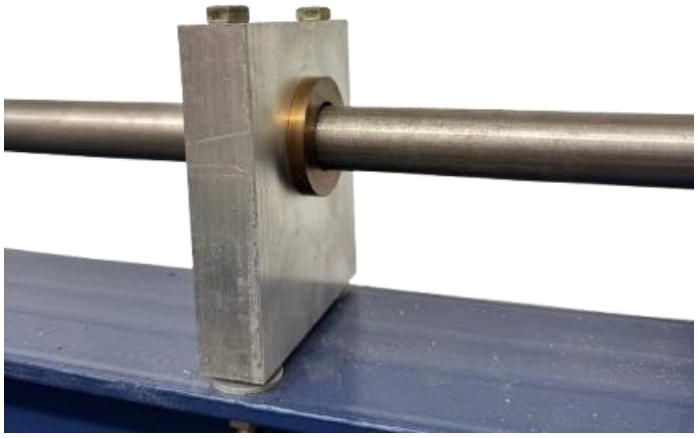

Figure 4.4: Image of the incident bar resting in the pillow block support

A 12 inch long maraging steel striker rod is fired from the gas-gun, pictured in Fig. 4.5; the gas chamber pressure of the apparatus is ~55 psi. The resulting striker velocity is approximately 12 m/s at impact on the incident bar. The striker impacts the incident bar and sets off stress waves to travel through it. The length of the incident bar ensures that a uniaxial loading wave that will propagate through the specimen and then into the transmitted bar. Thus, the striker impact loads the specimen dynamically and causes it to fracture.

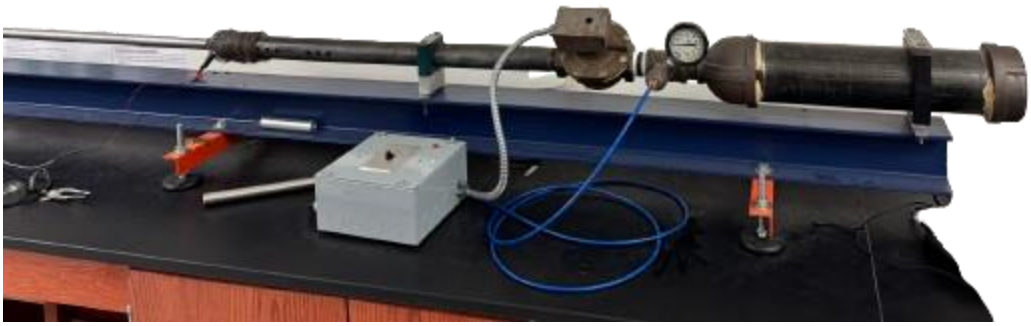

Figure 4.5: Photograph of the gas-gun apparatus aligned with the incident bar of SHPB

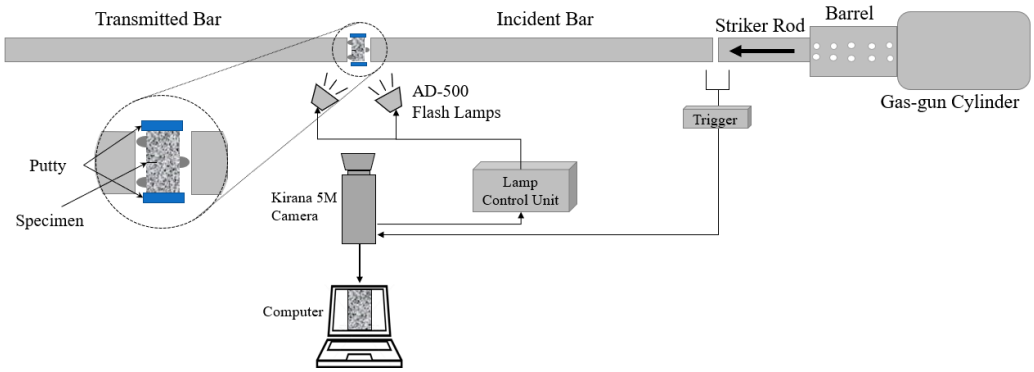

Figure 4.6: Schematic of split-Hopkinson pressure bar apparatus

The specimen is held in place between the two long bars. Small strips of putty are attached to the top and bottom of the specimen and an adjustable height supporting table is placed underneath the specimen. Putty allows for the specimen to freely move even with the placement of the support table. This supporting table is gently placed to ensure the specimen is held only by the two long bars, not held up by any force from the table. Without this support table and putty, vibrations from the gas-gun can cause the specimen to slip down during experiments.

Figure 4.7: Specimen held in place between the incident and transmitted bars with putty and support table

This stress wave loading event lasts approximately 350μs in total. Using a Kirana-5M ultrahigh-speed camera, 180 images are taken at 400,000 fps. The camera has a 924x768 pixel resolution and images are saved as 8-bit .jpg files. The experiment is illuminated using two AD-500 high power flash lamps. These lamps use 500 J of energy and have a flash duration of 2 milliseconds. The camera and flash lamps are timed to trigger just before the stress wave travels through the specimen. The trigger detects the contact between the striker rod and the incident bar. Steel wool is wrapped around the barrel of the gas gun and conductive tape is attached to the face of the incident bar, as shown in Fig. 4.9. Alligator clips are attached to the steel wool and the tape and are connected to a close circuit detector. When the striker makes contact with the face of the incident bar, the trigger detects the closed circuit. A built-in time delay is synchronized so that the camera and flash lamps fire at the time when the deformation and failure of the specimen are to occur. The camera, lens, and lamps are shows in Fig. 4.8.

Figure 4.8: Image showing set up of camera and flash lamp system

The same imaging/photography considerations as in the quasi-static experiments are necessary here. The lighting and aperture are adjusted so that the average brightness of the specimen is approximately 60%. The magnification and focus are carefully set so that the entire image is in sharp focus and so that the speckles cover approximately 5 pixels. Due to the size of the specimen and the camera placement, for the high strain-rate experiments the scale factor is approximately 0.035 mm/pixel. The other details regarding imaging and DIC are shown in Table 4.2.

Table 4.2: DIC details for high strain-rate experiments

Hardware Parameters		Analysis Parameters	
Camera Manufacturer	Specialized Imaging	Software Package	ARAMIS v6.3.1
Camera Model	Kirana 5M	Software Manufacturer	GOM
Image Resolution	924 x 768 px	Image Filtering	None
Lens Manufacturer	Nikon	Sub-image Size	40 px
Focal Length	80-400 mm	Step Size	10 px
Field of View	32 x 27 mm	Subset Shape Function	Affine
Image Scale	0.035 mm/px		
Stand-off Distance	50 cm		
Image Acquisition Rate	400,000 fps		
Patterning Technique	Spray Painted		
Approx. Feature Size	5 px		

Due to slight variations in the firing of the gas-gun and contact of the striker rod with the conductive tape, there are slight differences in the timing of the images. Fig. 4.9 shows the conductive tape as it is placed on the incident bar and the lamp trigger system.

Figure 4.9: Conductive tape trigger system at the barrel of the gas gun

Two alligator clips are positioned on the conductive tape and on the steel wool around the barrel of the gas gun to detect the closed circuit and fire the camera. In the image sequence, the first 15-30 frames are not optimally illuminated as it takes some time for the flash lamps to reach its full power. A fully illuminated frame after the lamps reach full brightness is used as the reference image. In this image the incident bar is not yet moving, and the stress waves have not yet reached the specimen. All subsequent images are correlated with the reference and analyzed subsequently. The image series captures the entire fracture event, and the critical value energy release rate J_c at the point of crack initiation as well as post-initiation crack growth behavior can be analyzed. Detailed results are shown and discussed in section 5.4.

Chapter 5: Results

The results for experiments which have been outlined in Chapter 4 are presented in this chapter. Two stress intensity factor (SIF) extraction techniques are used. The first is the least-squares error minimization procedure as described in Chapter 2. Because of the clear benefits of the combined fields method, that technique will be employed rather than the legacy approach, and these results are shown in section 5.1. The second extraction technique is a hybrid DIC-Finite Element (DIC-FE) method. This technique relies on the use of finite element (FE) analysis to extract fracture parameters from measured DIC data. This method has several advantages over the least-squares method for use with ductile materials which may deform significantly and preclude the use of LEFM assumptions. For these reasons the DIC-FE method is the primary extraction method used for obtaining the results for IN-718 alloy. DIC-FE results for quasi-static experiments in section 5.1, and for high strain-rate experiments in section 5.3.

5.1 Least-Squares Approach

The first extraction method is the least-squares error minimization method. This method is a common method for extracting stress intensity factors (SIFs) such as K_I and K_{II} in full-field optical experiments which fall under linear elastic fracture mechanics (LEFM) assumptions. This technique and its benefits are already discussed in great detail in Chapter 2. It also compared two ways of extracting SIFs from this method and the advantages of the combined fields technique when using this extraction method. For the reasons explained in Chapter 2, the current section will only use the combined fields method to obtain the results.

A crucial assumption when using the least-squares extraction method is that linear elastic fracture mechanics in the region of interest govern the crack tip deformation field equations. It is assumed that the region of interest selected in the displacement field analysis is heavily influenced by crack tip effects, and that the deformations are elastic in nature. To ensure this assumption is true, a plastic zone in the immediate vicinity of the crack tip is typically excluded from the analysis which also often helps to eliminate dominant triaxial or 3D effects as well avoid large error in the measurement of the radial distance from the crack tip to the nearby data points. Additionally, to exclude far-field effects, such as those due to loading pins, the region of interest is limited to within an outer radius where crack tip effects are dominant. Within the selected region, the assumption of LEFM must be valid.

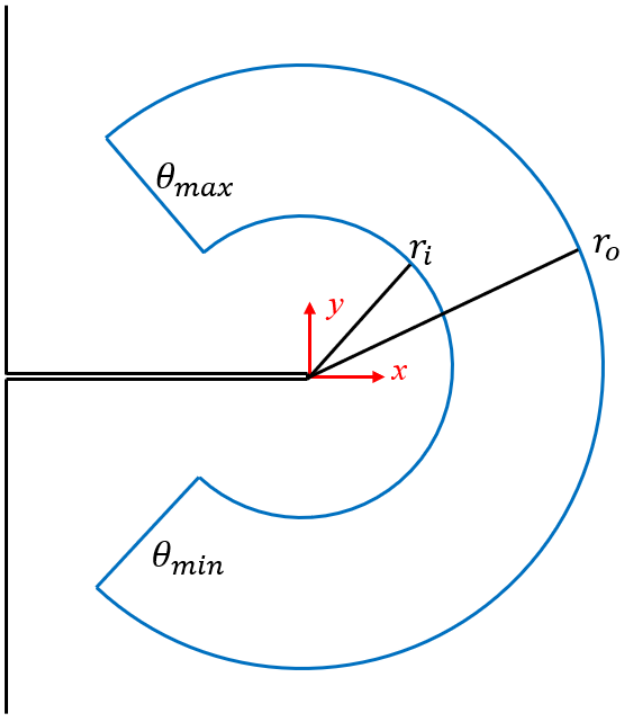

Figure 5.1: Schematic of region of interest for least-squares data analysis.

The selected region of interest is shown in Fig. 5.1. Here, the inner and outer radii are noted as r_i and r_o respectively. The angular bounds θ_i and θ_i are shown as well. The coordinate system is aligned so that the origin is at the crack tip and the positive *x*-direction is in the direction of crack growth. The region of interest is defined by using polar coordinates in this coordinate system.

Fig. 5.2 displays the extracted SIF (K_I) results for a quasi-statically loaded N1R specimen plotted as a function of applied load (P). The specimen is supported by two support pins with a span of 70mm. The width of the specimen is 22mm and the initial notch length is 5mm. Other details concerning the quasi-static specimen geometry and experiment procedure are described in sections 3.1 and 4.2 respectively. The region of interest used here is $0.75 < r/B < 2.0$ and $-135° < \theta <$

135°, as shown in Fig. 5.1. For validation, the closed form LEFM solution from Eq. 5.1 is shown in orange.

$$K_I = \frac{PS(3\alpha^{1/3}[1.99 - \alpha(1-\alpha)(2.15 - 3.93\alpha + 2.7\alpha^2)])}{2BW^{3/2}(1+2\alpha)(1-\alpha)^{3/2}} \qquad (5.1)$$

Here, K_I is the mode-I SIF, P is the load, S is the span of the supports, α is the ratio of crack length to width (a/W), B is the thickness, and W is the width of the specimen. This equation describes a linear relationship between SIF, K_I, and the applied load, P. The predicted SIF from this closed form solution and the extracted values from the quasi-static experiment are shown in Fig. 5.2.

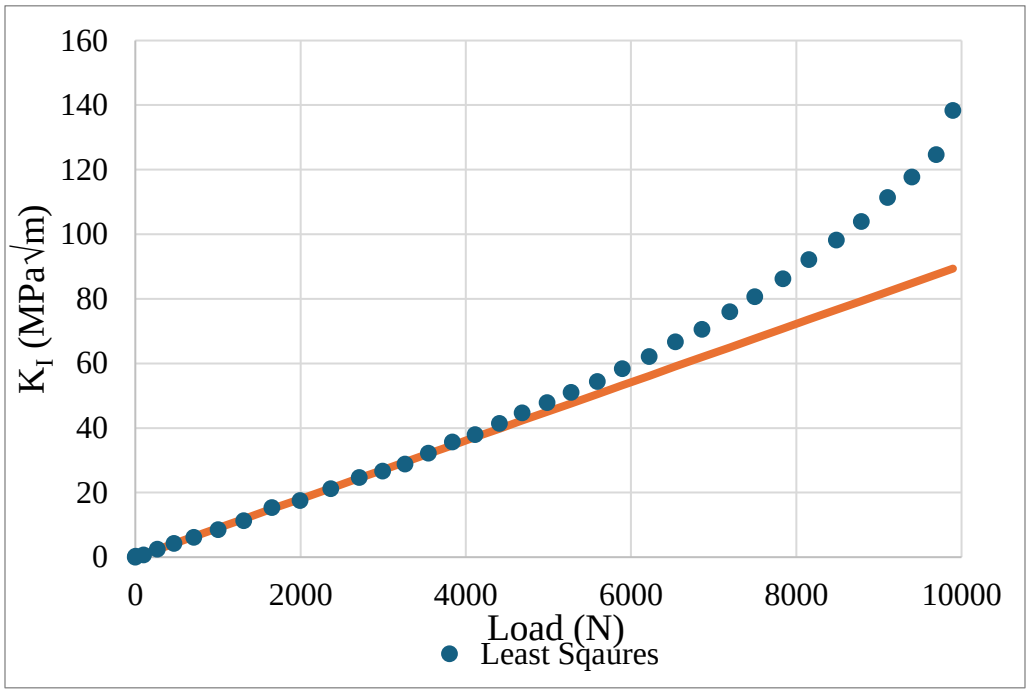

Figure 5.2: Variation of mode-SIF (K_I) with load showing a linear relationship in the elastic region before plastic effects cause the least-squares approach to

overestimate the prediction. The last data point corresponds to crack initiation.

Here, a linear relationship is seen between K_I and P at low load levels with an agreement of ~1% deviation with the closed form validation. At higher loads, plasticity effects become prevalent and can no longer be excluded from the selected region of interest. This causes a discrepancy between the value of K_I extracted using least-squares analysis and the value predicted by the closed form solution. The K_I values can be converted to energy release rate (J) by Eq. 5.2. Because these experiments are mode-I, K_{II} is negligible.

$$J = \frac{{K_I}^2 + {K_{II}}^2}{E} \approx \frac{{K_I}^2}{E} \tag{5.2}$$

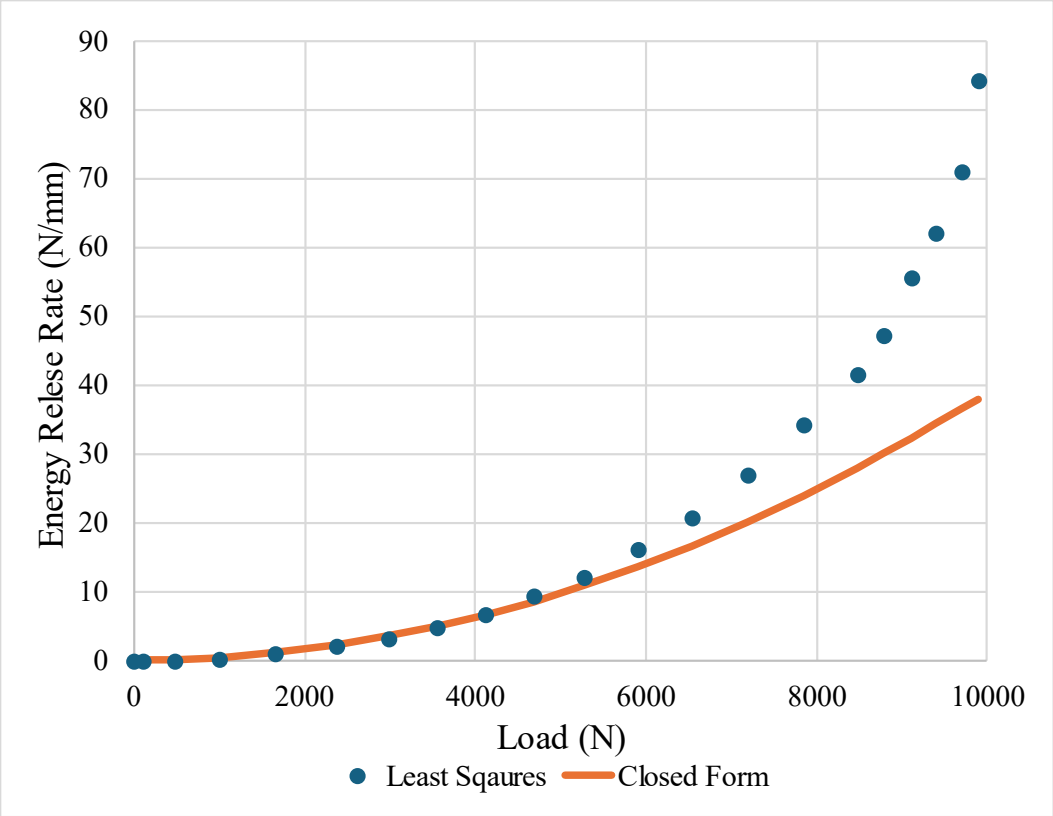

Figure 5.3: Energy release rate extracted using linear least-squares analysis for N1R specimen. The last data point corresponds to crack initiation.

In Fig. 5.1 and Fig. 5.2, the critical value corresponding to crack initiation is the final point with a load of 9900 N. It can be seen that ERR increases quadratically with load. In the elastic region when the load is below, say, 5000 N, the closed form solution validates the least-squares extracted data well. However, leading up to the point of crack initiation, the magnitudes of least-squares values diverge from the closed form counterparts. In this range, the extracted value again overestimates the closed form solution, indicating crack tip plasticity effects are to be accounted for in the data analysis.

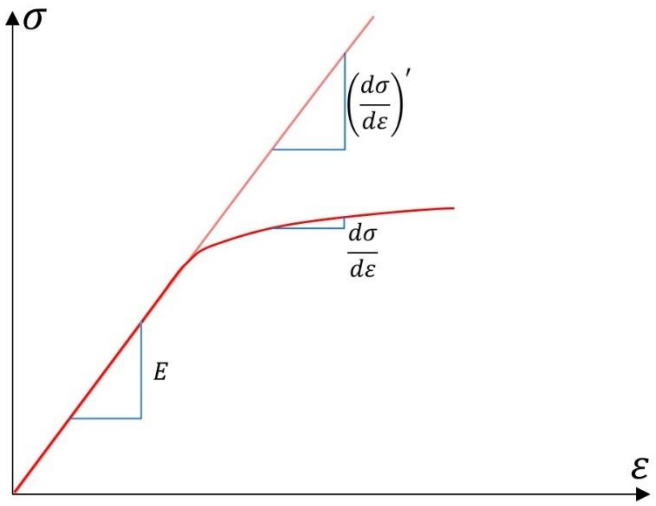

Figure 5.4: Illustration of the error leading to overestimation of fracture parameters when using the least-squares method and the LEFM assumption is violated.

In the plastic domain, the slope of the stress-strain curve, $\frac{d\sigma}{d\varepsilon}$, is less than the elastic modulus *E*. By conducting the analysis in this domain by assuming that the material undergoes elastic deformations only, the model expects the deformations to take more stress than is actually needed. This causes the extraction to overestimate the true stress intensity factor, as shown in Fig. 5.4. Here, $\frac{d\sigma}{d\varepsilon}$ is the true slope of the stress-strain curve in the plastic region, whereas $\left(\frac{d\sigma}{d\varepsilon}\right)'$ is the expected derivative, equivalent to the elastic modulus *E*. The error in the fracture parameter extraction is due to $\left(\frac{d\sigma}{d\varepsilon}\right)'$ being much greater than $\left(\frac{d\sigma}{d\varepsilon}\right)$.

From this, one can conclude that the LEFM assumption becomes invalid close to crack initiation. To limit the plasticity effects, the region of interest where the data is gathered can be adjusted. By excluding a larger region close to the crack

tip and extending the region of interest farther away one can possibly reduce the influence of plasticity effects. However, it was found by trial and error that this could not significantly reduce the influence of plastic effects. At the point of crack initiation, plastic deformation is present to such a large degree and hence no linear elastic region of interest that successfully extracted the correct SIFs and ERR could be found could be found. Fig. 5.5 compares the original extracted data (orange cirlces) of K_I vs Load with a reduced region-of-interest (blue circles) $1.0 < r/B < 2.0$ and $-135° < \theta < 135°$. While a slight reduction in plasticity effects is seen, it is still insufficient.

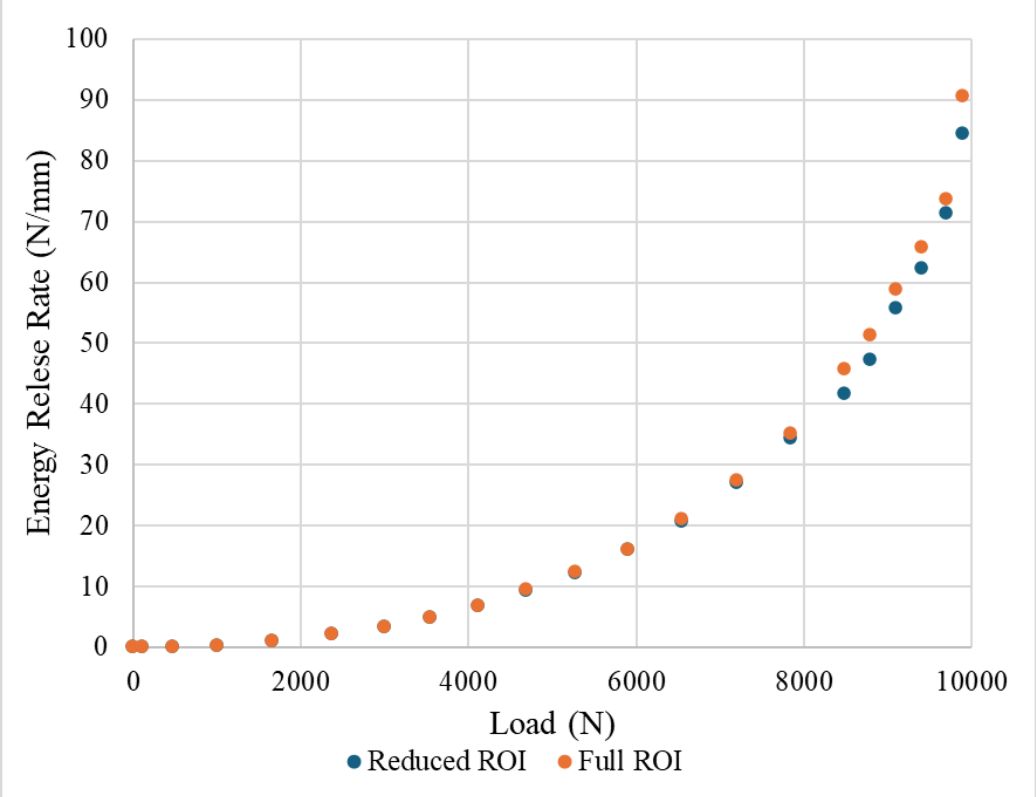

Figure 5.5: Effect of reducing size of ROI to mitigate plasticity effects. Full ROI is $0.75 < r/B < 2.0$. Reduced ROI is $1.0 < r/B < 2.0$.

Despite this, the DIC data from the experiment in the elastic region is validated by the closed form solution. However, the critical value (K_{IC}) is of great interest and cannot be accurately extracted using the least-squares approach in this case. Despite the advantages of the combined fields method as outlined in Chapter 2, a different, equally robust method must be adopted to account for plasticity effects present in the specimen.

5.2 DIC-Finite Element (DIC-FE) Method

The hybrid DIC-Finite Element (DIC-FE) method allows for the stress-strain response of the material to be measured in a tension test and applied as an elastic-plastic material behavior input to the finite element analysis. The major benefit of this method is that for materials with plastic deformations prior to crack initiation, the fracture toughness and post-initiation behavior can be reliably obtained. Although the energy release rate is computed in this method by evaluating the *J*-integral as [41],

$$J = \lim_{\Gamma \to 0} \int_{\Gamma} \left(W \delta_{1i} - \sigma_{ij} \frac{du_j}{dx_1} \right) n_i dC, \ (i,j = 1,2) \tag{5.3}$$

where, Γ is the path of integration encircling the crack tip, W is the strain energy density, σ_{ij} are the 2D components of the Cauchy stress tensor, u_j are the cartesian components of the displacement field, where u_1 is the *x*-displacement (u) and u_2 is the *y*-displacement (v), n_i are the components of the normal unit vector along the path of integration in the counterclockwise direction encircling the crack tip, and dC is the arc length along the path of integration. The *J*-integral is also expressed as a domain/area integral over the enclosed area of the integration path as,

$$J = \int_{\mathrm{A}} \left(-W\delta_{1i} + \sigma_{ij} \frac{du_j}{dx_1} \right) \frac{dq_1}{dx_1} dA, \ (i, j = 1,2) \tag{5.4}$$

where, A is the area of integration and q is a weighting function varying from 0 on the inner boundary to 1 on the outer boundary of the domain. In elastic analysis, this method allows for the *J*-integral to be separated into individual SIFs K_I and K_{II}. However, for elastic-plastic analyses, the mode-I and mode-II SIFs cannot be calculated. Because different regions in the material may experience different amounts of plasticity, one cannot extract individual SIFs, but only the energy release rate from the *J*-integral. This makes the method unsuitable for examining mixed-mode cracks if understanding the ratio of mode-I to mode-II is crucial and significant plasticity is present. For experiments in this work, the specimen geometry and loading condition was designed for mode-I crack initiation and growth, so the DIC-FE method can be readily applied to evaluate critical values of the energy release rate or the *J*-integral.

The stress-strain response of IN718 alloy is obtained by performing a tension test first. This test was repeated for all 12 manufacturing conditions as reported in chapter 3. This data is fed to the finite element analysis so that rather than only the elastic modulus and Poisson's ratio being used as elastic constants, the complete elastic-plastic stress-strain response is incorporated. From this complete material behavior data, a standard finite element model is constructed to validate the experimental results from the DIC-FE method. This validation model is a 2-D model of half of the specimen with a symmetry constraint imposed at the midspan over the uncracked specimen height. The loading pin and support pin are

modeled as rigid cylinders, and the contact is modeled as a surface-to-surface finite sliding contact with a friction coefficient of 0.5. The mesh size of the model is 0.2mm. This model is run 12 times using each of the material data sets for the different heat treatment and 3D printing conditions.

The standard FE validation model had very little variation (<0.4%) in the energy release rate between the different manufacturing conditions for the same displacement of the loading pin. This is because there is very little difference in the elastic-plastic stress-strain response of the different manufacturing conditions. This allowed all the manufacturing conditions to be averaged together into a single validation model. From this model, energy release rate can be expressed as a function of loading pin displacement and this function can be used to validate the DIC-FE results extracted from experimental data. In Eq. 5.5, the *J*-integral is the energy release rate in units of N/mm and *d* is the displacement of the loading pin in units of mm.

$$J = 68.202d^2 + 12.316d - 0.7721 \tag{5.5}$$

The DIC-FE method is based on applying experimentally measured displacement data to the finite element model as boundary conditions. To do this, the DIC grid, made of square subsets, is aligned with the mesh of the finite element model. The mesh size of the finite element model will be equal to the step size multiplied by the scale factor of the image used during DIC step. This ensures that every node on the finite element mesh will be matched with a corresponding subset from the DIC grid so that the measured deformation of each subset will be assigned as a displacement boundary condition to the corresponding finite element node. In

this work, the step size used is 10 pixels. The scale factor for quasi-static experiments is between 0.02-0.03 mm/pixel. Therefore, the element size in the DIC-FE model is between 0.2-0.3 mm. For dynamic experiments, the scale factor is 0.035-0.037 mm/pixel, and the element size is 0.175-0.185 mm. The convergence of the mesh is not a major concern in the DIC-FE method because the mesh size is predetermined by the image scale and DIC settings. Additionally, the displacement of every node is constrained by the boundary condition assigned to it. From these displacements the *J*-integral is evaluated to extract the energy release rate.

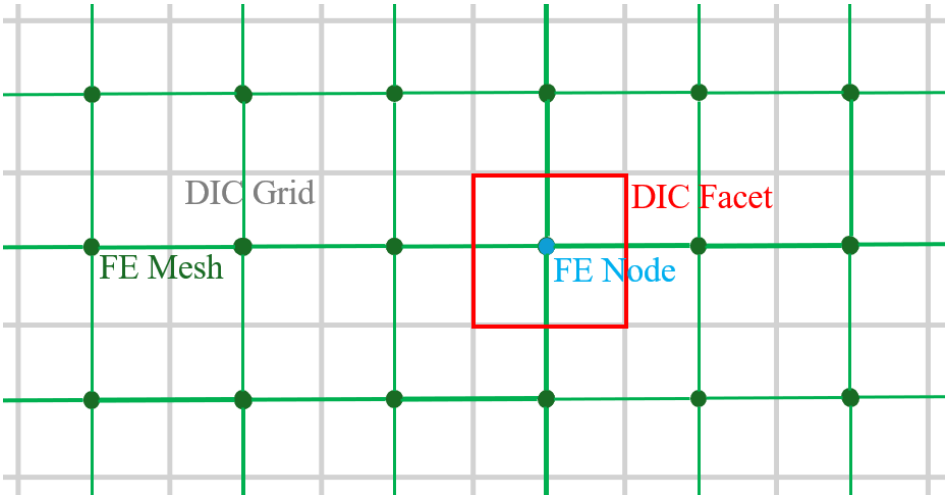

Figure 5.6: Alignment of DIC grid (gray) and FE mesh (green). An example of a finite element node is highlighted in blue, and the corresponding facet is highlighted in red.

The DIC-FE method is implemented using a series of scripts in MATLAB. Once the model has been constructed in ABAQUS finite element software, each node in the model can be exported as a .csv file, recording the node numbers and their *x* and *y* coordinates. Nodes close to the edges and the crack tip are excluded from this list because the DIC data in these regions contains too much noise. A

MATLAB script then assigns each node in the .csv file to the corresponding DIC facet from the DIC output data. In this way, each node and facet are paired because the spacing between the FE nodes is the same as the spacing between DIC facets. A new input file is created to assign the displacement of each DIC facet as a boundary condition to the corresponding node. These boundary conditions are included in the job input files and the *J*-integral is taken as the finite element output. All MATLAB scripts for this procedure is made available in Appendix C.

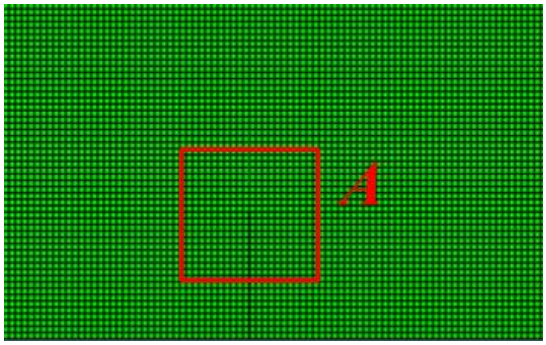

Figure 5.7: Contour path of the J-integral in the DIC-FE method. Contour number refers to the size of the path A as the number of sub-images included from the crack tip to the edge of the path.

In this work, the *J*-integral was evaluated for 50 contour paths around the crack tip, as shown in Fig. 5.7. The value for each can be plotted to determine the appropriate range for the region of interest. The values in this region are taken as an average to extract the energy release rate for each time step. The specimen N2R condition is used as an example to generate a plot showing the value of the *J*-integral for each contour in Fig. 5.8. The highlighted region indicates the selected region which is averaged to find a value for energy release rate at this specific load step. This region was selected because it contains a relatively constant extracted

value. The region closer to the crack tip is excluded from the analysis due to the high noise in the data of DIC sub images which contain the notch or crack tip. The region beyond this is excluded due to the high noise visible in the extracted values of the *J*-integral caused by the integral path including reaching too far away from the crack tip and including far field effects, edge effects, or loading pin effects.

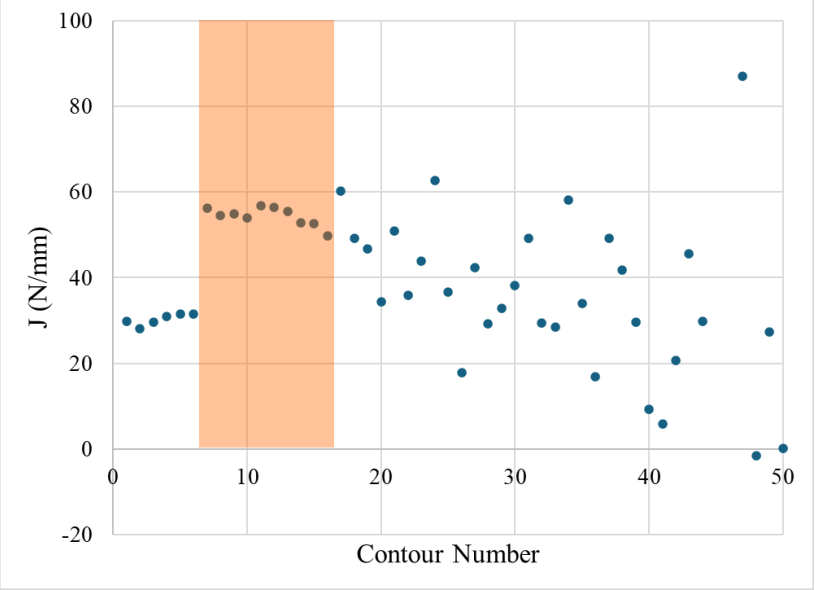

Figure 5.8: Extracted *J*-integral values for each contour in an N1R experiment. The region of interest highlighted is from 1.6mm to 4.1mm.

Here the region of relative stability exists from contours 7 to 18, which are averaged to extract a value of J = 54.4 N/mm. This region corresponds to a radius of 1.6mm to 4.1mm.

5.3 Quasi-Static Results

After conducting fracture experiments on edge notched beams in three-point bending configuration, the fracture parameters can be extracted from DIC data using two primary methods. The first is an over-deterministic linear least-squares analysis. This approach assumes that linear elastic fracture mechanics is

applicable to the deformation data in the region of interest near the crack tip. However, when significant plastic deformations are present in the region of interest, this method will not extract accurate values for Stress Intensity Factors (SIFs). The alternative approach is to use the hybrid DIC-Finite Element (DIC-FE) method to solve for the *J*-Integral at each load-step. This method accounts for plastic deformations present in the material but does not allow for extraction of SIFs. In this work, significant plasticity was observed in the material, and the crack groove geometry constrains the crack growth to a self-similar mode-I path. For these reasons, the DIC-FE method is needed in order to accurately extract the fracture parameter, and the mode-II effects during crack growth are negligible.

During implementation of the hybrid DIC-FE method, contour plots are generated from the recorded DIC displacement field data. These contours show isostatic fields of u_x and u_y components where the deformation levels remain constant for each contour. These contours can show that the loading of the specimen is symmetric and help visualize the nature of deformation before and after crack initiation during loading history. Fig. 5.9 shows two representative contour plots of a N1R specimen at a load of 9896 N. This load-step is just prior to crack initiation. In Fig. 5.9a, the u_x displacement component is shown. This is the displacement component field parallel to the direction of the crack. Close to the crack tip, the displacement is approximately zero, and near the edges of the specimen the displacement is positive as the specimen bends. In Fig. 5.9b, the u_y component field shows the displacement perpendicular to the direction of the crack. This contour

plot shows an anti-symmetric nature of deformation as the crack opens, and the compression of the specimen occurs on the edge opposite to the notch tip.

Using this DIC-FE method to extract results for different time steps with increasing load, we can characterize the material behavior throughout the loading sequence. These data are shown in Fig. 5.10 for the N1R condition. As the loading pin causes the specimen to deflect, the energy release rate (*J*-integral) increases parabolically. When *J* reaches the critical value, the crack initiates. This critical value—the final point shown in Fig. 5.10 at load of 9896 N—is related to the fracture toughness of the material.

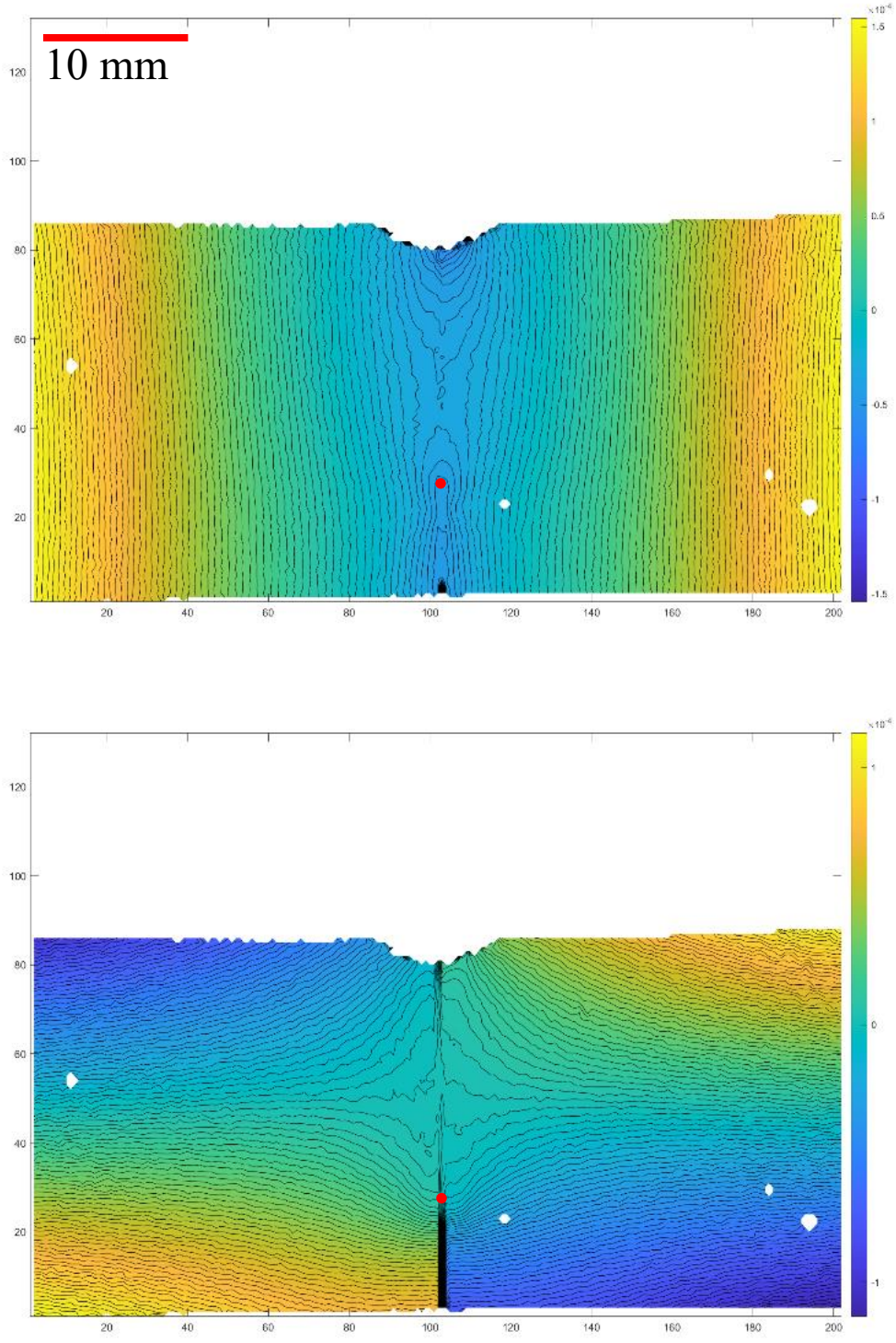

Figure 5.9: Contour plots of a) *x*-displacement field, b) *y*-displacement field. Contour increment is 0.003mm.

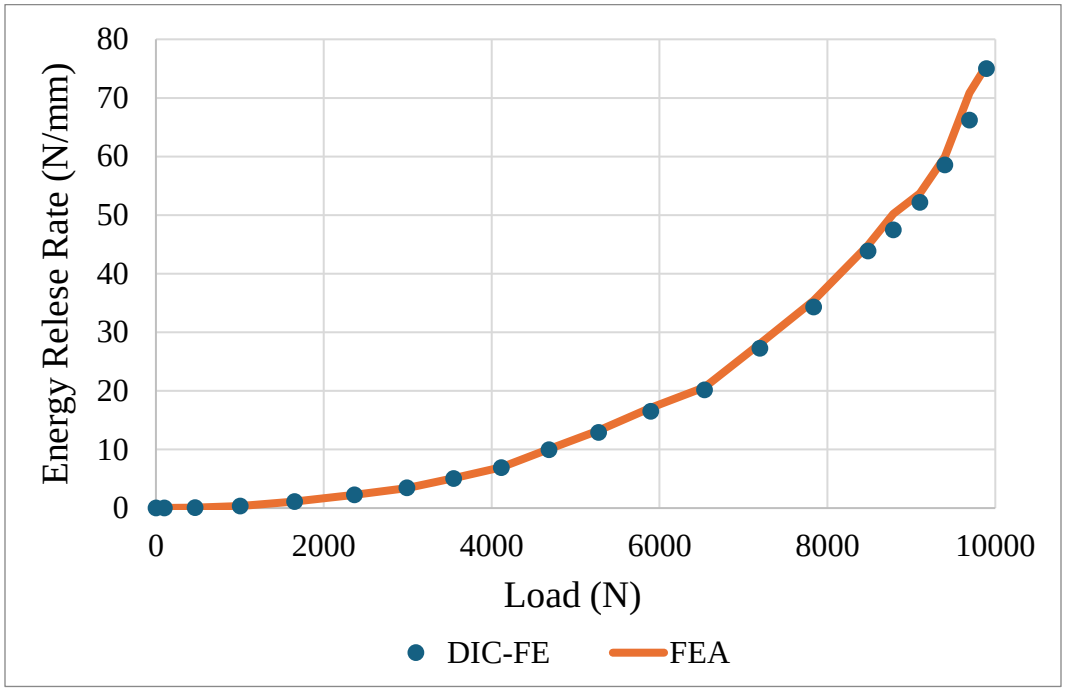

Figure 5.10: Validation of DIC-FE extracted data for N1R specimen

Here, the solid blue symbols points show the *J*-integral values extracted from DIC-FE, while the solid orange line is the one extracted from a standard FE analysis based on far-field load and load-point displacement measurements from the testing machine. This analysis was done to validate the extracted results, and is not based on the data collected using DIC. Because both the DIC-FE method and the standard FE analysis both are defined using the tensile stress-strain data for IN-718, they account for the elastic-plastic behavior present in the specimen.

In some quasi-static experiments, the crack initiation occurred abruptly and led to a rapid crack growth. In these cases, the post-initiation behavior could not be captured because the crack growth occurred too rapidly relative to the frame rate of the camera. However, in some cases the crack grew slowly, and the post-initiation data was collected. The post-initiation data analysis was similar to the stationary

crack case described earlier except the crack tip must be located in every frame. The resulting crack growth resistance (or, ERR vs. crack extension) data is shown for one such case for the A1K condition in Fig. 5.11. These data show the energy release rate continues to increase as the crack advances. This behavior indicates the ductility of the material responsible for increasing amounts of energy release rate needed to continue to cause the crack to grow. Similar post-initiation crack growth resistance behavior is seen for all manufacturing conditions where slow crack growth was observed, as shown in Appendix A.

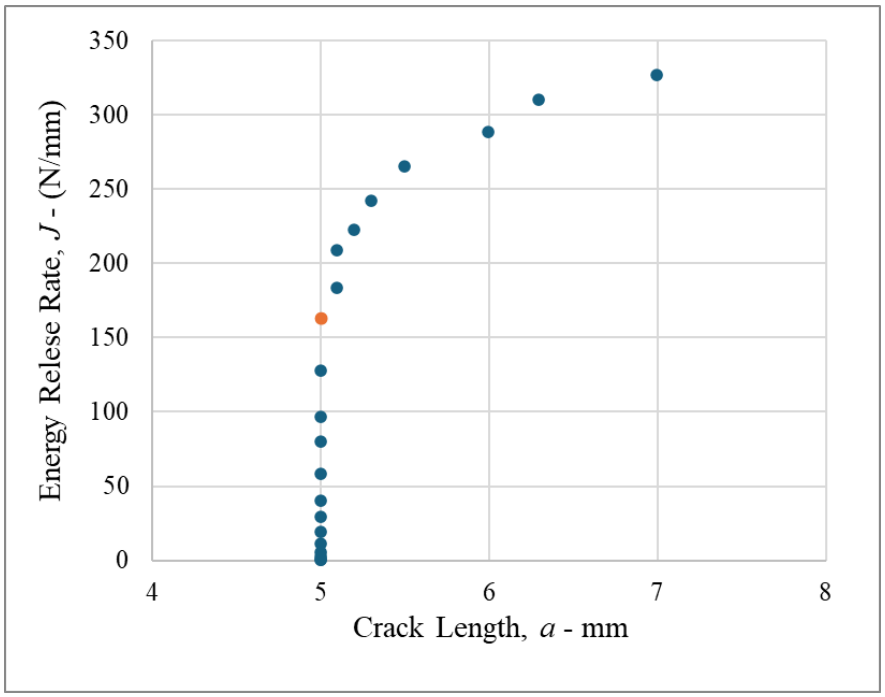

Figure 5.11: Crack growth resistance behavior of A1K specimen

Here, the energy release rate is plotted against crack length to show the post-initiation behavior as the crack grows. The *J*-integral values continue to increase after the critical value, highlighted in orange. This shows a ductile behavior where additional energy is needed to continue to grow the crack after initiation has occurred.

Repeating the DIC-FE extraction for all 12 manufacturing conditions, the critical value of the *J*-integral marking the point of crack initiation can be found for each. These data are shown in Table 5.1, as well as the validation point found from a companion FE analysis driven by the boundary condition of the loading pin displacement, rather than DIC data. Notably, the selected LPP, which controls the prevalence of keyhole and lack of fusion defects in the specimens, has relatively little effect on the critical energy release rate, but the heat treatment and shielding gas have significant effects. Comparing argon gas specimens to their nitrogen gas counterparts, it is observed that the argon gas specimens have a higher critical *J*-integral value in every case. Similarly, comparing the two heat treatments, HT1 specimens have a higher critical *J*-integral value than their HT2 counterpart for every case. This results in the Argon HT1 (A1) specimens having the highest critical energy release rate, regardless of LPP, and Nitrogen HT2 (N2) specimens having the lowest critical energy release rate value.

Table 5.1: Quasi-static results extracted using DIC-FE method for different manufacturing conditions.

			Critical *J*-integral (N/mm)	
Gas	**HT**	**LPP**	**DIC-FE**	**FEA**
Nitrogen	**1**	**L**	85.3	82.0
		R	73.3	76.9
		K	78.5	78.3
	2	**L**	48.1	52.1
		R	54.4	53.6
		K	47.0	49.7
Argon	**1**	**L**	132.8	109.8
		R	159.3	154.7
		K	163.1	131.3
	2	**L**	84.7	86.2
		R	69.8	68.4
		K	85.0	82.8

The difference between the critical energy release rates of A1 and N2 specimens is significant. The average value of *Jc* among the A1 specimens is 151.8 N/mm, while the average among N2 specimens is only 49.8 N/mm. To further understand how this difference arises, scanning electron microscopy is performed and the images are examined in section 5.3.1. Because the LPP has an insignificant effect on the critical energy release rate values for the quasi-statically loaded cases, different LPPs will not be used for the high strain-rate specimens. Instead, the recommended LPP will be used in all the high strain-rate experiments and only four manufacturing conditions (A1, A2, N1, N2) will be tested.

5.3.1 Fractography

To further understand why the difference in the critical value of the *J*-integral is so large between the different heat treatments and shielding gases, the fracture surface of each specimen was examined under a scanning electron microscope. In Fig. 5.12, images of the fracture surface are shown for two manufacturing conditions varying the heat treatment and shielding gas, but with the recommended LPP. The magnification is 10,000X and the electron high tension (EHT) is 5.00 kV.

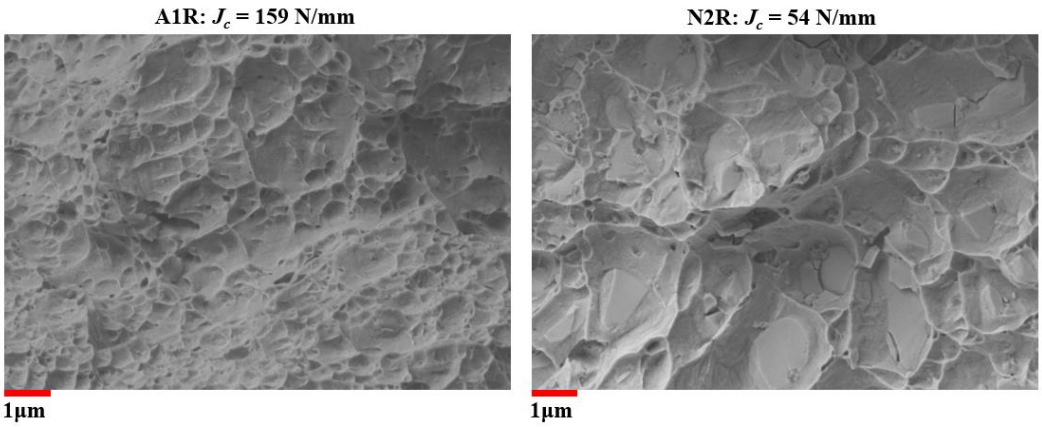

Figure 5.12: SEM imagery of A1R and N2R quasi-static fracture surfaces at 10,000X magnification

In these images the cup and cone structures formed during the crack growth are visible. In the A1 manufacturing condition, the cup and cone formations are densely packed together. There are a large number of ridges on the fracture surface formed as the material failed. In the N2 condition, the cup and cone structures are sparser or more spread out. The ridges are larger but are not as densely packed. This indicates that the expected energy required to create new surface area in the A1 condition should be greater than for the N2 condition. This microscopic evaluation aligns with the macroscopic results seen in Section 5.3.

The A2 and N1 conditions have roughly similar values of critical value of *J*-integral, in between the maximum and minimum seen in the A1 and N2 conditions, respectively. These fracture surfaces also appear as an intermediate between the extremes when looking for ridges and cup and cone structures. No significant difference can be observed in the fracture surfaces for these two conditions.

5.4 High Strain-Rate Results

The high strain-rate specimens were tested using a compression split-Hopkinson pressure bar apparatus described in section 4.3. Based on the quasi-static results, the LPP has very little effect on the fracture properties, and so for the high strain-rate experiments the recommended LPP is used for all specimens while the shielding gas and heat treatment are varied. This gives four total manufacturing conditions to be tested, which are referred to here as simply A1, A2, N1, and N2. After experimentation, the captured speckle images were analyzed using DIC. The contour plots in Fig. 5.13 show the measured planar deformations on the surface from the A1 specimen as a representative case. Additional contour plots are shown in Appendix B.

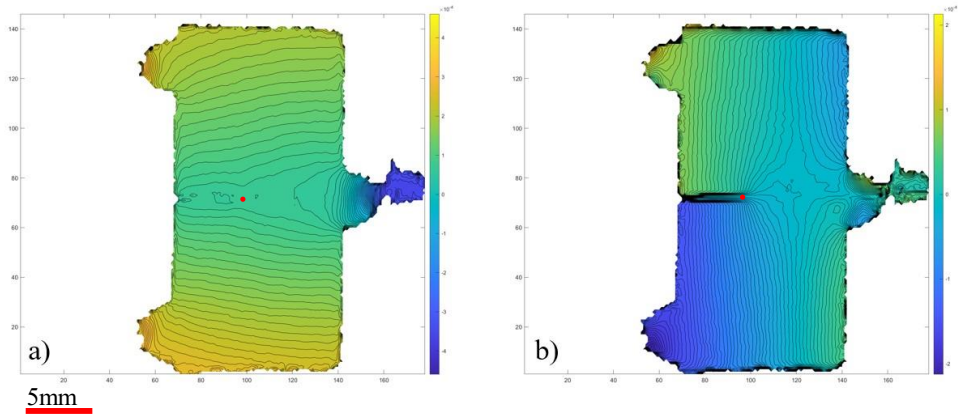

Figure 5.13: Contour plots of the high strain-rate A1 specimen at the point of crack initiation. a) u_x displacement field with contour increment of 0.009 mm. b) u_y displacement field with contour increment of 0.005 mm.

From this DIC measurement, the DIC-FE method is used to extract the energy release rate for each load and time-step up to the point of crack initiation and beyond. Because of the nature of the high-strain rate experiments, a load-cell cannot be used to measure load. Since load data is not available in these tests, the

J-integral history is shown. The trend shows how the energy release rate increases as the stress wave travels through the specimen. There is a decrease in the value of the *J*-integral prior to crack initiation. This indicates some irregular loading from the split-Hopkinson pressure bar and can be seen by observing the motion of the specimen in the video animation of the images recorded by the camera. The irregular loading pattern is discussed in more detail later in this section. In Fig. 5.14, the energy release rate history is plotted, with the critical value at crack initiation highlighted in orange

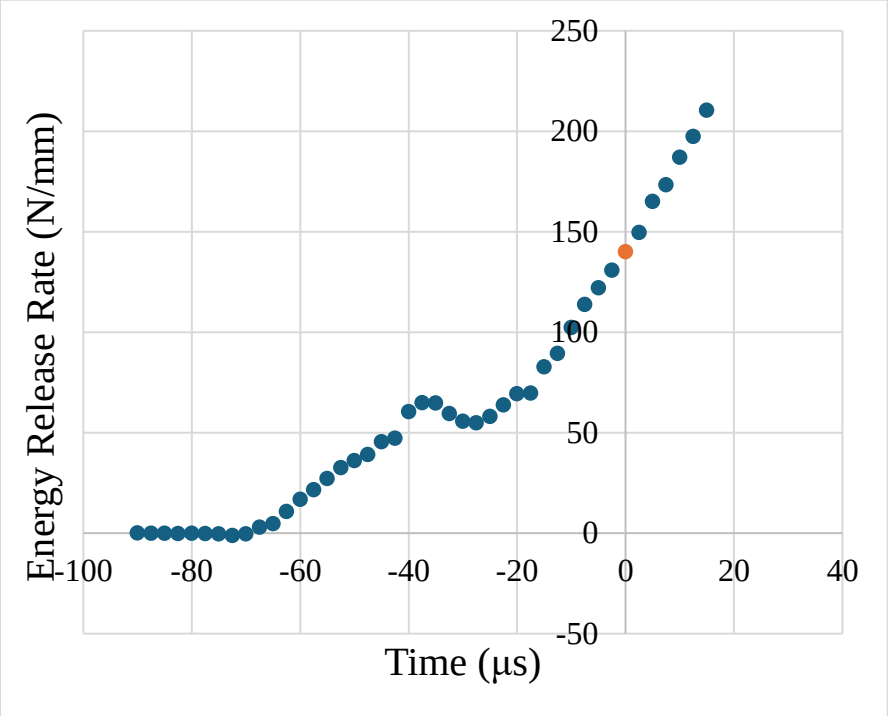

Figure 5.14: Plot of *J*-integral history for A1 specimen from high strain-rate experiment

Once the crack initiates, the energy release rate continues to increase beyond crack initiation. For all specimens, the post-initiation behavior can be analyzed. The first aspect of the post-initiation behavior to analyze for the dynamic experiments is the

crack velocity. The crack velocity is determined by the crack tip locations selected by identifying the point of convergence of contours in the contour plots, as seen in Fig. 5.13. For all specimens, the maximum crack velocity is less than 50 m/s. This is substantially lower than the longitudinal wave speed in the material, which is measured to be ~6100 m/s using an ultrasonic transducer in pulse-echo mode. Maximum crack velocities measured for each manufacturing condition are displayed in Table 5.2. All crack velocities are sufficiently slow to assume quasi-static crack growth in these dynamic experiments and extract meaningful crack growth resistance behavior as *J* vs. crack extension graphs.

Table 5.2: Maximum crack velocity for each manufacturing condition.

Manufacturing Condition	Max. Crack Velocity (m/s)
A1	15.6
A2	46.6
N1	29.9
N2	37.3

A continuous increase in energy release rate is seen after crack initiation. The A1 specimen data is displayed as a representative case as shown in Fig. 5.15. Like in the quasi-static experiments, this continuous increase in the *J*-integral as a result of material ductility, requiring more energy for the crack to continue to grow after initiation. However, this increase is much more significant than what is seen in the quasi-static experiments, suggesting that under dynamic conditions, the loading rate effects of the material are significant. This also shows that the high-strain-rate specimens are failing in a ductile fashion, in contrast to some of the

quasi-static specimens which failed abruptly. The crack resistance behavior is shown in Fig. 5.15. The critical value is highlighted by an orange symbol.

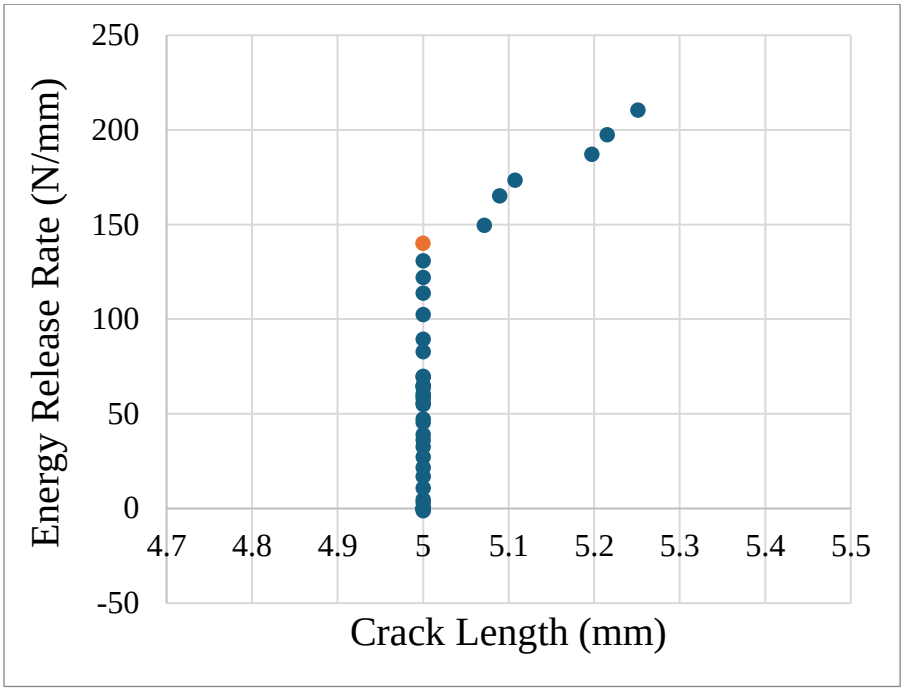

Figure 5.15: Crack growth resistance for high strain-rate A1 specimen.

To evaluate the energy release rate, the DIC-FE method was used. The stress-strain response used in the FE analysis is the same tensile test data used in the quasi-static calculations. It is assumed that the change from quasi-static to high strain-rate condition has negligible effect on the elastic properties. The material behavior at increasing time steps is characterized up to and beyond the point of crack initiation. After repeating this for the four selected manufacturing conditions, the critical value of the *J*-integral at crack initiation is reported in Table 5.3. These values have approximately 5-15% difference with their quasi-static counterparts.

Table 5.3: J_{cr} for high strain-rate specimens

Gas	HT	Critical Energy Release Rate (N/mm)
	1	140.1

Ar	**2**	81.7
N_2	**1**	78.3
	2	50.2

Much like the quasi-static results, the A1 specimen has the highest critical value whereas the N2 condition has the lowest. There is a significant effect of heat treatment and shielding gas on the critical value of energy release rate. Unlike in the quasi-static experiments, the load is not monotonically increasing here. Instead, as the stress wave loading occurs, the specimen seems to have been loaded non-monotonically. The initial energy from the impact of the incident bar begins to bend the specimen and cause the notch to open. As the energy grows and the *J*-values increase, it reaches a threshold where the loading pin begins to deform drastically when compared to the region near the notch tip. This loading pin deformation results in a period where the specimen deforms very little in the region of interest close to the tip, causing the value of *J*-integral to plateau. After this small period of irregularity, the loading continues to become more established, open the crack and eventually causes crack to initiate. Because the crack initiation occurs well after this period of irregular loading, the critical value of *J*-integral is expected to be unaffected.

When examining the non-monotonic loading, friction effects were considered as a possible cause. If significant friction existed between the support pins and the face of the transmitted bar of SHPB, it could prevent the crack from opening. To test this speculation, experiments were conducted again using specimens of the N2 manufacturing condition with a lithium grease lubricant applied to the surface between the specimen and the transmitted bar. This reduced

any friction present on this surface, but little change was seen in the energy release rate history, indicating that the primary cause is more likely due to the deformation of the loading pin discussed earlier. These data are displayed in Fig. 5.16, with the highlighted orange colored data point representing the point of crack initiation. Also, it is worth noting that the greased test was performed on a N2 specimen and not the A1 specimen discussed previously.

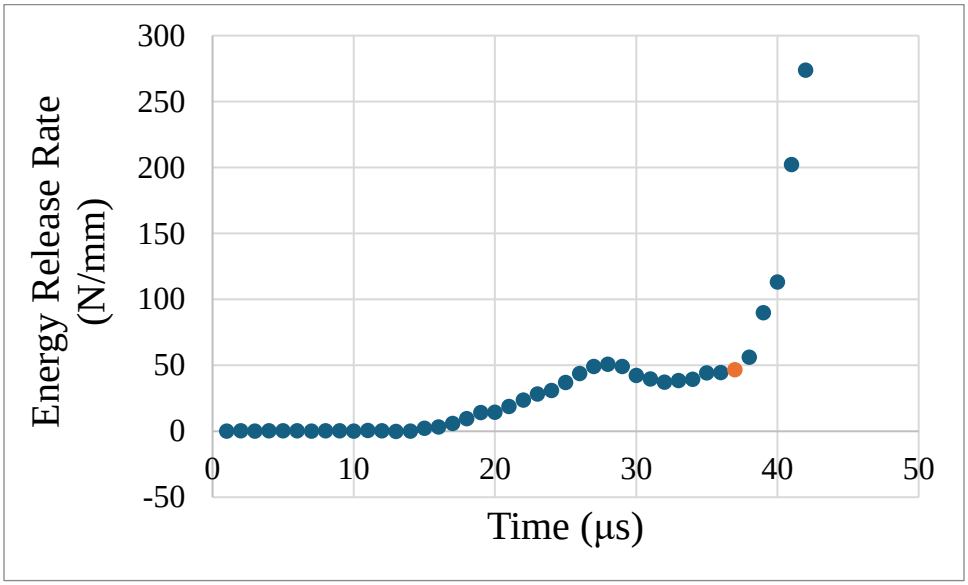

Figure 5.16: *J*-integral history for N2 specimen with lithium grease lubricant applied.

There is some reduction in the loading irregularity, but it is not significant. Previously, the difference in the local maximum to the subsequent local minimum was approximately 11 N/mm. After introducing the lubricating grease, the difference is approximately 10 N/mm. This shows that this irregularity is not primarily due to the friction between the support pins and the transmitted bar of SHPB.

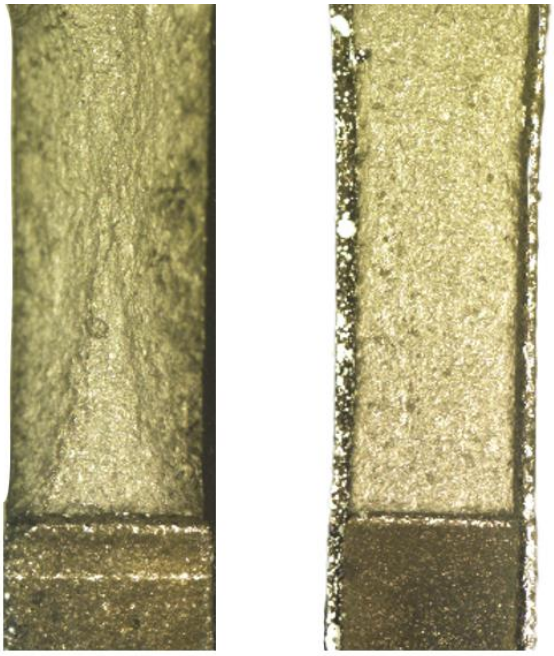

Figure 5.17: Fracture surface comparison of non-grooved and grooved specimens

To evaluate the possibility of persistent crack tunneling, the fracture surface is examined. Observing the fracture surface of the specimen without the side grooves, clear evidence shear lip formation exists. Additionally, a flat triangular region between the shear lips indicates the location of the crack groove. In the grooved specimen, the fracture surface has no visible shear lips. The entire fractured surface is relatively flat indicating that the crack front is not tunneling and curving. Due to the nature of the high strain-rate experiments, it is difficult to halt the experiment in the middle to examine the crack with XCT scans, as was done for quasi-static specimens described in section 3.1. It is also not possible in the current setup to measure the crack in-situ to monitor for crack tunneling. However, all posthumous evaluation indicates that the side-groove have successfully removed crack tunneling and that the loading irregularity has a different explanation.

Examining the images of the specimen gives further evidence that the irregular loading is due to the nature of loading pin deformation. Fig. 5.18 shows a before and after image of the N1 specimen during loading. Fig. 5.18a is immediately prior to the initial impact, while Fig. 5.18b is after some load has been applied which opened the crack slightly and has visibly deformed the loading pin.

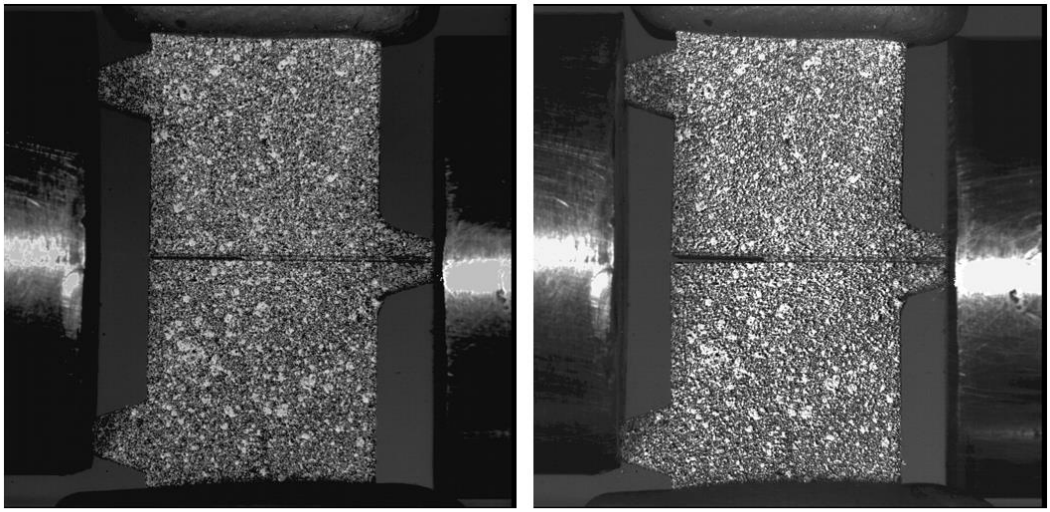

a) b)

Figure 5.18: N1 specimen a) before loading and b) after the stress wave has reached the specimen and load is applied.

The deformation in the loading pin requires energy. Therefore, much of the energy that is going into the specimen is being used to deform the loading pin rather than the cracked specimen. Using DIC, we can measure the average strain in the loading pin. Average strain is found by averaging the strain in a 5×5 square of DIC sub-images in the center of the loading pin.

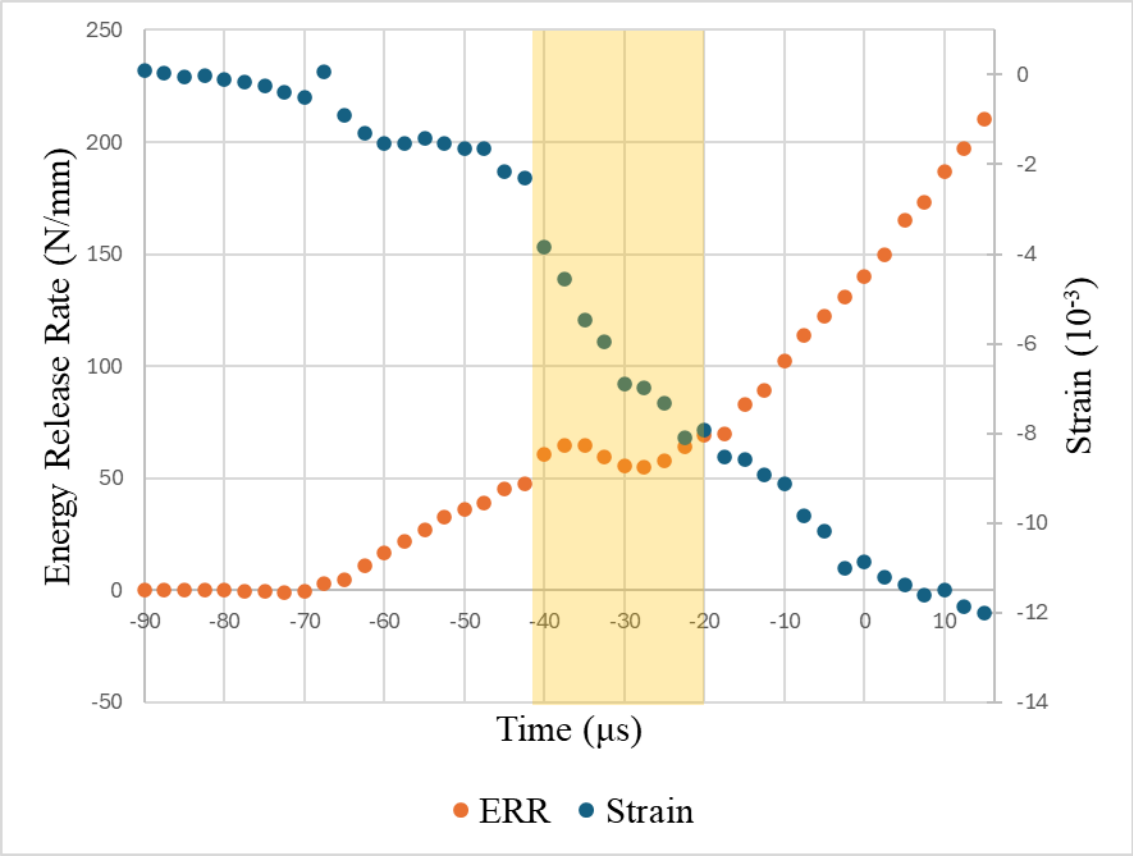

Figure 5.19: Correlation between measured energy release rate and strain in the loading pin from DIC.

The extracted energy release rate in Fig. 5.19 is shown in orange and is labeled by the vertical axis on the left side. The measured strain in the loading pin is shown in blue and is labeled by the secondary vertical axis on the right side. Note also that the strain is negative to indicate compression. The highlighted region from -40µs to -20µs is the time where the irregular loading is occurring. During this period, there is a clear increase in the strain-rate in the loading pin in comparison to the strain-rate of the loading pin prior to t = -40µs. This correlation gives evidence that one cause for non-monotonically increasing values of the J-integral could be the compression of the loading pin. Future work may look for alternative specimen

geometries to remove this irregularity since monotonic loading is desirable. Other potential explanations could be due to inherent backlash or lag in the loading apparatus. However, it is not expected that irregular loading prior to the critical value should have an impact on the energy release rate at crack initiation.

Chapter 6: Conclusions

The primary motivation of this work has been the study of the effects of shielding gas, heat treatment, and laser process parameters on the fracture behavior of additively manufactured IN-718 using the full-field optical method of digital image correlation (DIC). Secondarily, It has been demonstrated here that a combined fields approach can accurately extract crack tip stress intensity factors (SIFs) under mode-I, mode-II, and mixed-mode conditions more precisely from measured displacements from 2D DIC. This method has improved precision and robustness in comparison to the single-field legacy approach. The combined fields method is resilient to changes in user-determined parameters, namely the number of terms, region of interest, and selected crack tip location for full-field displacement analysis from DIC measurements. The combined fields method results in greater than 70% reduction in the standard deviation in the extracted values after altering these parameters, demonstrating the method is substantially more robust than the legacy method.

While this method is highly effective for linear elastic experiments, it was observed that IN-718 specimens exhibited severe elastoplastic deformations near the crack tip during fracture events. As a result, the combined fields method fell short as it is rooted in linear elastic fracture mechanics. This led to the adoption of a hybrid DIC-FE method instead to recover alternative fracture parameter namely the energy release rate evaluated as the *J*-integral, rather than SIFs, as the primary parameter of interest. It has been shown that under quasi-static loading conditions the laser process parameters which induce defects do not have significant effect on

critical energy release rate at crack initiation. Rather, it is seen that heat treatment and shielding gas have dominant effect. For both quasi-static and high strain-rate loading, it is shown that the Argon shielding gas results in a tougher material than the Nitrogen shielding gas. Additionally, heat treatment 1 protocol yields tougher specimens than heat treatment 2 protocol. Additionally, the critical values extracted for many of the LPBF specimens in this work is higher than what is reported in the literature for wrought and cast specimens [23].

The superior manufacturing condition under quasi-static loading was the A1K condition with a critical energy release rate of 163.1 N/mm. The A1R and A1L conditions also were stronger than any alternative heat treatment or shielding gas. The N2K manufacturing condition had the lowest critical energy release rate of 47.0 N/mm, and the N2R and N2L conditions were similarly weaker than any alternative heat treatment or shielding gas. The crack growth resistance behavior for select quasi-static experiments which allowed for post-initiation behavior to be extracted showed the influence of material ductility of IN-718. The crack growth resistance curves in these cases were continuously increasing throughout the crack growth window during experiments.

Under high strain-rate loading, as was tested using the split-Hopkinson pressure bar apparatus, the same trend with shielding gas and heat treatment holds. There is only slight difference between the critical energy release rate under quasi-static and dynamic conditions. The Argon shielded specimens are tougher than the Nitrogen gas shielded specimens, and heat treatment 1 protocol resulted in tougher specimens than heat treatment 2 protocol. The A1 condition yielded a critical

energy release rate of 140.1 N/mm, the strongest condition under high strain-rate loading. The next strongest was the A2 conditions with a critical value of 81.7 N/mm. The third strongest condition was N1, with a critical value of 78.3 N/mm. The weakest condition was the N2 condition with the critical energy release rate value found to be 50.2 N/mm. Similar to the quasi-static case, the post-fracture crack growth resistance behavior of the dynamic experiments does not differ substantially. The crack velocity under dynamic loading conditions were very low (<50 m/s) relative to the stress wave speeds due to expansive plasticity. As a result, crack growth resistance curves for high strain-rate loading conditions were plotted as energy release rate vs. crack extension instead of crack velocity. They showed a constantly increasing pattern as in the quasi-static cases.

Based on these results, this research has concluded that heat treatment and shielding gas have a substantial effect on the fracture behavior of additively manufactured IN-718 under quasi-static and dynamic loading conditions, as was originally hypothesized. However, contrary to the initial hypothesis, it was found that no significant difference was seen in the fracture behavior by inducing defects into the material through the altered laser process parameters. Therefore, it is concluded that the heat treatment and shielding gas used during the additive manufacturing process of IN-718 is more important to fracture behavior than laser process parameter and defects introduced into the part.

6.1 Future Work

This thesis explores in depth the fracture behavior of additively manufactured IN-718 in quasi-static and high strain-rate loading configurations.

However, this work is limited in scope by the time, equipment and resources available. Future researchers interested in this material system can continue to study the fracture behavior and make new discoveries which cannot be covered by this work.

One area of interest is concerning the crack tunneling behavior. This work sought to eliminate the tunneling behavior as much as possible and so the nature of the tunneling was not studied. Now that this behavior is known and documented, future work could devise an experiment to measure the crack tunnell in-situ and learn the precise nature of how the tunnell forms and the energy release rate of tunneling cracks. Experimentalists may seek to use stereo-DIC to measure out of plane deformations and identify a way to locate the internal crack tip. Alternative experiment methods using XCT scans may be adapted to allow for in-situ measurement of crack tunneling.

Another area of future work concerning IN-718 is it's behavior at elevated temperatures. Because many applications of Inconel involve high temperature environments, additional work should be done to determine fracture behavior at several elevated temperatures. Prior literature on Inconel has been done to test it's fatigure behavior at elevated temperatures, and expanding this to fracture would be an appreciated contribution to the current literature.

Alternative material and manufacturing conditions could be considered by future researchers. Various chemical compositions could be explored in more detail. Additional heat treatments, atomization techniques, and laser parameters should be tested as well. In this work, it was seen that laser parameter had minimal

impact on the fracutre toughness. Altering the LPPs to induce a greater number of defects or defects of larger size could result in a different conclusion. Lastly, additional variables which have been controlled in this work could be studied, such as build orientation, and alternative methods of printing.

References

1. Kassner ME, Son KT, Lee KA, Kang TH, Ermagan R. The creep and fracture behavior of additively manufactured Inconel 625 and 718. Materials at High Temperatures. 2022 Nov 2;39(6):499-506.
2. Vieille B, Keller C, Mokhtari M, Briatta H, Breteau T, Nguejio J, Barbe F, Azzouna MB, Baustert E. Investigations on the fracture behavior of Inconel 718 superalloys obtained from cast and additive manufacturing processes. Materials Science and Engineering: A. 2020 Jul 14;790:139666.
3. Dodaran MS, Muhammad M, Shamsaei N, Shao S. Synergistic effect of microstructure and defects on the initiation of fatigue cracks in additively manufactured Inconel 718. International Journal of Fatigue. 2022 Sep 1;162:107002.
4. Lu Y, Wu S, Gan Y, Huang T, Yang C, Junjie L, Lin J. Study on the microstructure, mechanical property and residual stress of SLM Inconel-718 alloy manufactured by differing island scanning strategy. Optics & Laser Technology. 2015 Dec 1;75:197-206.
5. Soong SZ, Lai WL, Kay Lup AN. Atomization of metal and alloy powders: Processes, parameters, and properties. AIChE Journal. 2023 Nov;69(11):e18217.
6. Yu X, Lin X, Liu F, Wang L, Tang Y, Li J, Zhang S, Huang W. Influence of post-heat-treatment on the microstructure and fracture toughness properties of Inconel 718 fabricated with laser directed energy deposition additive manufacturing. Materials Science and Engineering: A. 2020 Nov 4;798:140092.
7. Li Y, Zhou M. Effect of competing mechanisms on fracture toughness of metals with ductile grain structures. Engineering Fracture Mechanics. 2019 Jan 1;205:14-27.
8. Park SY, Kim KS, Kim MC, Kassner ME, Lee KA. Effect of post-heat treatment on the tensile and cryogenic impact toughness properties of inconel 718 manufactured by selective laser melting. Advanced Engineering Materials. 2021 Mar;23(3):2001005.
9. Zhao JR, Hung FY, Lui TS. Microstructure and tensile fracture behavior of three-stage heat treated inconel 718 alloy produced via laser powder bed fusion process. Journal of Materials Research and Technology. 2020 May 1;9(3):3357-67.
10. Sutton MA, Orteu JJ, Schreier H. Image correlation for shape, motion and deformation measurements: basic concepts, theory and applications. Springer Science & Business Media; 2009.
11. Pan B. Digital image correlation for surface deformation measurement: Historical developments, recent advances and future goals. Measurement Science and Technology. 2018; 29(8):082001

12. Becker TH. Extracting fracture properties from digital image and volume correlation displacement data: A review. Strain. 2024; 60(4):e12469.
13. Eshraghi I, Dehnavi MR, Soltani N. Effect of subset parameters selection on the estimation of mode-I stress intensity factor in a cracked PMMA specimen using digital image correlation. Polymer testing. 2014; 37:193-200.
14. Mokhtarishirazabad M, Lopez-Crespo P, Moreno B, Lopez-Moreno A, Zanganeh M. Evaluation of crack-tip fields from DIC data: A parametric study. International Journal of Fatigue. 2016; 89:11-9.
15. Yates JR, Zanganeh M, Tai YH. Quantifying crack tip displacement fields with DIC. Engineering Fracture Mechanics. 2010; 77(11):2063-76.
16. McNeill SR, Peters WH, Sutton MA. Estimation of stress intensity factor by digital image correlation. Engineering fracture mechanics. 1987; 28(1):101-12.
17. Beretta S, Patriarca L, Rabbolini S (2017) Stress Intensity Factor calculation from displacement fields. Frattura e Integrita Strutturale 11(41):269–276
18. Yoneyama S, Ogawa T, Kobayashi Y. Evaluating mixed-mode stress intensity factors from full-field displacement fields obtained by optical methods. Engineering fracture mechanics. 2007; 74(9):1399-412.
19. Reddy MS, Ramesh K, Thiyagarajan A. Evaluation of mode-I SIF, T-stress and J-integral using displacement data from digital image correlation–Revisited. Theoretical and Applied Fracture Mechanics. 2018; 96:146-59.
20. Owens AT, Tippur HV. Measurement of mixed-mode fracture characteristics of an epoxy-based adhesive using a hybrid digital image correlation (DIC) and finite elements (FE) approach. Optics and Lasers in Engineering. 2021 May 1;140:106544.
21. Cook TS. Stress-strain behavior of Inconel 718 during low cycle fatigue. July 1982
22. Matthews JR, West GD. J Ic Measurement Point Determination for HY130, CMS-9, and Inconel Alloy 718. Journal of testing and evaluation. 1983 May 1;11(3):217-24.
23. Bouse GK. Impact and fracture toughness of investment cast, plasma sprayed, and wrought alloy 718. Superalloys. 1991;718:625.
24. Kawagoishi, Chen, Nisitani. Fatigue strength of Inconel 718 at elevated temperatures. Fatigue & Fracture of Engineering Materials & Structures. 2000 Mar;23(3):209-16.
25. Hohnbaum CC. Fracture toughness and fatigue crack growth rate characterization of Inconel 718 formed by laser powder bed fusion. 2019
26. Anderson TL, Anderson TL. Fracture mechanics: fundamentals and applications. CRC press; 2005 Jun 24.
27. Nalawade C, Saxena S, Mohanty A. Evaluating the effect of side grooving parameters on critical SZW. Engineering Fracture Mechanics. 2016 Mar 1;153:1-0.

28. Edwards A, Cho J, Tippur H. Extracting Mixed-Mode Fracture Parameters Using Two Vision-based Methods: Comparison of Combined Fields Method with Legacy Approach. Experimental Mechanics. 2025 Mar 14:1-24.
29. Chong KP, Kuruppu MD. New specimen for fracture toughness determination for rock and other materials. International Journal of Fracture. 1984; 26(2):R59-62.
30. Ayatollahi MR, Aliha MR, Hassani MM. Mixed mode brittle fracture in PMMA - An experimental study using SCB specimens. Materials Science and Engineering: A. 2006; 417(1-2):348-56.
31. Fahem A, Kidane A, Sutton M. Loading Rate Effects for Flaws Undergoing Mixed-Mode I/III Fracture. Experimental Mechanics. 2021 61(8):1291-307.
32. Owens AT, Tippur HV. An image processing technique to identify crack tip position and automate fracture parameter extraction using DIC: application to dynamic fracture. Experimental Mechanics. 2023; 63(3):445-66.
33. Xie Y, Cao P, Jin J, Wang M. Mixed mode fracture analysis of semi-circular bend (SCB) specimen: A numerical study based on extended finite element method. Computers and Geotechnics. 2017; 82:157-72.
34. Kirugulige MS, Tippur HV. Measurement of fracture parameters for a mixed-mode crack driven by stress waves using image correlation technique and high-speed digital photography. Strain. 2009; 45(2):108-22.
35. Tippur HV, Krishnaswamy S, Rosakis AJ. A coherent gradient sensor for crack tip deformation measurements: analysis and experimental results. International journal of fracture. 1991; 48:193-204.
36. Soltani-Tehrani A, Isaac JP, Tippur HV, Silva DF, Shao S, Shamsaei N. Ti-6Al-4V powder reuse in laser powder bed fusion (L-PBF): The effect on porosity, microstructure, and mechanical behavior. International Journal of Fatigue. 2023 Feb 1;167:107343.
37. "Standard Specification for Additive Manufacturing Nickel Alloy (UNS N07718) with Powder Bed Fusion," ASTM F3055-14a, ASTM International, 2021
38. "Standard Guide for Determination of Various Elements by Direct Current Plasma Atomic Emission Spectrometry," ASTM E1097-12, ASTM International, 2017
39. "Standard Test Methods for Determination of Carbon, Sulfur, Nitrogen, and Oxygen in Steel, Iron, Nickel, and Cobalt Alloys by Combustion and Inert Gas Fusion Techniques," ASTM E1019-24, ASTM International, 2024
40. "Heat Treatment, Nickel Alloy and Cobalt Alloy Parts," AMS2774H, SAE International, 2024
41. Shih CF, Moran B, Nakamura T. Energy release rate along a three-dimensional crack front in a thermally stressed body. International Journal of fracture. 1986 Feb

Appendix A: Additional Quasi-Static Contour Plots

Appendix A contains contour plots showing the u_x and u_y displacement fields recorded using DIC in the quasi-static experiments. Horizontal and vertical displacement fields are shown for each manufacturing condition for one stage prior to crack initiation and one stage at the point of crack initiation. For the cases where post initiation data could be collected, one stage after crack initiation is included as well. Table A.1 includes the load and contour increment information for all figures.

Table A.1: Quasi-static contour plot details

Figure	Man. Condition	Load (N)	Contour Increment (u_x)	Contour Increment (u_y)
A.1	A1R	5183	0.003	0.003
A.2	A1R	13058	0.004	0.005
A.3	A1R	12909	0.005	0.006
A.4	A1L	4917	0.005	0.004
A.5	A1L	12760	0.007	0.004
A.6	A1L	12512	0.008	0.006
A.7	A1K	5670	0.003	0.003
A.8	A1K	13301	0.004	0.004
A.9	A1K	13953	0.005	0.006
A.10	A2R	4533	0.006	0.004
A.11	A2R	10924	0.012	0.006
A.12	A2L	5615	0.008	0.003
A.13	A2L	11543	0.008	0.004
A.14	A2K	4633	0.005	0.003
A.15	A2K	11632	0.006	0.005
A.16	N1R	4985	0.003	0.003
A.17	N1R	9896	0.003	0.003
A.18	N1L	4873	0.004	0.003
A.19	N1L	9783	0.004	0.003
A.20	N1L	9992	0.004	0.004
A.21	N1K	5641	0.003	0.003
A.22	N1K	10596	0.005	0.003
A.23	N2R	4691	0.003	0.003
A.24	N2R	8254	0.003	0.003
A.25	N2L	4812	0.003	0.003
A.26	N2L	7878	0.003	0.003
A.27	N2K	4911	0.003	0.003
A.28	N2K	7737	0.003	0.003

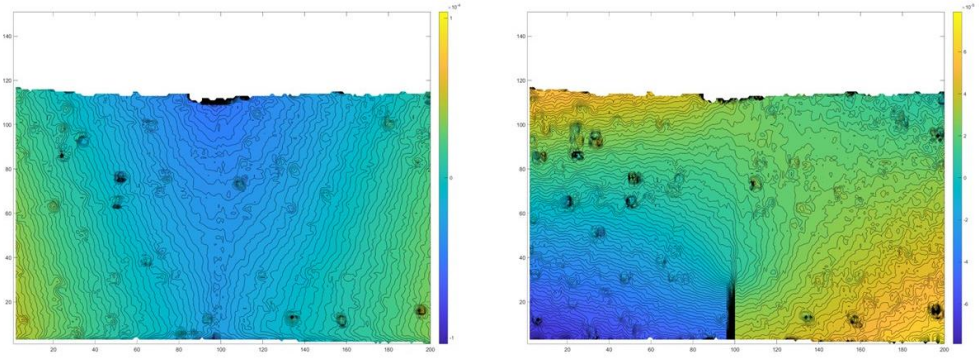

Figure A.1: A1R specimen prior to crack initiation: a) u_x displacement b) u_y displacement

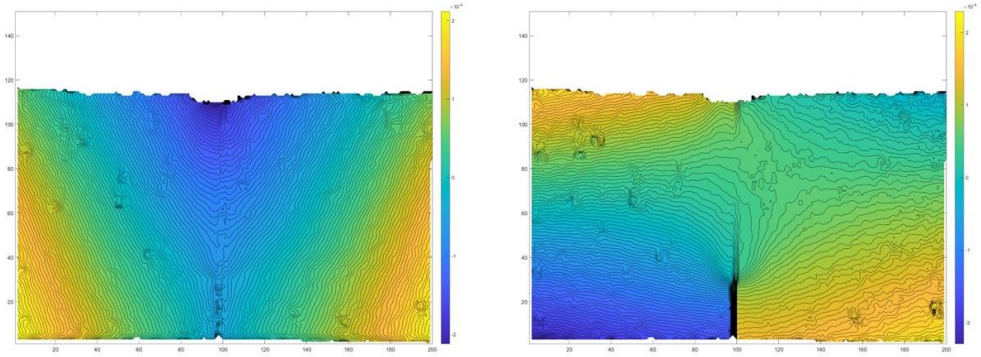

Figure A.2: A1R specimen at crack initiation: a) u_x displacement b) u_y displacement

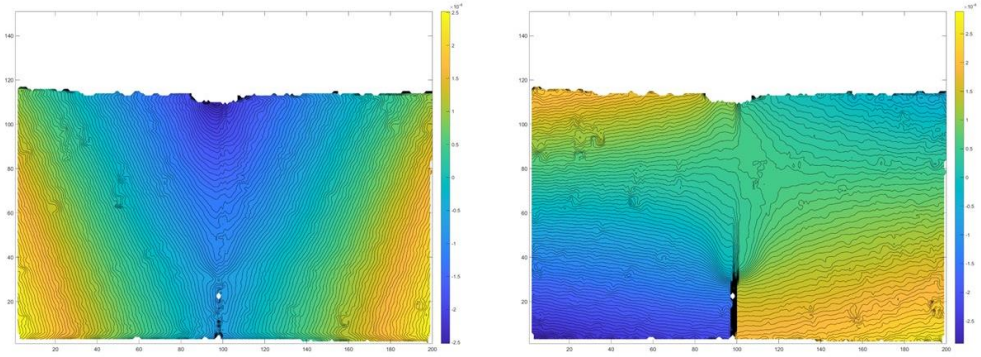

Figure A.3: A1R specimen after crack initiation: a) u_x displacement b) u_y displacement

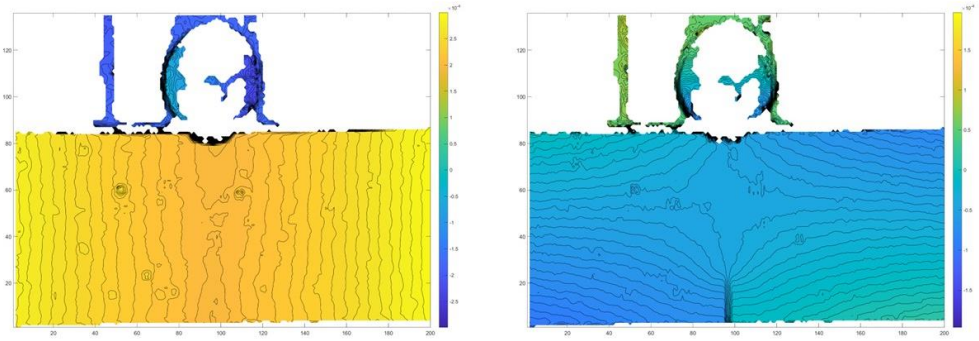

Figure A.4: A1L specimen prior to crack initiation: a) u_x displacement b) u_y displacement

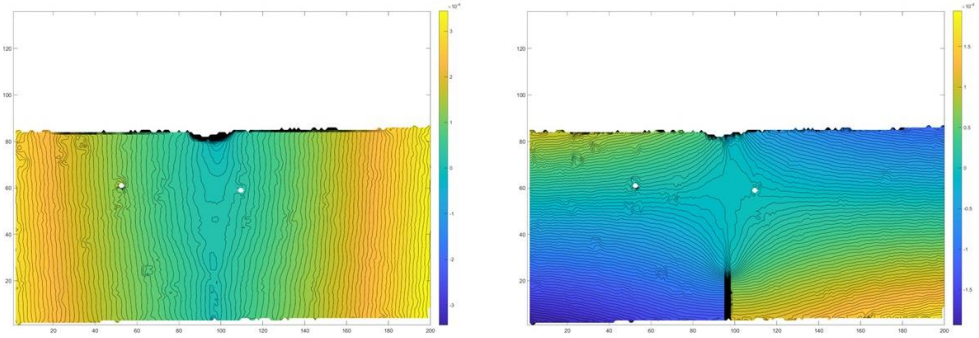

Figure A.5: A1L specimen at crack initiation: a) u_x displacement b) u_y displacement

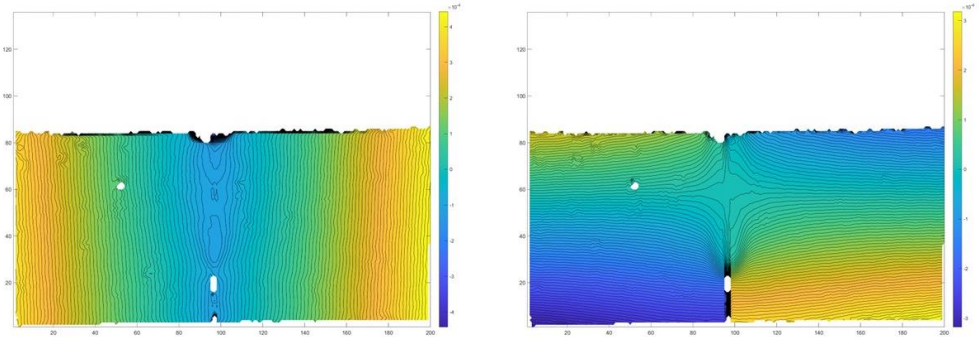

Figure A.6: A1L specimen after crack initiation: a) u_x displacement b) u_y displacement

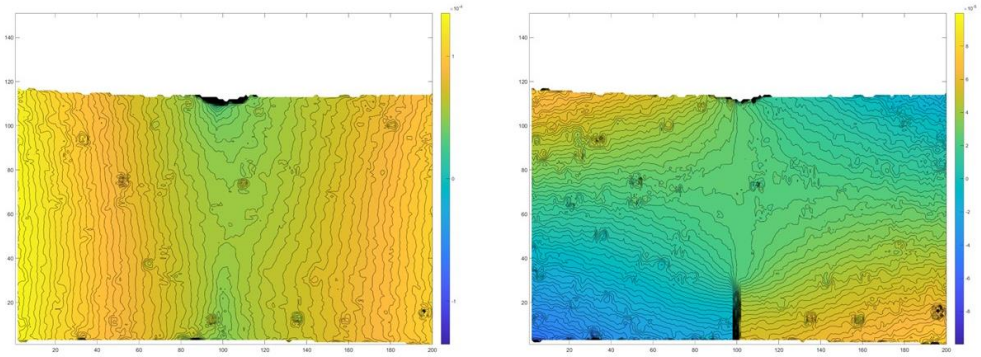

Figure A.7: A1K specimen prior to crack initiation: a) u_x displacement b) u_y displacement

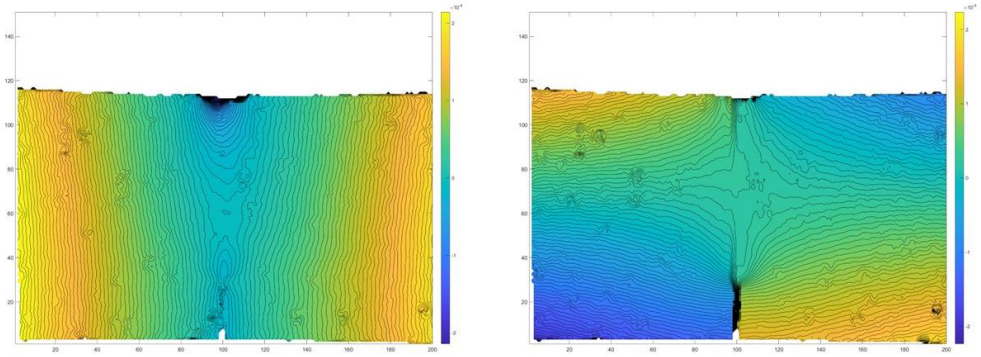

Figure A.8: A1K specimen at crack initiation: a) u_x displacement b) u_y displacement

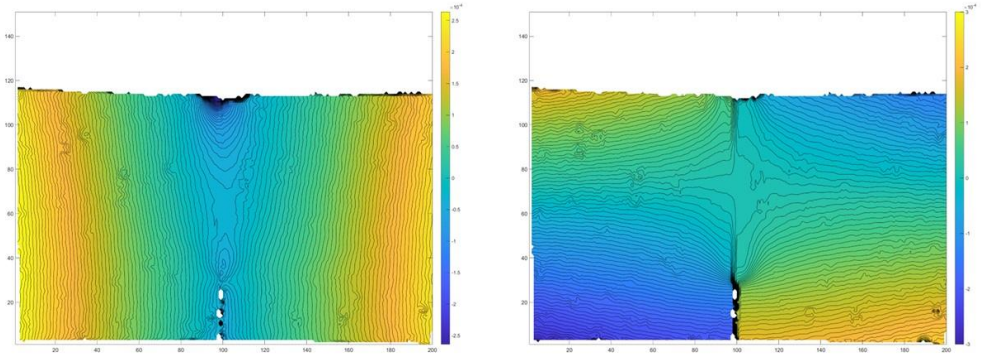

Figure A.9: A1K specimen after crack initiation: a) u_x displacement b) u_y displacement

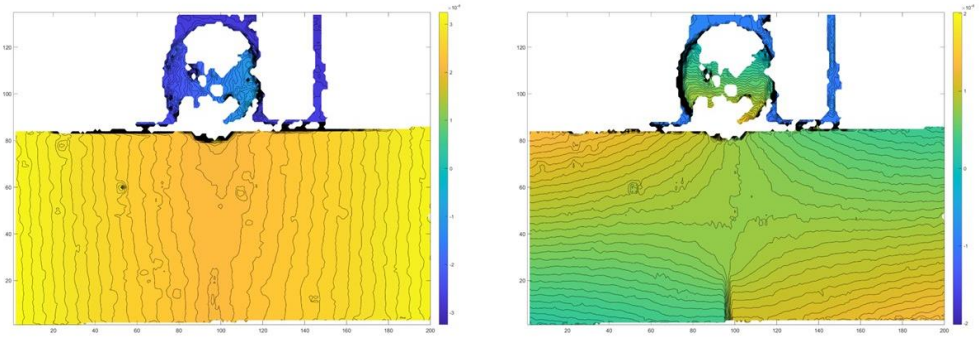

Figure A.10: A2R specimen prior to crack initiation: a) u_x displacement b) u_y displacement

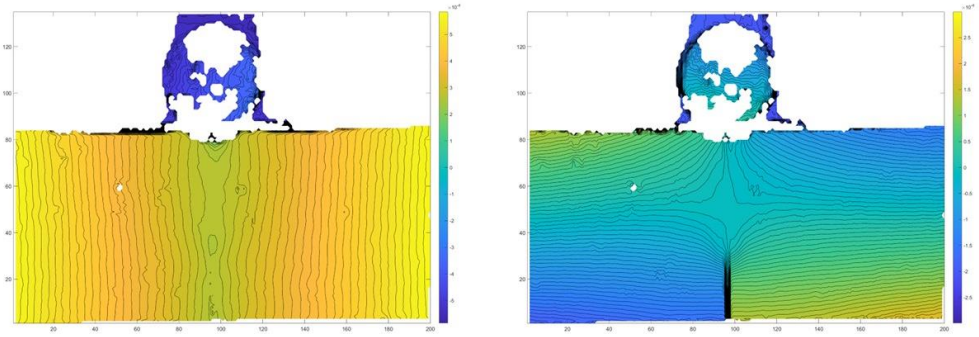

Figure A.11: A2R specimen at crack initiation: a) u_x displacement b) u_y displacement

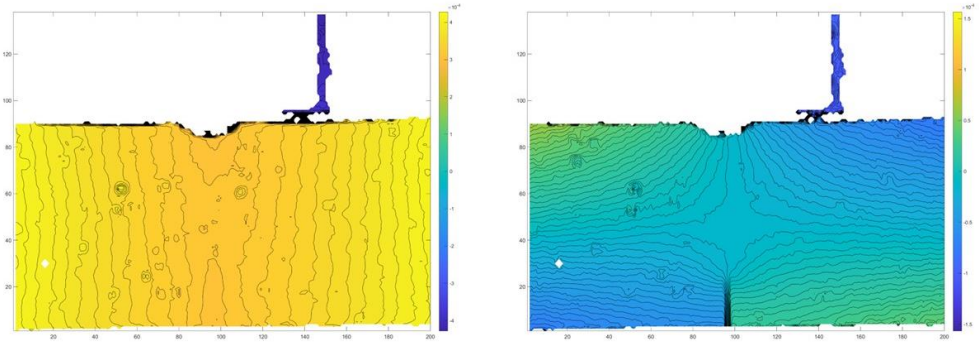

Figure A.12: A2L specimen prior to crack initiation: a) u_x displacement b) u_y displacement

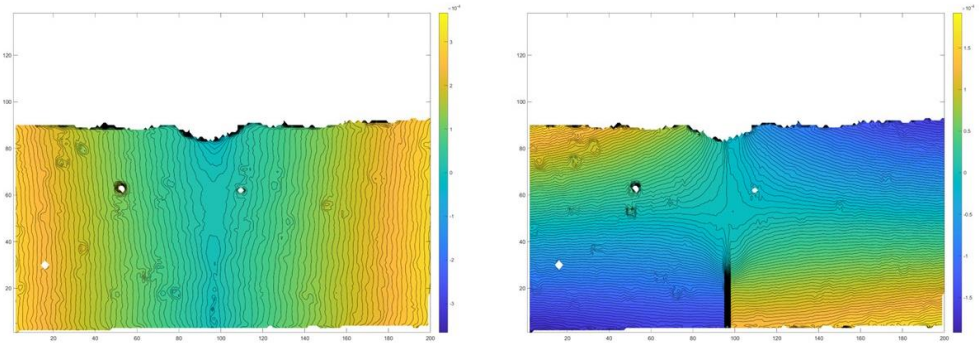

Figure A.13: A2L specimen at crack initiation: a) u_x displacement b) u_y displacement

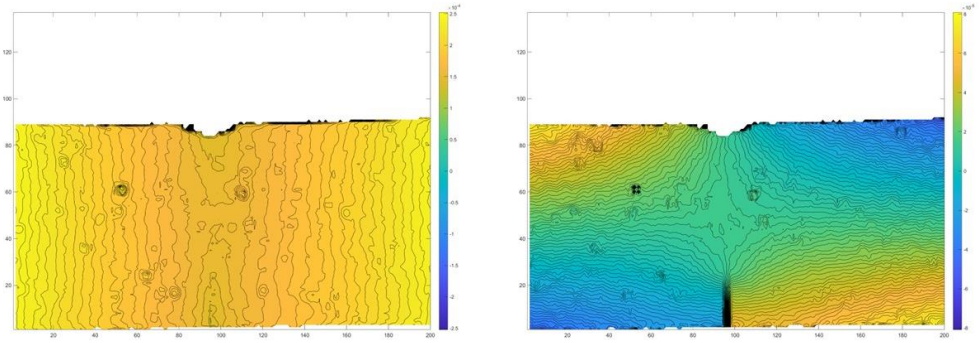

Figure A.14: A2K specimen prior to crack initiation: a) u_x displacement b) u_y displacement

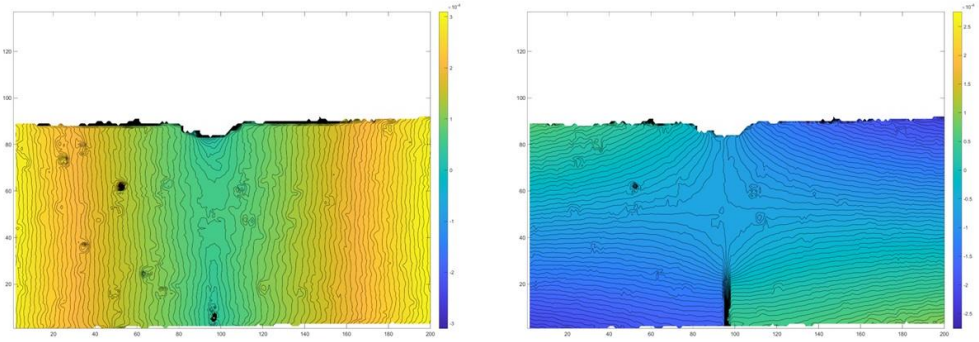

Figure A.15: A2K specimen at crack initiation: a) u_x displacement b) u_y displacement

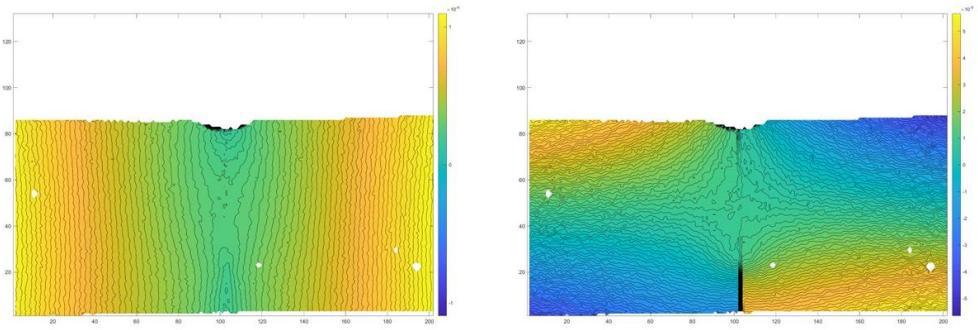

Figure A.16: N1R specimen prior to crack initiation: a) u_x displacement b) u_y displacement

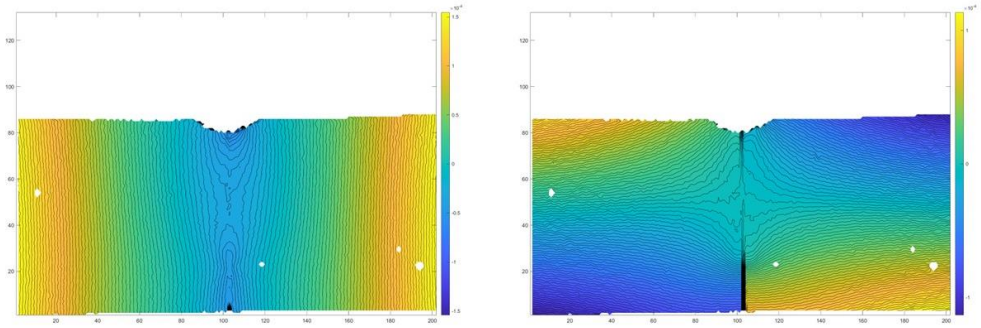

Figure A.17: N1R specimen at crack initiation: a) u_x displacement b) u_y displacement

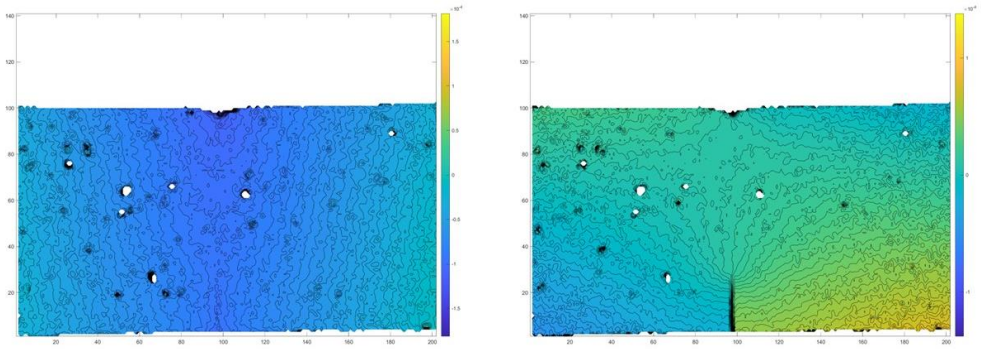

Figure A.18: N1L specimen prior to crack initiation: a) u_x displacement b) u_y displacement

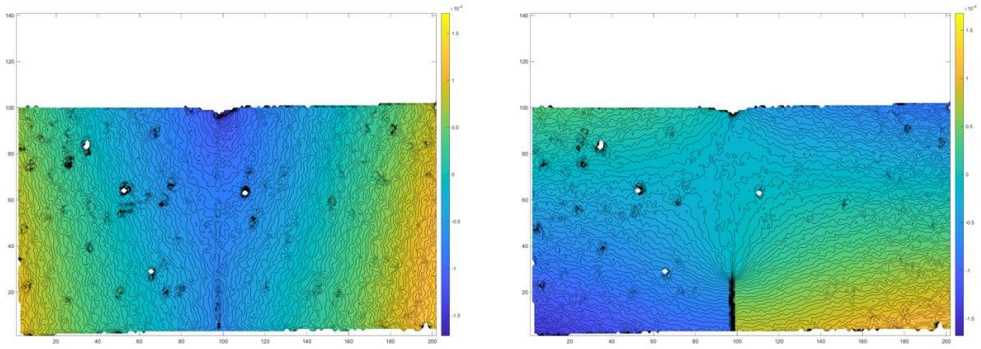

Figure A.19: N1L specimen at crack initiation: a) u_x displacement b) u_y displacement

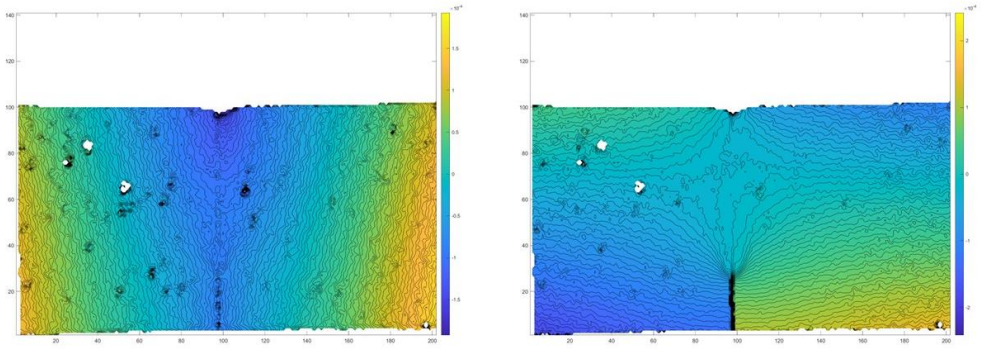

Figure A.20: N1L specimen after crack initiation: a) u_x displacement b) u_y displacement

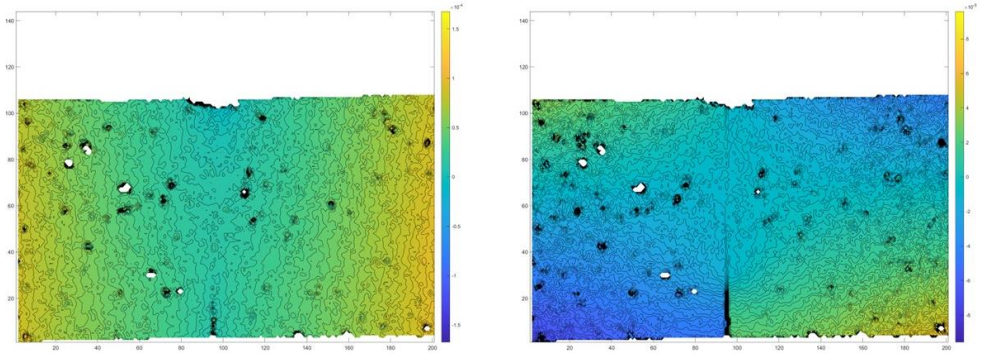

Figure A.21: N1K specimen prior to crack initiation: a) u_x displacement b) u_y displacement

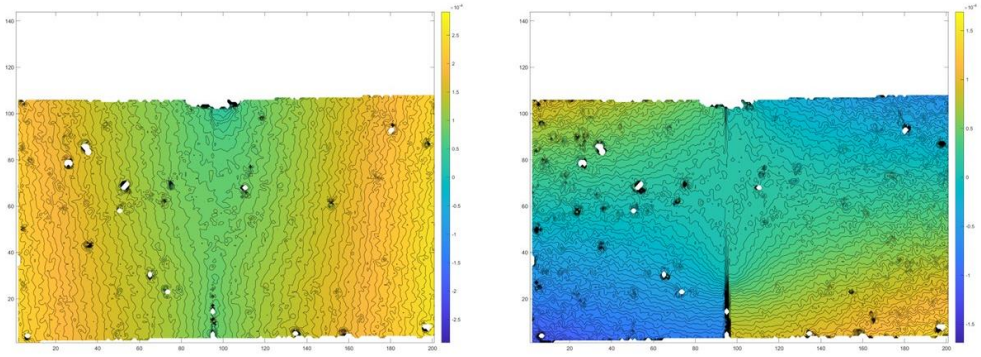

Figure A.22: N1K specimen at crack initiation: a) u_x displacement b) u_y displacement

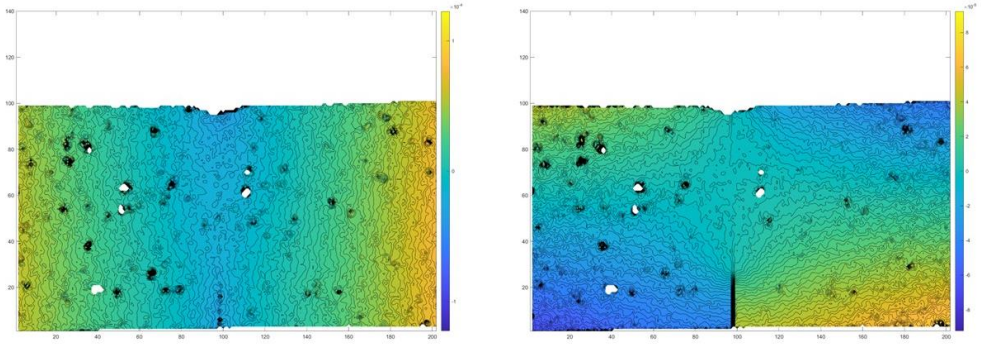

Figure A.23: N2R specimen prior crack initiation: a) u_x displacement b) u_y displacement

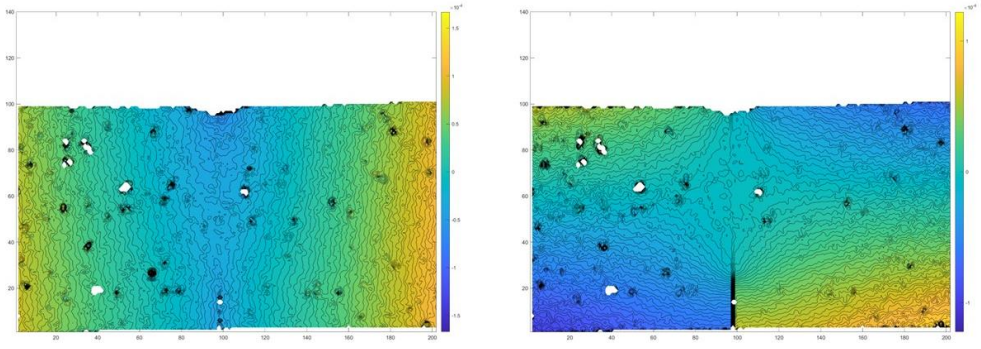

Figure A.24: N2R specimen at crack initiation: a) u_x displacement b) u_y displacement

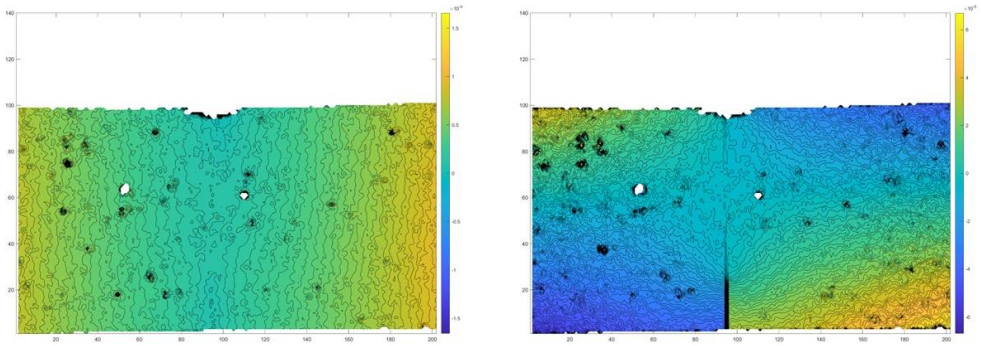

Figure A.25: N2L specimen prior to crack initiation: a) u_x displacement b) u_y displacement

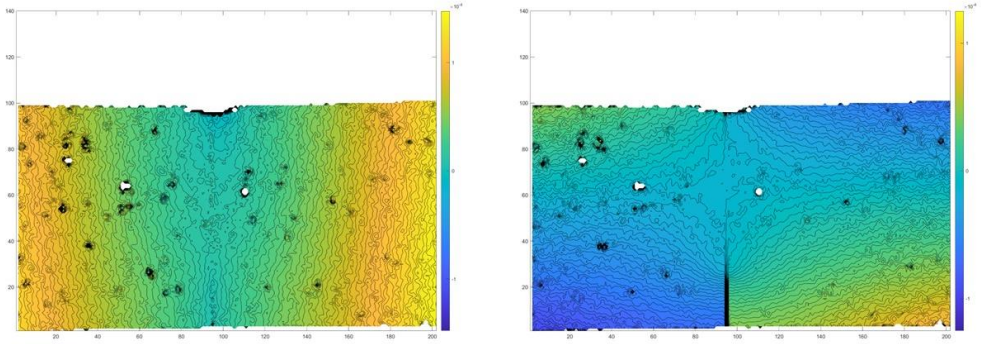

Figure A.26: N2L specimen at crack initiation: a) u_x displacement b) u_y displacement

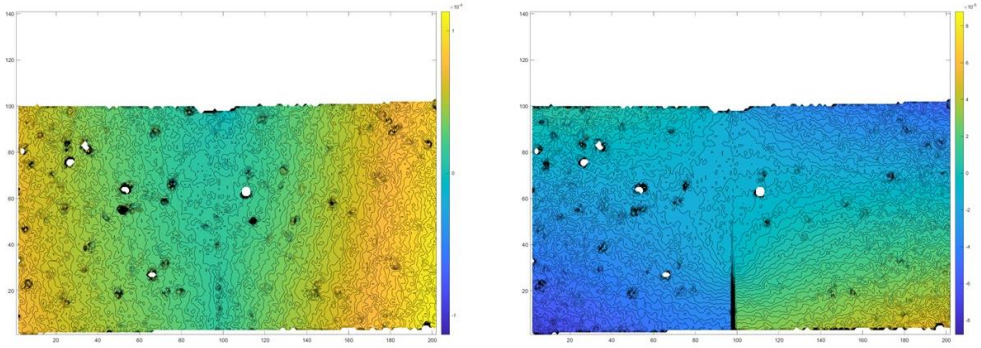

Figure A.27: N2K specimen prior to crack initiation: a) u_x displacement b) u_y displacement

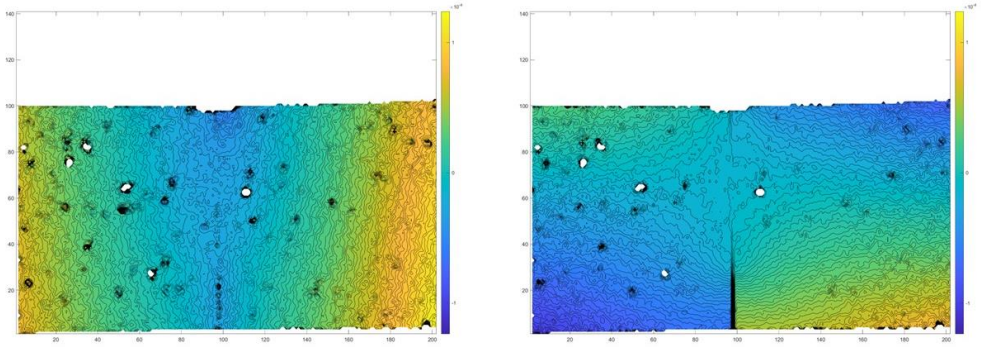

Figure A.28: N2K specimen at crack initiation: a) u_x displacement b) u_y displacement

Appendix B: Additional High Strain-Rate Contour Plots

Appendix B contains contour plots showing the u_x and u_y displacement fields for the high strain-rate specimens. For each manufacturing condition, contours are shown for stages prior to, at, and after crack initiation.

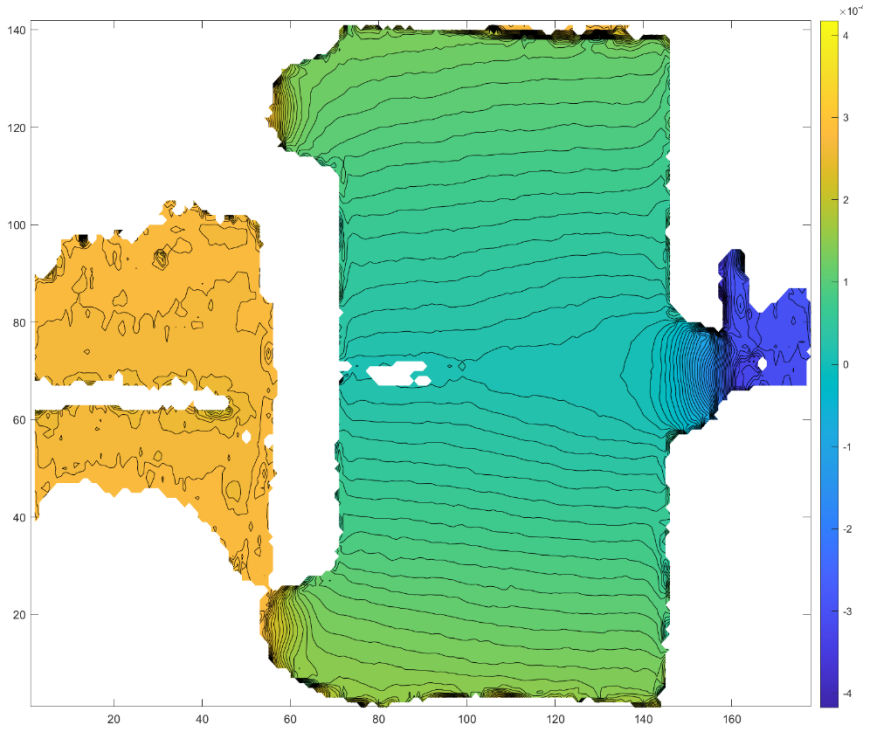

Figure B.1: u_x displacement field of A1 specimen 25 µs prior to crack initiation. Contour increment is 0.008 mm.

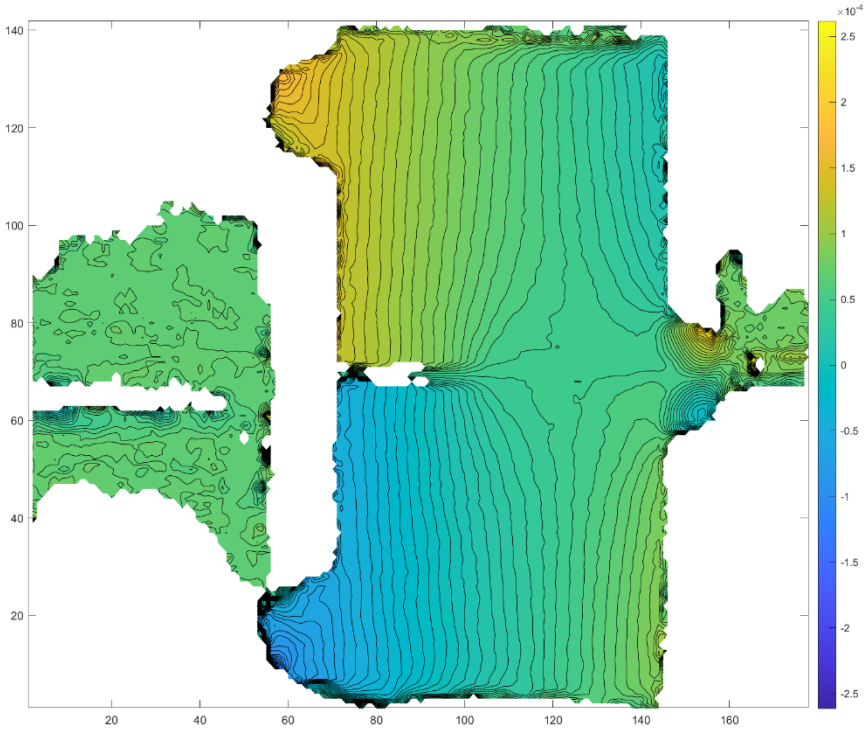

Figure B.2: u_y displacement field 25 μs prior to crack initiation. Contour increment is 0.005mm.

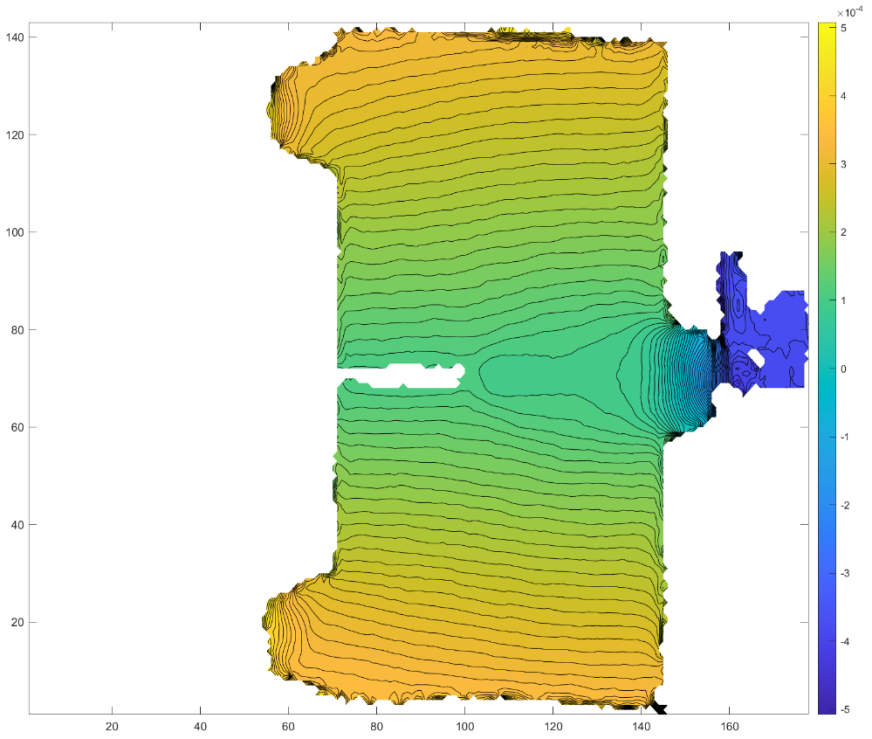

Figure B.3: u_x displacement field of A1 specimen at crack initiation. Contour increment is 0.010 mm.

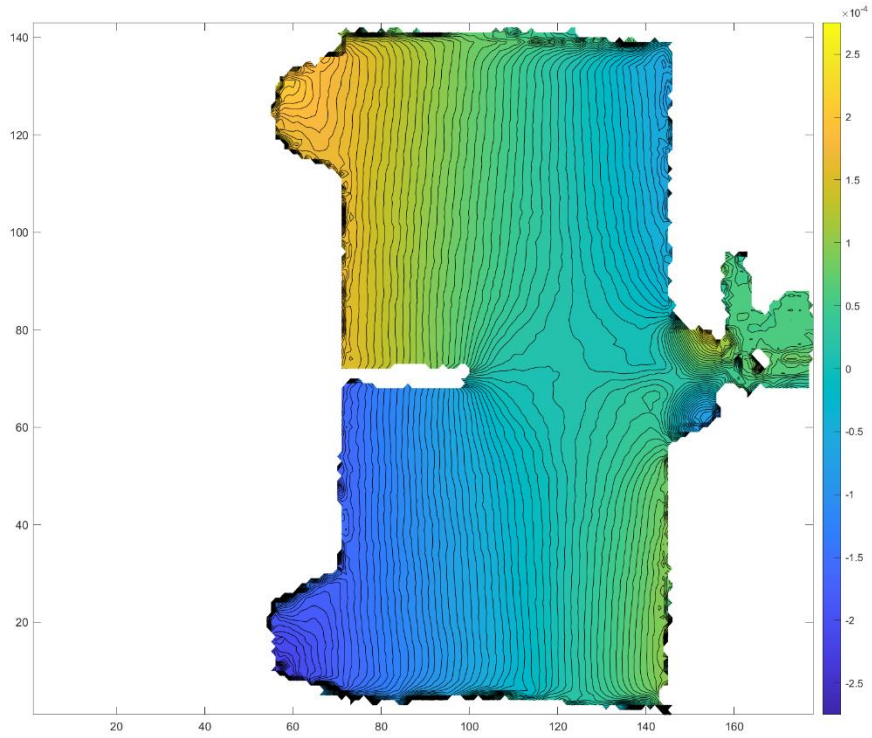

Figure B.4: u_y displacement field of A1 specimen at crack initiation. Contour increment is 0.0055 mm.

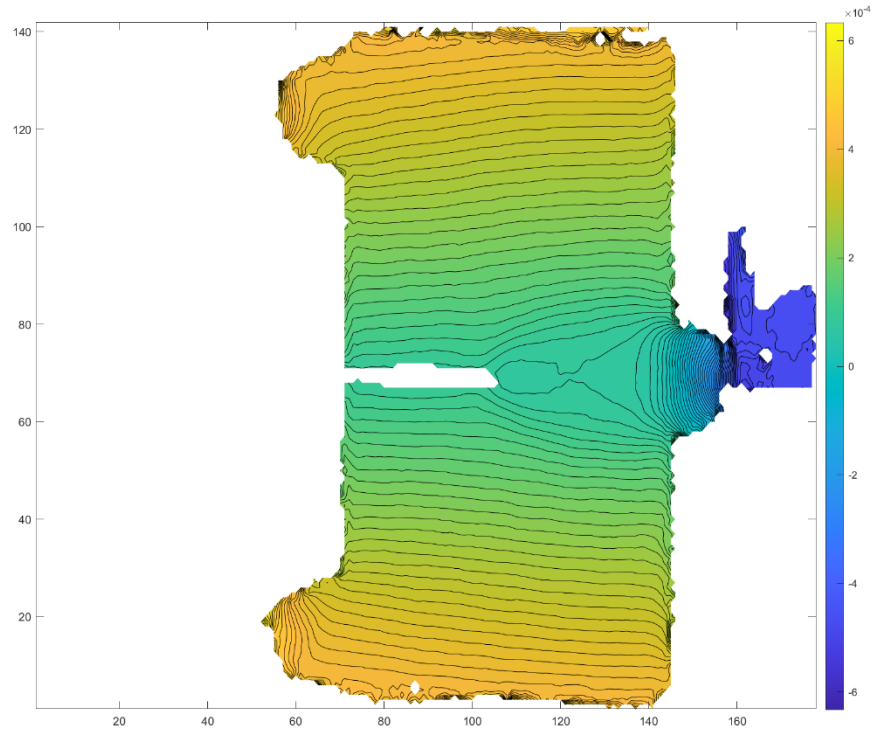

Figure B.5: u_x displacement field of A1 specimen 15 µs after crack initiation. Contour increment is 0.012 mm.

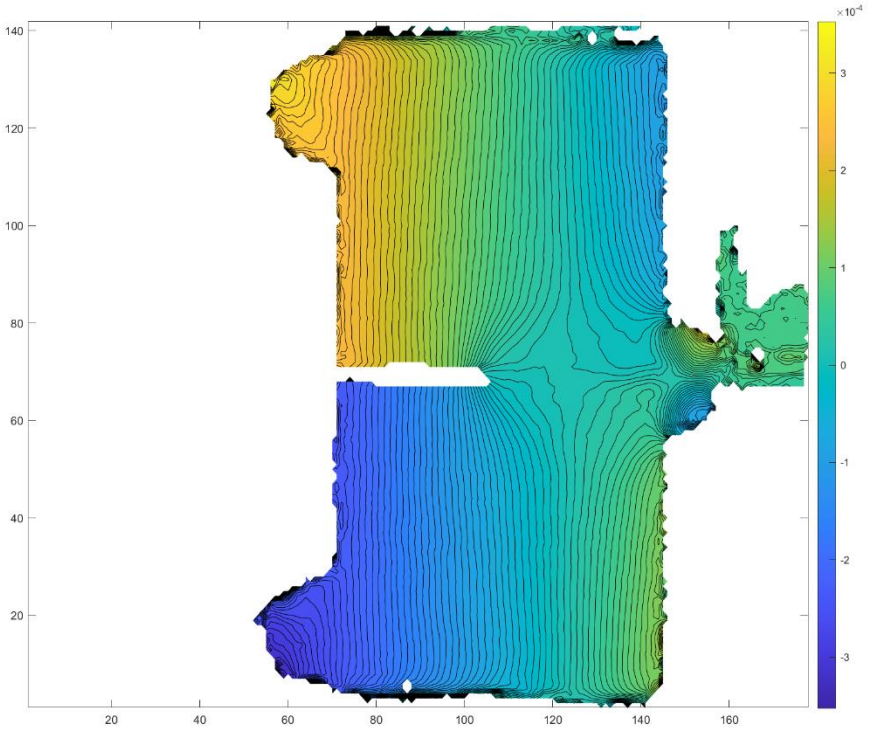

Figure B.6: u_y displacement field of A1 specimen 15 µs after crack initiation. Contour increment is 0.007 mm.

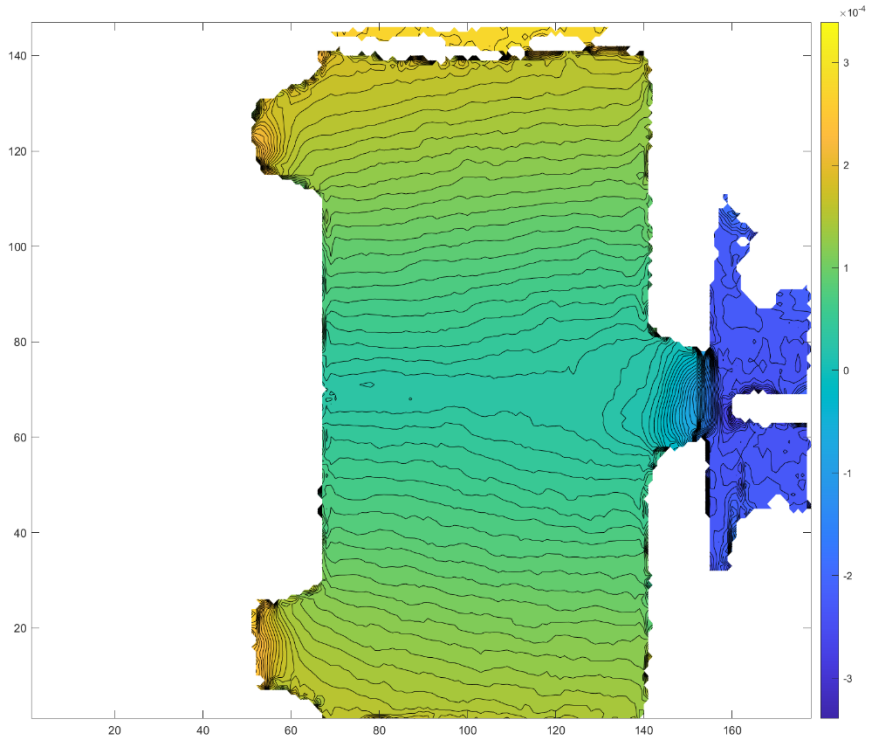

Figure B.7: u_x displacement field of A2 specimen 25 µs prior to crack initiation. Contour increment is 0.007 mm.

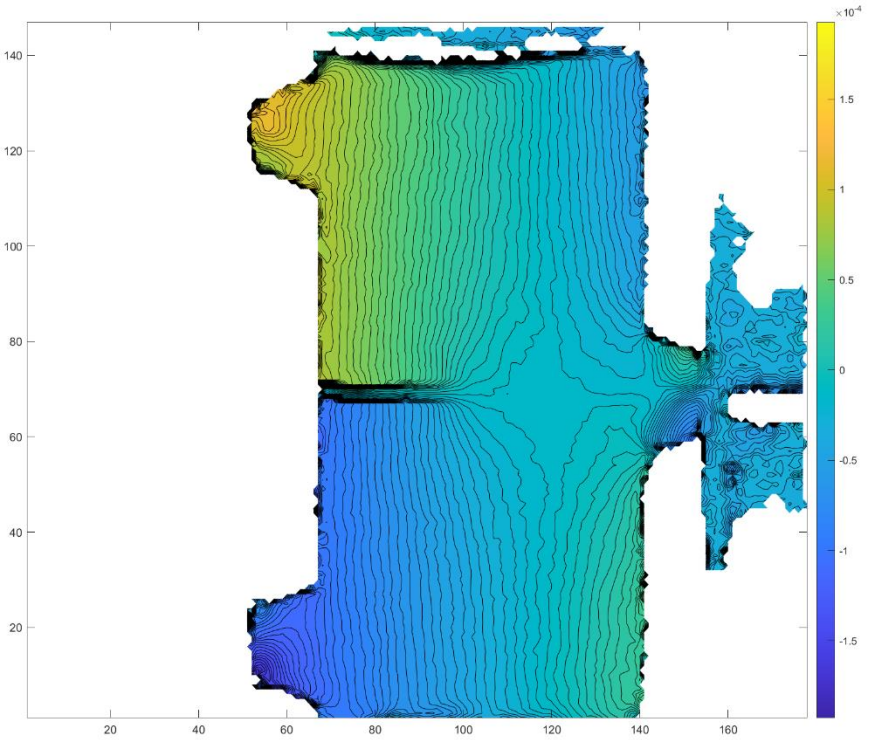

Figure B.8:u_y displacement field of A2 specimen 25 µs prior to crack initiation. Contour increment is 0.004 mm.

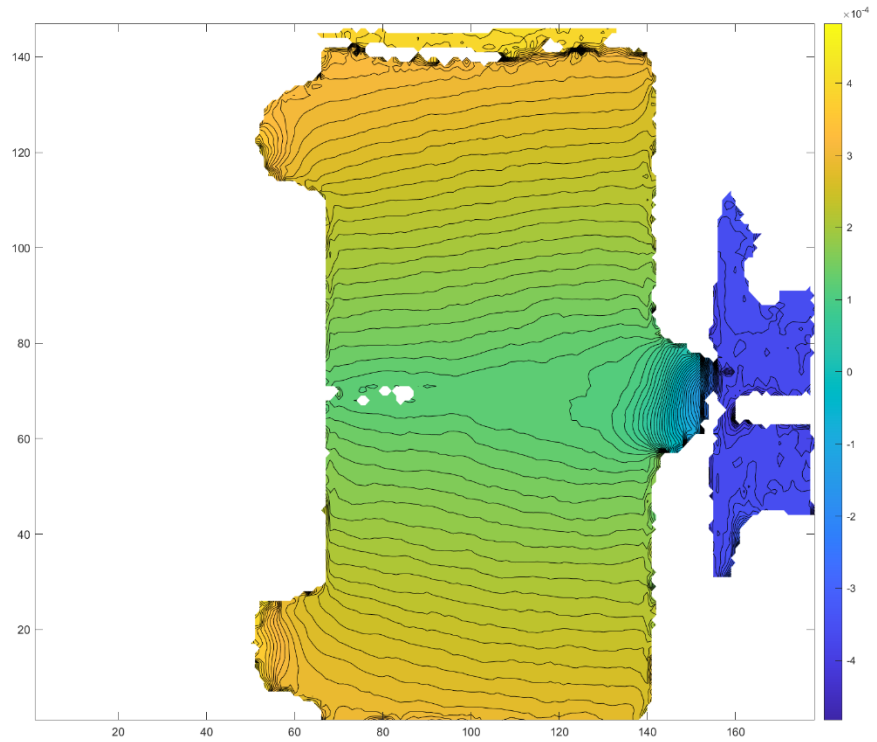

Figure B.9: u_x displacement field of A2 specimen at crack initiation. Contour increment is 0.009 mm.

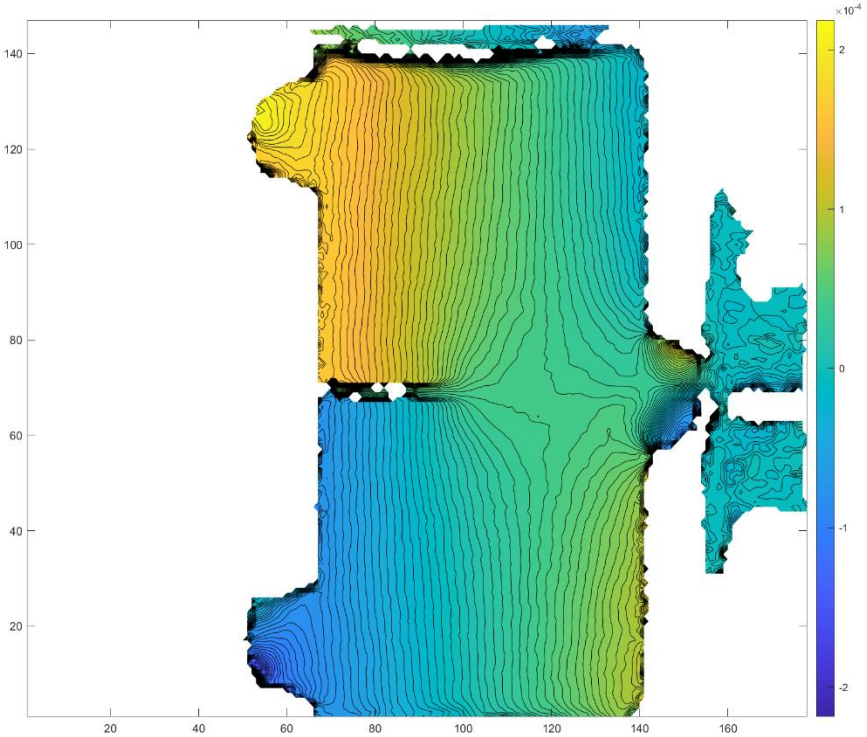

Figure B.10: u_y displacement field of A2 specimen at crack initiation. Contour increment is 0.005 mm.

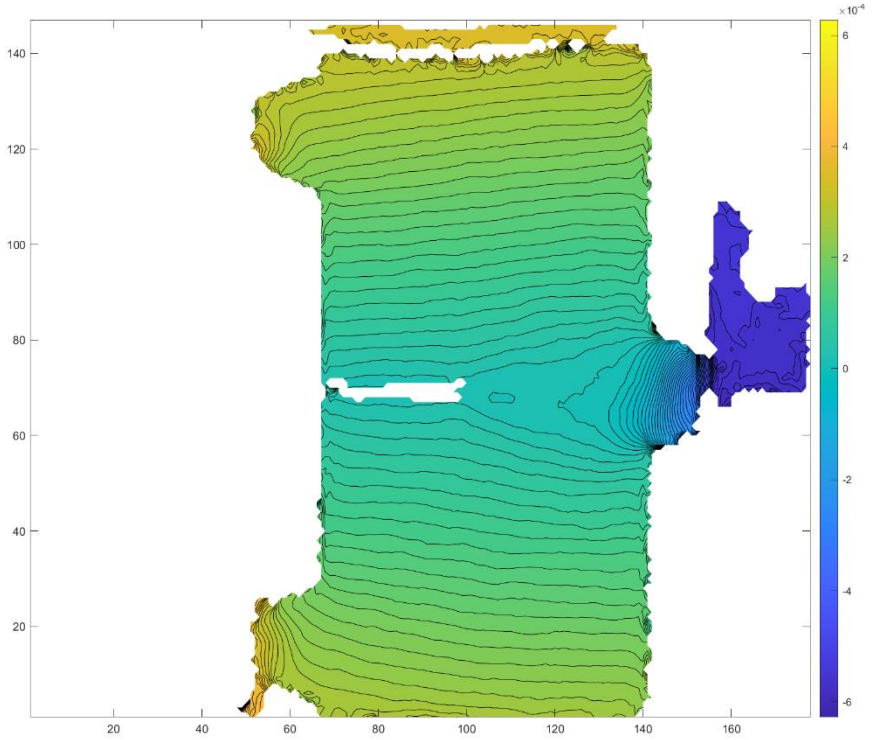

Figure B.11: u_x displacement field of A2 specimen 15 µs after crack initiation. Contour increment is 0.012 mm.

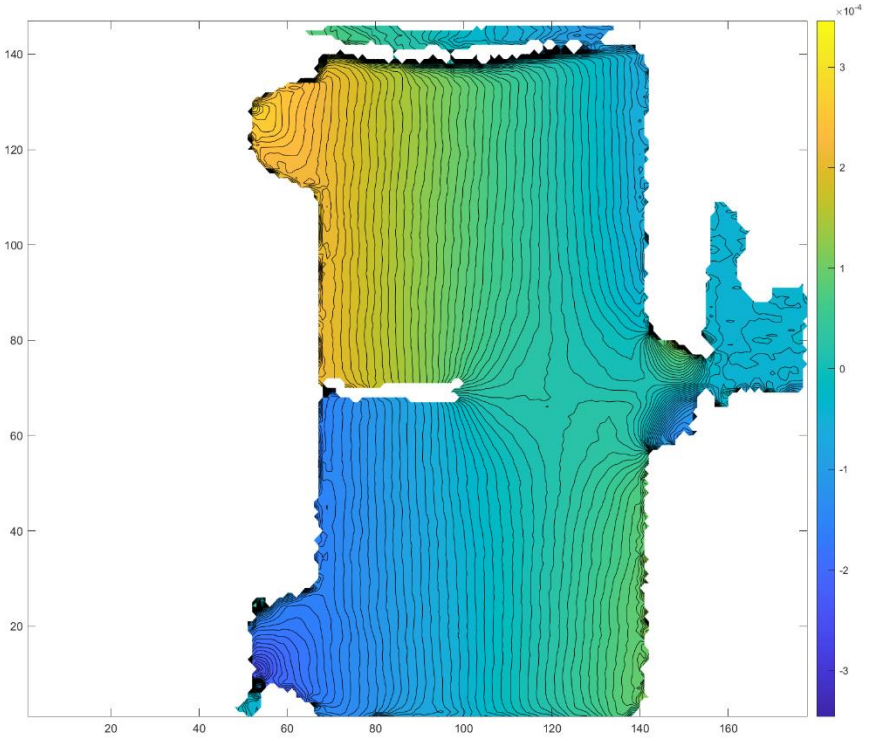

Figure B.12: u_y displacement field of A2 specimen 15 µs after crack initiation. Contour increment is 0.007 mm.

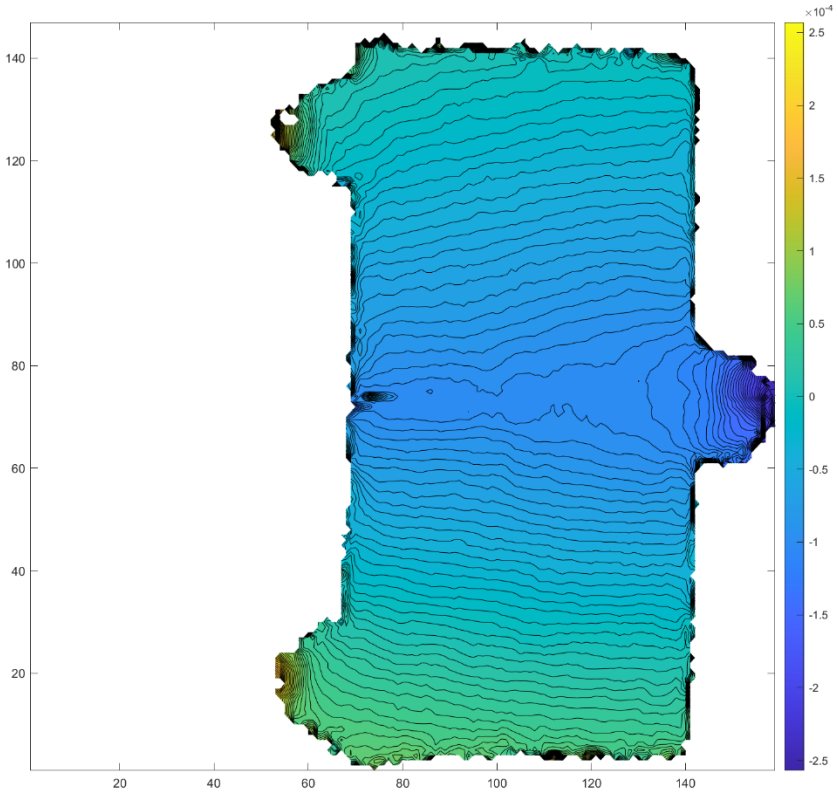

Figure B.13: u_x displacement field of N1 specimen 25 µs prior to crack initiation. Contour increment is 0.005 mm.

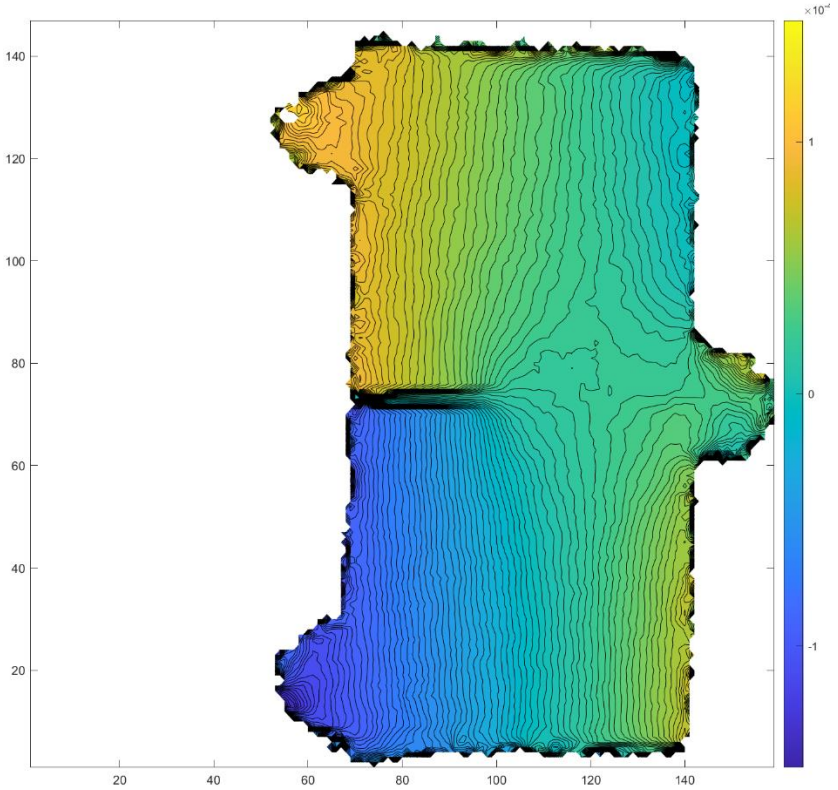

Figure B.14: u_y displacement field of N1 specimen 25 µs prior to crack initiation. Contour increment is 0.004 mm.

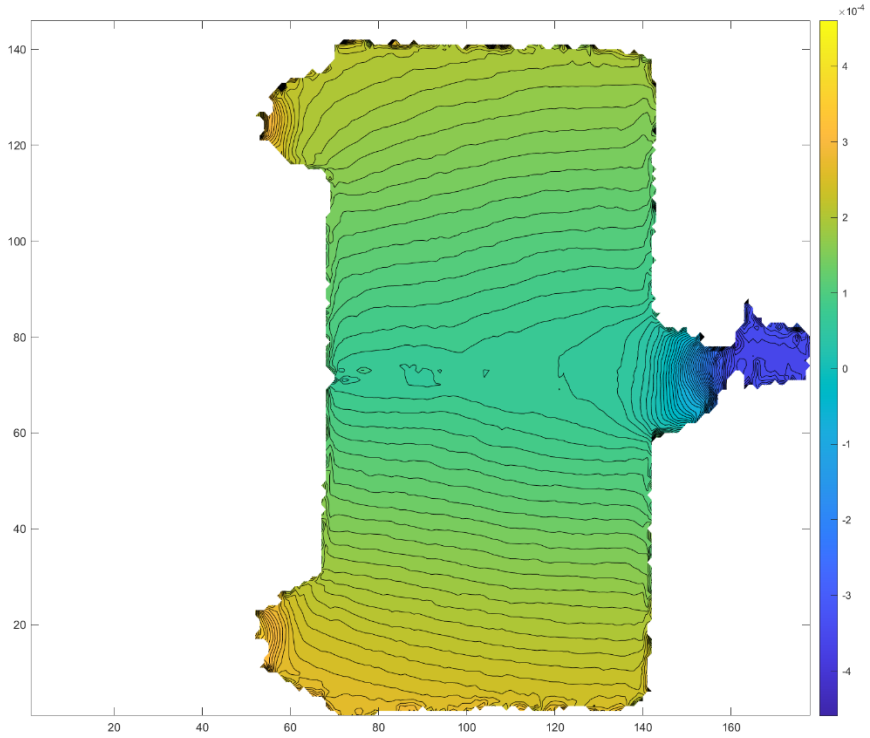

Figure B.15: u_x displacement field of N1 specimen at crack initiation. Contour increment is 0.009 mm.

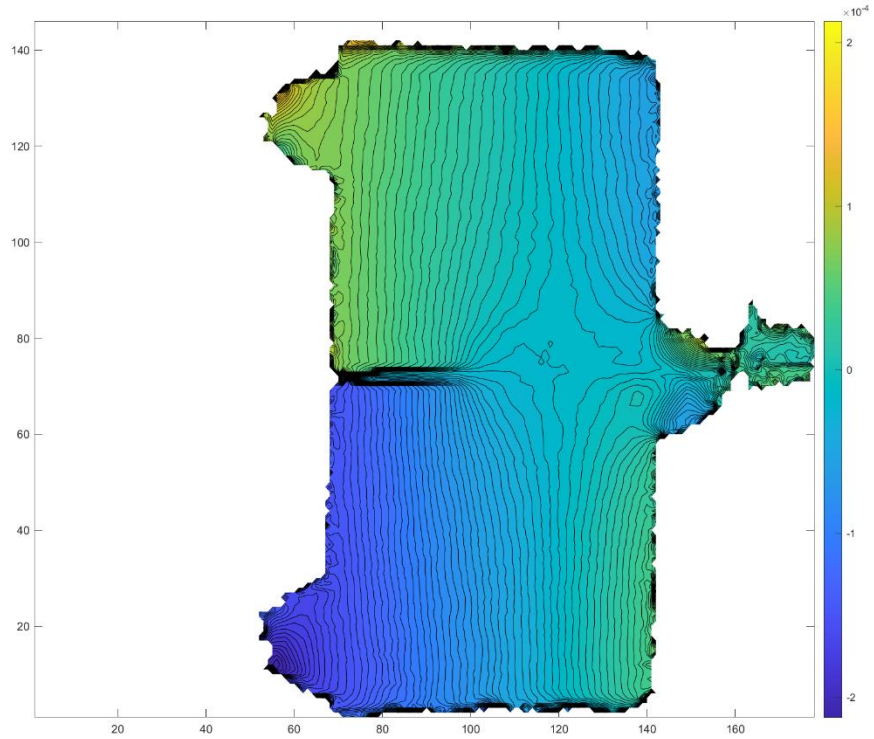

Figure B.16: u_y displacement field of N1 specimen at crack initiation. Contour increment is 0.004 mm.

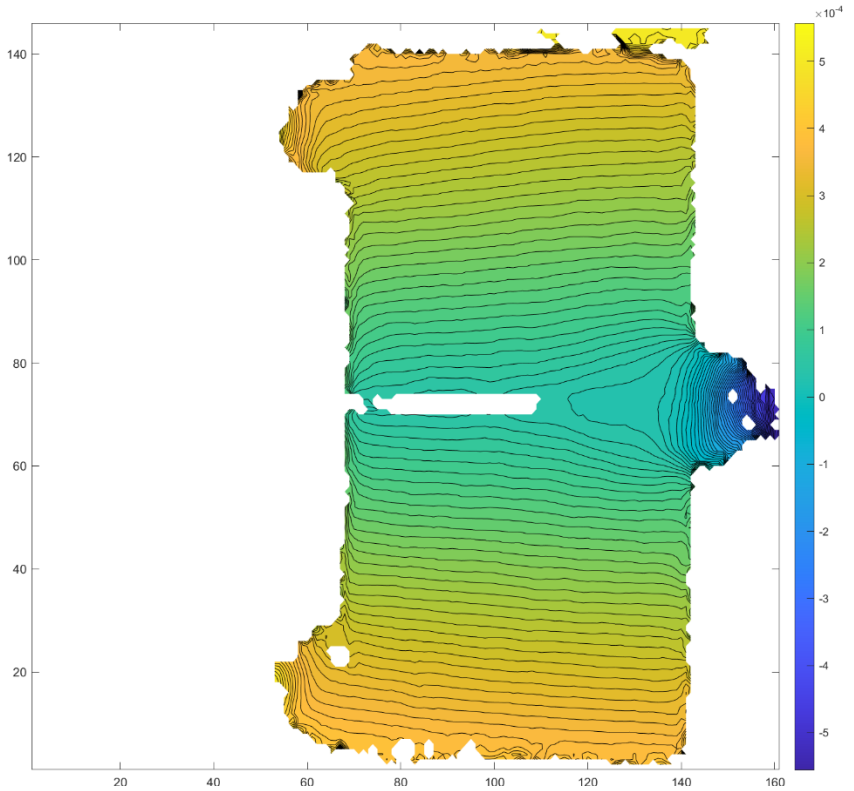

Figure B.17: u_x displacement field of N1 specimen 15 µs after crack initiation. Contour increment is 0.011 mm.

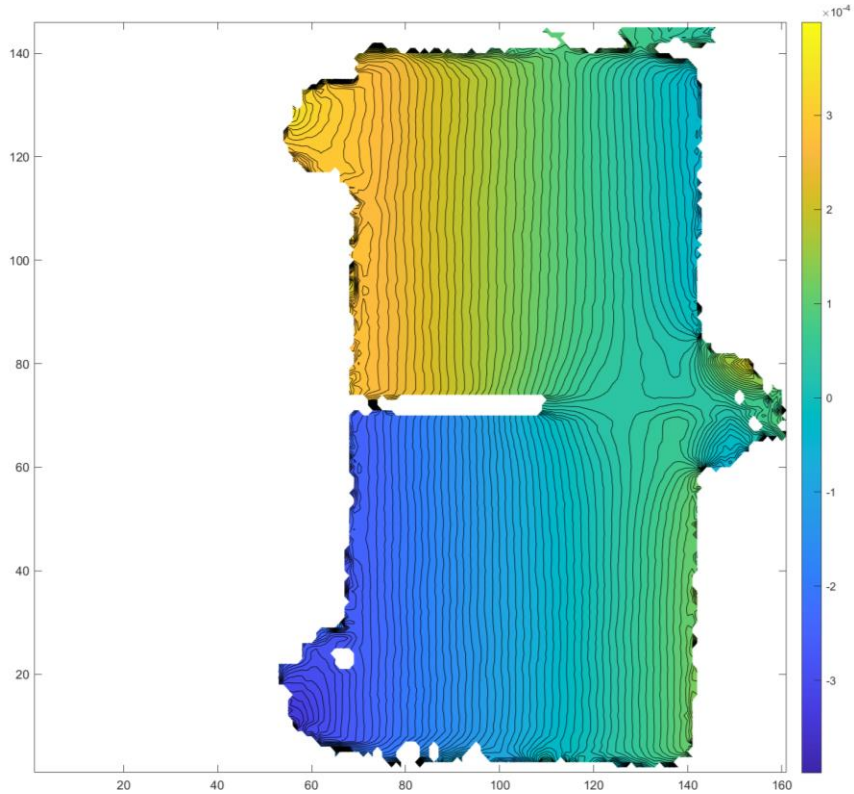

Figure B.18: u_y displacement field of N1 specimen 15 µs after crack initiation. Contour increment is 0.008 mm.

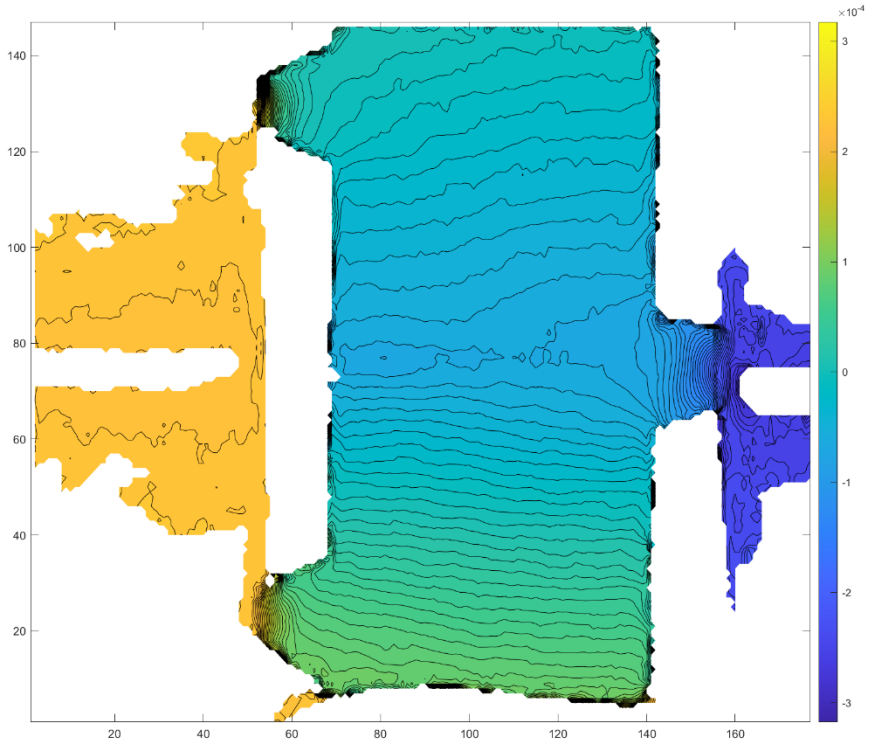

Figure B.19: u_x displacement field of N2 specimen 25 µs prior to crack initiation. Contour increment is 0.006 mm.

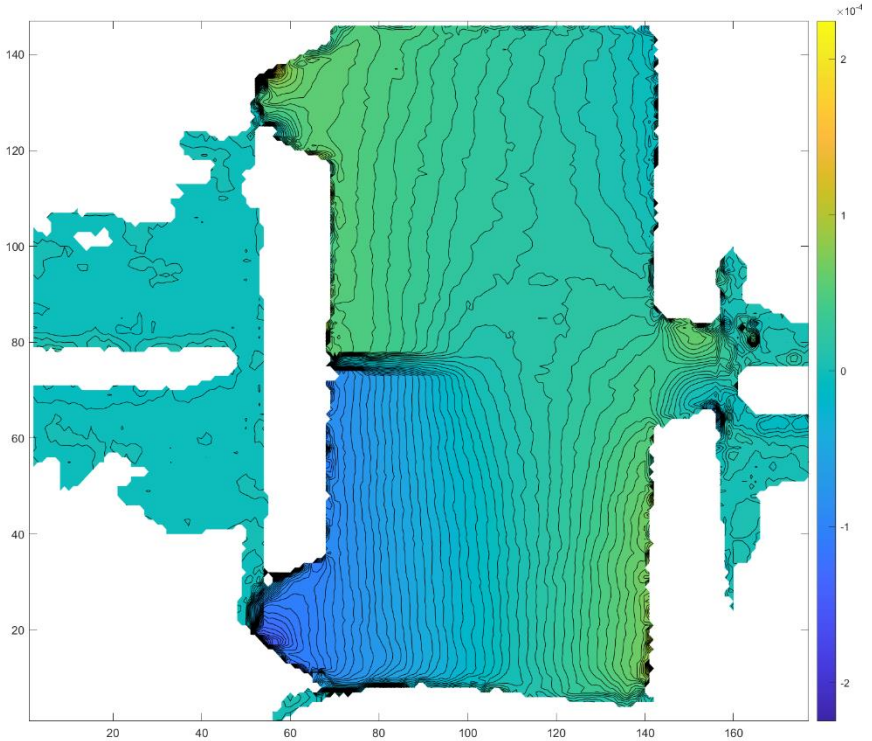

Figure B.20: u_y displacement field of N2 specimen 25 µs prior to crack initiation. Contour increment is 0.004 mm.

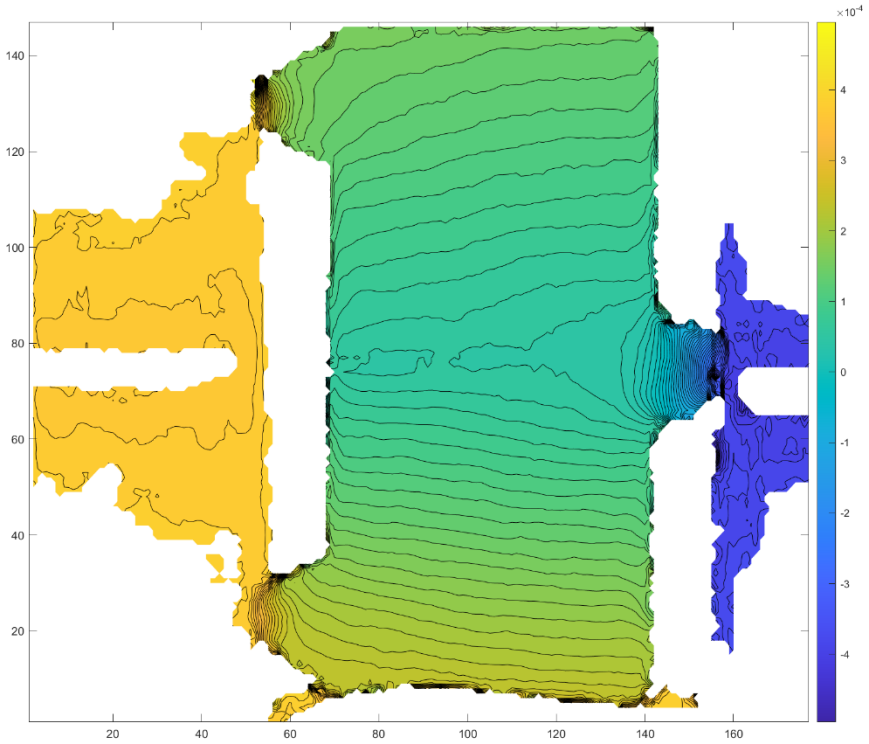

Figure B.21: u_x displacement field of N2 specimen at crack initiation. Contour increment is 0.010 mm.

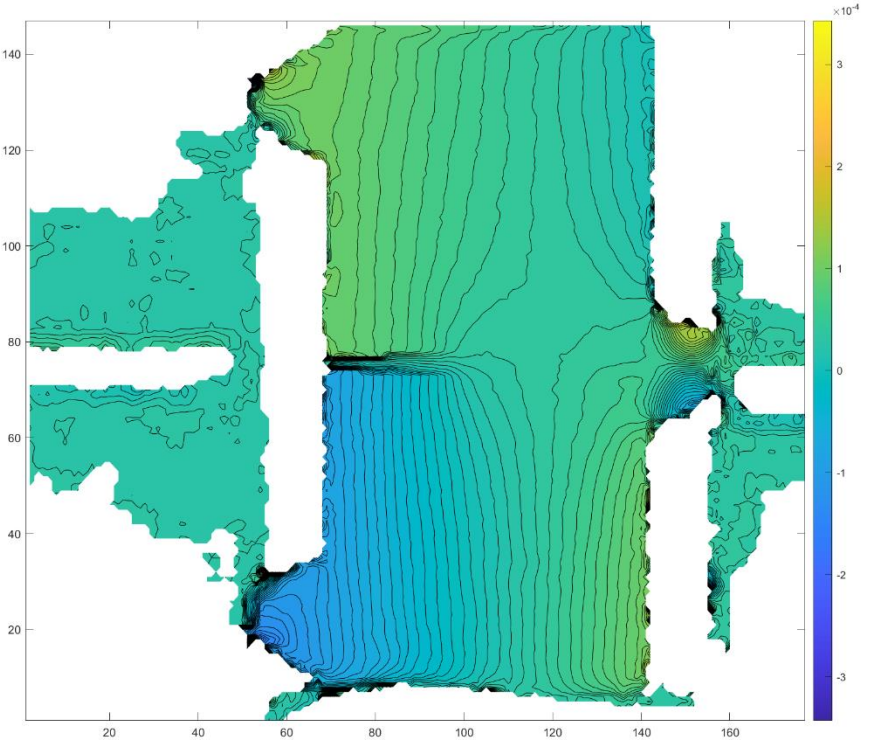

Figure B.22: u_y displacement field of N2 specimen at crack initiation. Contour increment is 0.007 mm.

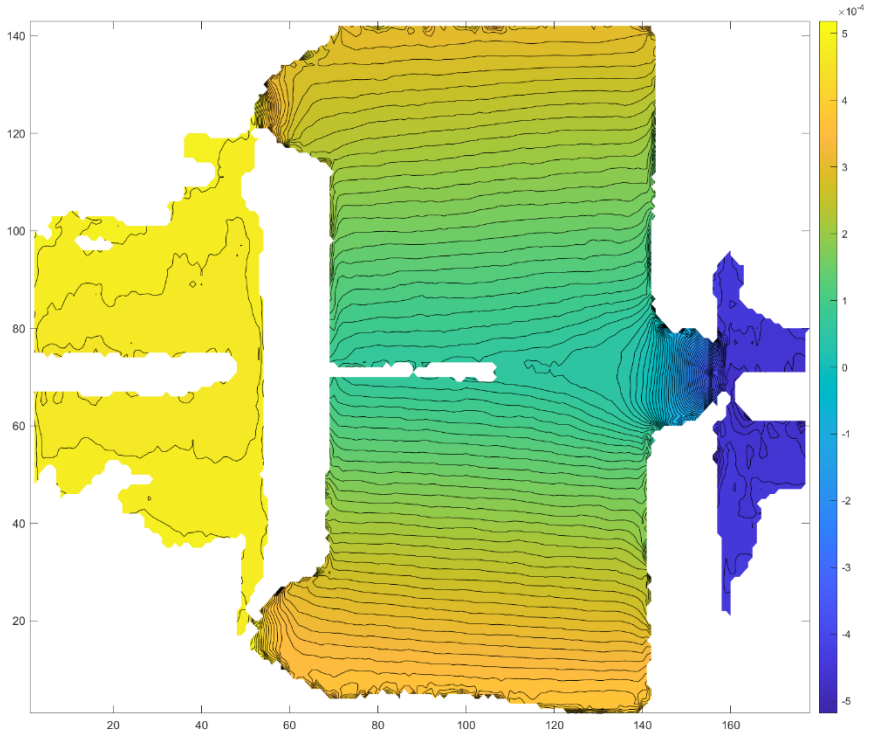

Figure B.23: u_x displacement field of N2 specimen 15 µs after crack initiation. Contour increment is 0.010 mm.

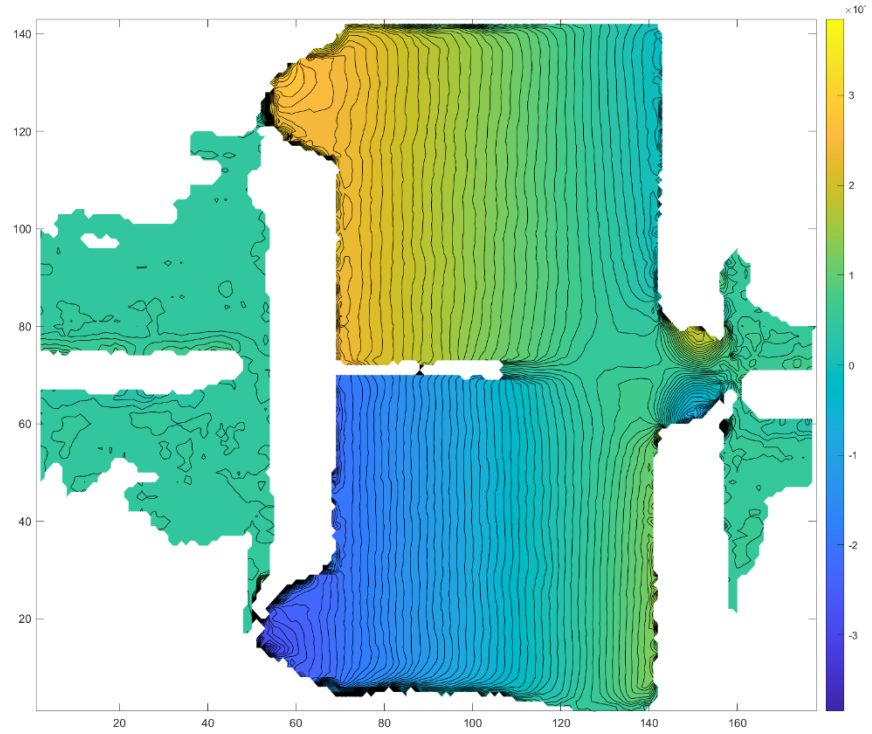

Figure B.24: u_y displacement field of N2 specimen 15 µs after crack initiation. Contour increment is 0.008 mm.

Appendix C: MATLAB Scripts

```
%-----Universal SIF Code-----%
%close all
clear all %#ok<CLSCR>
clc

%FRAMES
start_frame = 1;
end_frame = 99;
filename = 'filename'; %exclude index number
%PARAMETERS
% - Image Scaling -
m = 7;
lines = 100;


for frame_loop = start_frame:end_frame

%crack tip override if cracktip is already known, else = 0 to choose crack tip
ct_override = 0;
%crack direction: 1 = vertical, 0 = horizontal
cdirection = 0;
%used to draw correct contours when selecting crack tip from plot

%exp type = 0 for static, 1 for dynamic (Not yet availible)
mode = 0;
% - DIC Parameters -
scale_factor = 3.47e-5; %m/px
facet_step = 5; %px

% - Material Properties -
E = 2.1e11; %Pa
poisson = 0.3134;
mu = E/(2 * (1 + poisson)); %Pa
kappa = (3 - poisson)/(1 + poisson);

% - Data Range -
B = 0.003;%m
innerbound = 0.5; %r/B
outerbound = 1.5; %r/B
angularbound = 135; % +/- degrees

% - Number of Terms -
Nmin = 1;
Nmax = 15;

%CONTROLS
% - 1 will run code, 0 will skip -
use_uy = 0;
use_ur = 0;
use_uxuy = 1;







%-----END USER INPUT-----%



%---- Load Data Set ----%
fr_num = frame_loop;
    ws = [filename num2str(fr_num)];
    load (ws)
    close all

%Parameter update
xvect = linspace(min(min(Displ_X)),max(max(Displ_X)), lines);
yvect = linspace(min(min(Displ_Y)),max(max(Displ_Y)), lines);

%--- Setup Variables ---%
% Defines matrix
horiz_Displacement = (0);
% Redefines X and Y to properly index the column vectors
X = Index_x + 1;
Y = Index_y + 1;
% k indexes 1 through lenghtx to insure each row is used.
% each item in the matrix is defined by the location (Index X and Y) and the value
for k = 1:length(X);
    horiz_Displacement(Y(k),X(k)) = Displ_X(k);
end
% Repeat steps for Y displacement
vert_Displacement=(0);
for k = 1:length(Y);
```

```
    vert_Displacement(Y(k),X(k)) = Displ_Y(k);
end

%size
sz = size(horiz_Displacement);
w = sz(1,2);
h = sz(1,1);
numrows = h;
numcols = w;


%----- Crack Tip Selection -----%
if ct_override == 0;
    if cdirection == 1;
        % Create contour plots for both matricies
        % choose crack tip location and direction
        f=figure;
        set(f,'position',[0 0 w*m h*m]);
        contourf(flipud(horiz_Displacement),xvect)
        cracktip = ginput(2); %input two points for ctrack tip coordinates -
        %first point is location of crack tip, second defines angle
        close all
    else
        f=figure;
        set(f,'position',[0 0 w*m h*m]);
        contourf(flipud(vert_Displacement),yvect)
        cracktip = ginput(2); %input two points for ctrack tip coordinates -
        %first point is location of crack tip, second defines angle
        close all
    end
else
    cracktip = ct_override;
end

%-----Setup For Proper Coordinates-----%
%Xo and Yo are ct coordinates in old orientation
sz = size(horiz_Displacement);
Xo = cracktip(1,1);
Yo = sz(1,1) - cracktip(1,2);

%phi is angle of the crack, in degrees
phi = atan( (cracktip(2,2)-cracktip(1,2)) / (cracktip(2,1)-cracktip(1,1)) ) * (180/pi);
if cracktip(2,1)-cracktip(1,1) < 0
    phi = phi + 180;
end
if phi > 180
    phi = phi - 360;
end
%phi is now in the proper cordinate system of -180,180 degrees relative
%to original coordinates.

%check if phi is nan (this occurs if you select the same point twice in
%crack tip selection, which gives the vector no direction)
phinan = isnan(phi);
if phinan == true
    phi=0;
end
%now if this happens the direction is set to be 0 degrees



%defines r
horiz_dif = zeros(max(Y), max(X));
vert_dif = zeros(max(Y), max(X));
for k = 1:length(X)
    horiz_dif(Y(k),X(k)) = X(k) - Xo;
    vert_dif(Y(k),X(k)) = Yo - Y(k);
end
r = sqrt(horiz_dif.^2 + vert_dif.^2); %units of subimages
theta = (atan(vert_dif ./ horiz_dif)) .* (180./pi); %in degrees, but on wrong scale
%theta scale correction
sz = size(theta);
for k=1:sz(1,1)
    for i=1:sz(1,2)
        if horiz_dif(k,i) < 0
            theta(k,i) = theta(k,i) + 180;
        end
        if theta(k,i) > 180
            theta(k,i) = theta(k,i) - 360;
        end
        if theta(k,i) > 180
            theta(k,i) = theta(k,i) - 360;
        end
    end
end
%theta now is a 2D matrix where the location in thematrix represetns the
%location in the specimen and the value is the polar coordinates of that
```

```
%subimage on the scale of -180,180 degrees
%creates variable that is the displacement value at ct location


%rotate coordinates by phi degrees
theta = theta-phi;

%and readjust to keep theta on the -180,180 scale
sz = size(theta);
for k=1:sz(1,1)
    for i=1:sz(1,2)
        if theta(k,i) < 180
            theta(k,i) = theta(k,i) + 360;
        elseif theta(k,i) > 180
            theta(k,i) = theta(k,i) - 360;
        end
        if theta(k,i) < 180
            theta(k,i) = theta(k,i) + 360;
        elseif theta(k,i) > 180
            theta(k,i) = theta(k,i) - 360;
        end
        if theta(k,i) > 180
            theta(k,i) = theta(k,i) - 360;
        end
    end
end
% now theta is on the range -180,180 degrees
%in order to make the ur matrix we need the ux and uy matrix in new
%coordinates. everything from this point forward is in cracktip coordinates

hori_adj = horiz_Displacement(round(Yo), round(Xo));
vert_adj = vert_Displacement(round(Yo), round(Xo));

horiz_Displacement = horiz_Displacement - hori_adj;
vert_Displacement = vert_Displacement - vert_adj;
u_resultant = sqrt(horiz_Displacement.^2 + vert_Displacement.^2);

%u_resultant is the resultant displacement. this can be broken down into
%ux and uy in cracktip coordinates

u_resultant_angle = atand(vert_Displacement ./ horiz_Displacement); % this is the angle of the displacement relative to old coordinates
% scale correction
sz = size(u_resultant_angle);
for k=1:sz(1,1)
    for i=1:sz(1,2)
        if horiz_Displacement(k,i) < 0
            u_resultant_angle(k,i) = u_resultant_angle(k,i) + 180;
        end
        if u_resultant_angle(k,i) > 180
            u_resultant_angle(k,i) = u_resultant_angle(k,i) - 360;
        end
        if u_resultant_angle(k,i) > 180
            u_resultant_angle(k,i) = u_resultant_angle(k,i) - 360;
        end
    end
end

%creates ux and uy matrix on cracktip coords
ux = u_resultant .* cosd(u_resultant_angle - phi);
uy = u_resultant .* sind(u_resultant_angle - phi);

 %transform for ur and utheta
cos_theta = cosd(theta);
sin_theta = sind(theta);
ur = (ux .* cos_theta) + (uy .* sin_theta);
utheta = (-1 .* ux .* sin_theta) + (uy .* cos_theta);

r = r .* facet_step .* scale_factor; % r in meters

%----- UNIT CONVERSION FOR DISPLACEMENTS -----%
%convert displacements from mm to meters
ur = ur .* (10.^-3); %ur in meters
uy = uy .* (10.^-3); %uy in meters
ux = ux .* (10.^-3); %ux in meters

%limit data set
j = 1;
region = uy;
for row = 1:numrows
    for col = 1:numcols
        if r(row,col) < B*outerbound
            if r(row,col) > B*innerbound
                if theta(row,col) < angularbound
                    if theta(row,col) > -1 * angularbound
                        r_set(j) = r(row,col);
                        theta_set(j) = theta(row,col);
                        ux_set(j) = ux(row,col);
```

```
                        uy_set(j) = uy(row,col);
                        ur_set(j) = ur(row,col);
                        utheta_set(j) = utheta(row,col);
                        row_set(j) = row;
                        col_set(j) = col;
                        region(row,col) = 1000;
                        j = j + 1;
                    end
                end
            end
        end
    end
end
%If a data point meets all the criteria to be included, it is added to a
%new set for all relevent variables. these new set variables are column
%vectors.
%region is the same as uy, but with the selected values set to a large number so that
%plotting the contours can be used to visualize the selected region


for N=Nmin:Nmax
   % for loop to create cell arrays for the f and g functions
f1 = cell(N,1); % each cell array contains the values for each r,theta coord and for each n
f2 = cell(N,1);
g1 = cell(N,1);
g2 = cell(N,1);
    %r and theta below are in crack tip coordinates and units fo meters/degrees
    %location
if mode == 0 %static
for n = 1:N
    f1{n} = ( (r_set.^(n/2)) ./ (2 .* mu .* sqrt(2*pi)) ) .* ( (kappa .* cosd(n.*theta_set./2))       - (n ./ 2 .* cosd((n-4).*(theta_set./2))) + ((n ./ 2 + (-1).^n
    f2{n} = ( (r_set.^(n/2)) ./ (2 .* mu .* sqrt(2*pi)) ) .* ( (kappa .* sind(n.*theta_set./2))       - (n ./ 2 .* sind((n-4).*(theta_set./2))) + ((n ./ 2 - (-1).^n
    g1{n} = ( (r_set.^(n/2)) ./ (2 .* mu .* sqrt(2*pi)) ) .* ( (kappa .* sind(n.*theta_set./2))       + (n ./ 2 .* sind((n-4).*(theta_set./2))) - ((n ./ 2 + (-1).^n
    g2{n} = ( (r_set.^(n/2)) ./ (2 .* mu .* sqrt(2*pi)) ) .* ( (-1 .* kappa .* cosd(n.*theta_set./2)) - (n ./ 2 .* cosd((n-4).*(theta_set./2))) + ((n ./ 2 - (-1).^n
end
elseif mode == 1 %dynamic
end

%----- AFTER EQUATIONS: EACH SECTION IS FOR EACH DISPLACEMENT SET -----%




%%%%%%%%%
%---uy---%
%%%%%%%%%
if use_uy == 1
    %fill the matrixes with g1 and g2 for uy displcaments
    uy_matA = zeros(2*N, 2*N);
    % the first outer for-loop cycles the row for the top half of the matrix,
    %filling it in with the proper sums
    for row_n = 1:N
        %inner for-loops cycle through the column, the first one fills in f{n}
        %for the left half
        %the second loop fills in g{n} for the right half
      for col_n = 1:N
        uy_matA(row_n, col_n) = sum(g1{row_n} .* g1{col_n});
      end
      for col_n = N+1:2*N
         g_col = col_n - N; %this sets the correct index of g in the correct location of A
         uy_matA(row_n, col_n) = sum(g1{row_n} .* g2{g_col});
      end
    end
    %the second outer for-loop cycles through the bottom half. interior loops
    %mirror those above
    for row_n = N+1:2*N
         g_row = row_n - N;
         for col_n = 1:N
            uy_matA(row_n, col_n) = sum(g2{g_row} .* g1{col_n});
         end
         for col_n = N+1:2*N
            g_col = col_n - N;
            uy_matA(row_n, col_n) = sum(g2{g_row} .* g2{g_col});
         end
    end
    % matB is the displacement matrix.
    uy_matB = zeros(2*N,1);
    for row_n = 1:N
      uy_matB(row_n, 1) = sum(g1{row_n} .* uy_set);
    end
    for row_n = N+1:2*N
        uy_matB(row_n, 1) = sum(g2{row_n - N} .* uy_set);
    end
    uy_matK = uy_matA\uy_matB;
    eval(['uy_results_' num2str(fr_num) '(N,1) = uy_matK(1,1);']);
    eval(['uy_results_' num2str(fr_num) '(N,2) = uy_matK(N+2,1);']);
end %uy section end
```

```
%%%%%%%%%
%---ur---%
%%%%%%%%%
if use_ur == 1
    %F is the function for KI, G is the function for KII
    F = cell(N,1);
    G = cell(N,1);
    %Fill F and G with the proper functions
    for n = 1:N
        F{n} = f1{n}.*cosd(theta_set) + g1{n}.*sind(theta_set);
        G{n} = f2{n}.*cosd(theta_set) + g2{n}.*sind(theta_set);
    end
    %then fill the matrixes with F and G
    ur_matA = zeros(2*N, 2*N);
    % the first outer for-loop cycles the row for the top half of the matrix,
    %filling it in with the proper sums
    for row_n = 1:N
        %inner for-loops cycle through the column, the first one fills in f{n}
        %for the left half
        %the second loop fills in g{n} for the right half
        for col_n = 1:N
            ur_matA(row_n, col_n) = sum(F{row_n} .* F{col_n});
        end
        for col_n = N+1:2*N
            g_col = col_n - N; %this sets the correct index of g in the correct location of A
            ur_matA(row_n, col_n) = sum(F{row_n} .* G{g_col});
        end
    end
    %the second outer for-loop cycles through the bottom half. interior loops
    %mirror those above
    for row_n = N+1:2*N
        g_row = row_n - N;
        for col_n = 1:N
            ur_matA(row_n, col_n) = sum(G{g_row} .* F{col_n});
        end
        for col_n = N+1:2*N
            g_col = col_n - N;
            ur_matA(row_n, col_n) = sum(G{g_row} .* G{g_col});
        end
    end
    % matB is the displacement matrix.
    ur_matB = zeros(2*N,1);
    for row_n = 1:N
        ur_matB(row_n, 1) = sum(F{row_n} .* ur_set);
    end
    for row_n = N+1:2*N
        ur_matB(row_n, 1) = sum(G{row_n - N} .* ur_set);
    end
    ur_matK = ur_matA\ur_matB;
    eval(['ur_results_' num2str(fr_num) '(N,1) = ur_matK(1,1);']);
    eval(['ur_results_' num2str(fr_num) '(N,2) = ur_matK(N+2,1);']);
end %end ur section




%%%%%%%%%%%%%%%%%%%%
%---uxuy combined---%
%%%%%%%%%%%%%%%%%%%%
if use_uxuy == 1
    %fill the matrixes with g1 and g2 for uy displcaments
    uxuy_matA = zeros(2*(length(ux_set)), (2*N)+2);
    % the first outer for-loop cycles the row for the top half of the matrix,
    %filling it in with the proper sums
    for row_n = 1:length(ux_set)
        %inner for-loops cycle through the column, the first one fills in f{n}
        %for the left half
        %the second loop fills in g{n} for the right half
        for col_n = 1:N
            uxuy_matA(row_n, col_n) = f1{col_n}(row_n);
        end
        for col_n = N+2:2*N+1
            uxuy_matA(row_n, col_n) = f2{(col_n-1) - N}(row_n);
        end
    end
    %the second outer for-loop cycles through the bottom half. interior loops
    %mirror those above
    for row_n = length(ux_set) + 1 : 2 * length(ux_set)
        for col_n = 1:N
            uxuy_matA(row_n, col_n) = g1{col_n}(row_n - length(ux_set));
        end
```

```
        for col_n = N+2:2*N+1
            uxuy_matA(row_n, col_n) = g2{(col_n-1) - N}(row_n - length(ux_set));
        end
    end
    %add 1s and 0s for rigid body terms
    for row_n = 1 : length(ux_set)
        col_n = N + 1;
        uxuy_matA(row_n, col_n) = 1;
        col_n = 2*N + 2;
        uxuy_matA(row_n, col_n) = 0;
    end
    for row_n = length(ux_set)+1 : 2*(length(ux_set))
        col_n = N + 1;
        uxuy_matA(row_n, col_n) = 0;
        col_n = 2*N + 2;
        uxuy_matA(row_n, col_n) = 1;
    end
    % matB is the displacement matrix.
    uxuy_matB = zeros(2 * length(ux_set), 1);
    for row_n = 1:length(ux_set)
        uxuy_matB(row_n, 1) = ux_set(row_n);
    end
    for row_n = length(ux_set) + 1 : 2 * length(ux_set)
        uxuy_matB(row_n, 1) = uy_set(row_n - length(ux_set));
    end
    uxuy_AA = uxuy_matA.' * uxuy_matA;
    uxuy_matK = inv(uxuy_AA) * uxuy_matA.' * uxuy_matB;
    eval(['uxuy_results_' num2str(fr_num) '(N,1) = uxuy_matK(1,1);']);
    eval(['uxuy_results_' num2str(fr_num) '(N,2) = uxuy_matK(N+2,1);']);
    eval(['uxuy_results_' num2str(fr_num) '(N,3) = uxuy_matK(2,1);']);
end %end uyux section

end %end Nmin:Nmax For loop



%%%%%%%%%%%%%%
%%---PLOTS---%%
%%%%%%%%%%%%%%

% X Displacement
%{a
f=figure;
set(f,'position',[0 0 w*m h*m]);
contourf(flipud(ux),linspace(min(min(ux)),max(max(ux)), 100));
%}



% Y Displacement
%{a
f=figure;
set(f,'position',[0 0 w*m h*m]);
contourf(flipud(uy),linspace(min(min(uy)),max(max(uy)), 100));
%}



%Region Plot
%{a
f=figure;
set(f,'position',[0 0 w*m h*m]);
contourf(flipud(region),linspace(min(min(uy)),max(max(uy)), 100));
%}




end %end zzz loop


%results interpreter copy
%uxuy results interpreter

N = 8;
n = num2str(N);

all_results = zeros(end_frame - start_frame, 3);

for k = start_frame:end_frame
    s = num2str(k);
    all_results(k,1) = eval(['uxuy_results_' num2str(k) '(' n ',1)']);
    all_results(k,2) = eval(['uxuy_results_' num2str(k) '(' n ',2)']);
    all_results(k,3) = eval(['uxuy_results_' num2str(k) '(' n ',3)']);
end
```

```
open all_results
```

```
Error using load
Unable to find file or directory 'filename1'.

Error in Static_SIF_Master (line 65)
    load (ws)
    ^^^^^^^^^
```

Published with MATLAB® R2024b

Contents


```
%DICFE Looper

%INSTRUCTIONS
%{
1. All Code must be copied into the code folder
2. All Aramis txt files must be immediately outside of the code folder
3. Make sure the .cae, .jnl, and Nodes.csv files are in the code folder???
4. Copy all Job.inp files into the code folder (run Jobfile_exp.m code to create
these
5. Set correct fn, startframe, endframe, scale_f, step, thickness, loadpoint (run LoadpointFinder.m), and folder
%}

clear all
clc


run=1; %1 to run files, 0 just to create BCs

fn = 'N2R40-Stage-0-';
Nodefn = 'Nodes.csv';
startframe = 1;
endframe = 22;
scale_f = 0.0229; %mm/px
step = 10; %px
thickness = 0.002; %m
loadpoint = [97.2,26.6]; %run LoadpointFidner to get this
folder = 'C:\Users\ake0012\Documents\DIC-FE\N2 Experiments\Code Folder R'; %location of code folder, copy from top
```

read/map section

```
for Looper = startframe:endframe
    if Looper == startframe
        movefile(['../' fn num2str(Looper) '.txt'], '.');
    else
        movefile(['../' fn num2str(Looper) '.txt'], '.');
        movefile([fn num2str(Looper-1) '.txt'], ['../' fn num2str(Looper-1) '.txt']);
    end

    DIC_FE_Read_Aramis_files
    DISP_MAPPING
    Looper
    if Looper == endframe
        movefile([fn num2str(Looper) '.txt'], ['../' fn num2str(Looper) '.txt']);
    end

end %read/mapping loop, all excel files should be created
```

```
Error using movefile
No matching files named 'C:\Users\ake0012\Documents\DIC-FE\N2R40-Stage-0-1.txt' were found.
```

```
Error in DICFE_Looper (line 32)
        movefile(['../' fn num2str(Looper) '.txt'], '.');
        ^^^^^^^^^^^^^^^^^^^^^^^^^^^^^^^^^^^^^^^^^^^^^^^^
```

BC to inp section

```
%Now turn excel into inp
BCfileconverter
%Now all inp's are created.
```

abq job commands section

```
%run jobs (NOTE: ALL JOB.inp FILES MUST BE IN FOLDER)
if run==1
status1 = system(['cd ' folder]);
for Looper = startframe:endframe
status = system(['abq2016 job=Job-' num2str(Looper) ' cpus=4'])
end %end jobs loop, all jobs should be running
end
```

dat to mat

```
%dat_to_MATLAB_DICFE_Version
```

Published with MATLAB® R2024b

```
% PHI_X formula changed as per dynamic formulae
% Line 98 to define LoadPoint
format long;
N = 3; % number of terms
MixedModeFlag = true; % If the problem is mixed mode enter true, If it is Mode-I enter false
Step_Size = step; % step size is 5 pixels
B = thickness;% Thickness in meters
sf = scale_f; % Scale factor in mm/pixel
alphaInitial = 0; % enter the angle(degrees) between global x-axis and Local x-axis(Local:crack tip co-ordinate system): in simple terms, alpha is angle between x a
rOverB_LowerLimit = 0.35;
rOverB_UpperLimit = 1.35;
theta_regions = [-150  150]; % Give angle between -180 and 180 degrees. eg:    [-150 -120; -110 -10; 10 110; 120 150]
avg_grid_size = 1; % size of averaging grid around the node. This paramer is for averagng the data.
% all the parameters related to N=1, for dynamic formulation
rho = 1010; %1010; % mass density,kg/m^3
mue = 0.987e6; % shear modulus,N/m^2.987e6..180e6
nue = 0.34; % poisson's ratio.0.348
time = 1e-6; %time in seconds: time step between EACH IMAGE.
C_Initial = 0; % Crack velocity corresponding to first image. For static problems it can be given as zero.
No_CRACK_TIP_ROTA = true; %IF "NO CRACK TIP ROTATION" IS true, IT(CRACK TIP) WILL NOT ROTATE. CRACK KEEPS MOVING IN ALPHA INITIAL DIRECTION. HELPFUL FOR CRACK INITI
kappa = (3-nue)/(1+nue); % for plane stress
First_rawdata_number = 1; % rawdata might be having many files, Give the first data file number, that is required to study
Last_rawdata_number = 1; % rawadata might be having many files, Give the Last data file number, that is required to study

%Parameters that change with each image are listed below
textFiles = dir('*.txt'); % give location of text files here
numfiles = length(textFiles); %
rawdata2 = cell(1, numfiles);
rawdata = cell(1, numfiles);
for k = 1:numfiles
    rawdata2{k} = importLoads(textFiles(k).name, 2, inf);
    importdata(textFiles(k).name);
    rawdata{k} = rawdata2{k}(12:end,:);
end



% LoadPoints Matrix
LoadPoint_x = zeros(numfiles,1);
LoadPoint_y = zeros(numfiles,1);
crackTipx = zeros(numfiles,1);
crackTipy = zeros(numfiles,1);

%angle at each point
alpha = zeros(numfiles,1);
alpha(1) = alphaInitial;

for k = First_rawdata_number:Last_rawdata_number
    ConstMatrix = zeros(2*N+1);
    fgMatrix = zeros(2*N+1,1);

    rawdatasize=size(rawdata{k});% Size of input data
    %Convert the input data into 2D matrix
    for row=1:rawdatasize(1)
%         x_c(rawdata{k}(row,2),rawdata{k}(row,1))= rawdata{k}(row,3);  % x coordinate system in mm (undeformed)
%         y_c(rawdata{k}(row,2),rawdata{k}(row,1))= rawdata{k}(row,4);  % y coordinate system in mm (undeformed)
        x_disp(rawdata{k}(row,2),rawdata{k}(row,1))= rawdata{k}(row,3);  % transformation
        y_disp(rawdata{k}(row,2),rawdata{k}(row,1))= rawdata{k}(row,4);  % transformation
        x_strain(rawdata{k}(row,2),rawdata{k}(row,1))= rawdata{k}(row,5);  % transformation
        y_strain(rawdata{k}(row,2),rawdata{k}(row,1))= rawdata{k}(row,6);  % transformation
    end

    % x_disp_rot is roation of co-ordinates. For reverse impact, the specimen has to be rotated by 180 degrees.
    % This variable handles this kind of rotation. After this it needs to be
    % transofrmed from xy to x'y' co-ordinates.
    x_disp_rot =  x_disp; %rot90(x_disp,-1);%
    y_disp_rot =  y_disp; %rot90(y_disp,-1);%
    ang_resultant = sqrt(x_disp_rot.^2+y_disp_rot.^2);

    %Contouring the angular deflection data
     c_level=[-20:0.03: 20]; %contour spacing % settings for y disp
    [ms,ns]=size(x_disp_rot);    % Total Full feild matrix size; ms is row and ns is column of the x_disp_Trans matrix
    [x,y]=meshgrid(0:1:ns-1,0:1:ms-1); %grid on which displacements are plotted

    % %parametrs for the contour graph
    % % hFig = figure(1);
    % % set(hFig, 'Position', [0 0 1050 1100])% figure(1);
    % % contour(x,y,(x_disp_Trans),c_level,'linewidth',1);
    % % contour(x,y,flipud(x_disp_rot),120,'linewidth',2);
    % % contour(x,y,flipud(ang_resultant),120,'linewidth',2);
    % % contour(x,y,(x_disp_Trans),40);
    % daspect([1 1 1]);
    % caxis([-0.005 0.005]);
    % colorbar;
    % % hold on;
```

```
    %
    hFig = figure(2*(k-First_rawdata_number+1)-1);
    set(hFig, 'Position', [0 0 2048 2048])
       contourf(x,y,flipud(x_disp_rot),c_level,'linewidth',1);
       shading interp;
        colormap([0 0 0; jet]);
    colorbar;
    caxis([-1.5 1.5]); % settings for y disp

if loadpoint == 0
    LoadPoint=ginput();  % Pick the load point from the screen
else
    LoadPoint=loadpoint;  % Pick the load point from the screen
end %end if loadpoint
    LoadPx1 =(LoadPoint(1));
    LoadPy1=(ms-LoadPoint(2));
    LoadPoint_x(k,1) = LoadPx1;
    LoadPoint_y(k,1) = LoadPy1;

    % Calculate alpha for each immage (from 2nd image onwards)
    crackTipx(k,1)=LoadPx1;
    crackTipy(k,1)=LoadPy1;
    if k == First_rawdata_number
        alpha(k) = alphaInitial;
    else
        alpha(k-1) = alphaFunction(k,First_rawdata_number,alphaInitial,crackTipx,crackTipy,sf,Step_Size,No_CRACK_TIP_ROTA);
    end

    % transofrmation from xy coordinates to x'y' co-ordinates(crack tip
    % co-ordinates)

    % for DIC, displacements are shifted to crack tip co-ordinate system.
    % i.e displacements at crack tip are zero.
    x_disp_rot_xc = x_disp_rot((round(LoadPy1)),(round(LoadPx1)));
    y_disp_rot_yc = y_disp_rot((round(LoadPy1)),(round(LoadPx1)));
    x_disp_CTCSYS = x_disp_rot - x_disp_rot_xc;
    y_disp_CTCSYS = y_disp_rot - y_disp_rot_yc;



    % for first point, they will be transformed based on alpha initial
    if k<=First_rawdata_number
        x_disp_Trans = (x_disp_CTCSYS)*cosd(alpha(k))+(y_disp_CTCSYS)*sind(alpha(k));
        y_disp_Trans = (x_disp_CTCSYS)*-sind(alpha(k))+(y_disp_CTCSYS)*cosd(alpha(k));
    else
    % for all other points, transformation will be done based on previous point
    % angle
        x_disp_Trans = (x_disp_CTCSYS)*cosd(alpha(k-1))+(y_disp_CTCSYS)*sind(alpha(k-1));
        y_disp_Trans = (x_disp_CTCSYS)*-sind(alpha(k-1))+(y_disp_CTCSYS)*cosd(alpha(k-1));
    end


    %co-ordinates shifted to crack tip location
    x_c = x; % x_c is a index, same as x
    y_c = ms-y-1; % y_c is a index same as y_c. However, its direction is in upward direction (w.r.t. co-ordinate system)
    x_rot_xc = x_c((round(LoadPy1)),(round(LoadPx1))); % index near the crack tip in x-direction
    y_rot_yc = y_c((round(LoadPy1)),(round(LoadPx1))); % index near the crack tip in y-direction
    x_CTCSYS = (x_c - x_rot_xc)*Step_Size*sf; % converted to mm
    y_CTCSYS = (y_c - y_rot_yc)*Step_Size*sf; % converted to mm
    % for first point, they will be transformed based on alpha initial
    if k<=First_rawdata_number
        x_Trans = (x_CTCSYS)*cosd(alpha(k))+(y_CTCSYS)*sind(alpha(k));
        y_Trans = (x_CTCSYS)*-sind(alpha(k))+(y_CTCSYS)*cosd(alpha(k));
    else
    % for all other points, transformation will be done based on previous point
    % angle
        x_Trans = (x_CTCSYS)*cosd(alpha(k-1))+(y_CTCSYS)*sind(alpha(k-1));
        y_Trans = (x_CTCSYS)*-sind(alpha(k-1))+(y_CTCSYS)*cosd(alpha(k-1));
    end


    y_disp_Trans_neighbours = zeros(5,5);
    x_disp_Trans_neighbours = zeros(5,5);
    y_disp_Trans_avg = y_disp_Trans;
    x_disp_Trans_avg = x_disp_Trans;
    edge_band = floor(avg_grid_size*0.5); % avoids finding neighbours near corners
     for row_index=1:ms
         for col_index=1:ns
             if ((row_index>edge_band && row_index<=ms-edge_band) && (col_index>edge_band && col_index<=ns-edge_band));
                 y_disp_Trans_neighbours = y_disp_Trans(row_index-edge_band:row_index+edge_band, col_index-edge_band:col_index+edge_band);
                 y_disp_Trans_avg(row_index,col_index) = mean(mean(y_disp_Trans_neighbours));
                 x_disp_Trans_neighbours = x_disp_Trans(row_index-edge_band:row_index+edge_band, col_index-edge_band:col_index+edge_band);
                 x_disp_Trans_avg(row_index,col_index) = mean(mean(x_disp_Trans_neighbours));
             end
         end
     end
```

```
% %
        hFig = figure(2*(k-First_rawdata_number+1)-1);
    set(hFig, 'Position', [0 0 2048 2048])
    c_level2=[-20:0.02: 20];
%     contourf(x,y,flipud(y_disp_Trans_dup),c_level,'linewidth',1);
%         contourf(x,y,flipud(y_Trans),c_level2,'linewidth',1);
          contourf(x_Trans,y_Trans,(y_disp_Trans_avg)); %whenever using x_Trans and y_Trans do not flip the matrix. Because, for every (x_Trans,y_Trans) pair there
          shading interp;
        colormap([0 0 0; jet]);
    colorbar;
    daspect([1 1 1]);
%     caxis([-0.00005 0.00005]);
      caxis([-1 1]);
%     caxis([-0.000001 0.000001]);
%     set(hFig, 'Visible', 'off');
%     saveas(hFig,sprintf('y_disp_Trans_%d.png',k));

%     close all;
end

close all
```

```
Index exceeds array bounds.

Error in DIC_FE_Read_Aramis_files (line 52)
    rawdatasize=size(rawdata{k});% Size of input data
                     ^^^^^^^^^^
```

Published with MATLAB® R2024b

```
% clc; close all; clear all;
% clearvars -except x_Trans y_Trans
clear BC NodesSet NodesMatrix

% NodesMatrix = csvread('Nodes.csv'); % Reads from ABAQUS input file format
NodesMatrix = importfile(Nodefn, 1, inf);% Reads from ABAQUS input file format
% fid = fopen('Nodes.csv', 'r');
% if fid == -1, error('Cannoten read file: %s', FileName); end
% Data = fscanf(fid, '%d, %d, %d ;;', [3, inf]);
% fclose(fid);

% NodesMatrix = readtable('Nodes.csv');
NodesMatrix_Size = size(NodesMatrix);
TotalNodes = NodesMatrix_Size(1,1);
N_sum = zeros(TotalNodes,1);
ufea = zeros(TotalNodes,1);
vfea = zeros(TotalNodes,1);
BC = zeros(2*TotalNodes,4);
% NodesSet = strings([2*TotalNodes,3]);
for NodeIndex =1:TotalNodes
% for NodeIndex =37208:37208
clear x1_matrix x1_loc_matrix x2_matrix x2_loc_matrix y2_matrix y2_loc_matrix y3_matrix y3_loc_matrix

    xfea = NodesMatrix(NodeIndex,2); yfea = NodesMatrix(NodeIndex,3); % Nodes from fea
    x_size = size(x_Trans);

    x1_count = 0;
    x2_count = 0;
    y_index = 1;

    for x_index = 1:x_size(1,2)
        if x_Trans(y_index,x_index)<xfea;
            x1_count = x1_count+1;
            x1_matrix(x1_count) = x_Trans(y_index,x_index);
            x1_loc_matrix(x1_count) = x_index;
        elseif x_Trans(y_index,x_index)>=xfea;
            x2_count = x2_count+1;
            x2_matrix(x2_count) = x_Trans(y_index,x_index);
            x2_loc_matrix(x2_count) = x_index;
        end
    end
    y2_count = 0;
    y3_count = 0;
    x_index = 1;
    for y_index = 1:x_size(1,1)
        if y_Trans(y_index,x_index)<yfea;
            y2_count = y2_count+1;
            y2_matrix(y2_count,1) = y_Trans(y_index,x_index);
            y2_loc_matrix(y2_count,1) = y_index;
        elseif y_Trans(y_index,x_index)>=yfea;
            y3_count = y3_count+1;
            y3_matrix(y3_count,1) = y_Trans(y_index,x_index);
            y3_loc_matrix(y3_count,1) = y_index;
        end
    end

    % this will not apply any loads at the edges of the fea nodes
    if (or(or(x1_count==0,x2_count==0),or(y2_count==0,y3_count==0)))
        continue
    end
    x1 = max(x1_matrix); x2 = min(x2_matrix);
    y2 = max(y2_matrix);
    y3 = min(y3_matrix);

    [x1,x1_loc] = max(x1_matrix(:)); [x2,x2_loc] = min(x2_matrix(:));
    [y2,y2_loc] = max(y2_matrix(:)); [y3,y3_loc] = min(y3_matrix(:));
    x1_loc = x1_loc_matrix(x1_loc); x2_loc = x2_loc_matrix(x2_loc);
    y2_loc = y2_loc_matrix(y2_loc); y3_loc = y3_loc_matrix(y3_loc);

    x3=x2;x4=x1;
    y1=y2;y4=y3;
    x3_loc=x2_loc; x4_loc=x1_loc;
    y1_loc=y2_loc; y4_loc=y3_loc;

%     u1= x_disp_Trans(y1_loc,x1_loc); v1= y_disp_Trans(y1_loc,x1_loc);
%     u2= x_disp_Trans(y2_loc,x2_loc); v2= y_disp_Trans(y2_loc,x2_loc);
%     u3= x_disp_Trans(y3_loc,x3_loc); v3= y_disp_Trans(y3_loc,x3_loc);
%     u4= x_disp_Trans(y4_loc,x4_loc); v4= y_disp_Trans(y4_loc,x4_loc);
    u1= x_disp_Trans_avg(y1_loc,x1_loc); v1= y_disp_Trans_avg(y1_loc,x1_loc);
    u2= x_disp_Trans_avg(y2_loc,x2_loc); v2= y_disp_Trans_avg(y2_loc,x2_loc);
    u3= x_disp_Trans_avg(y3_loc,x3_loc); v3= y_disp_Trans_avg(y3_loc,x3_loc);
    u4= x_disp_Trans_avg(y4_loc,x4_loc); v4= y_disp_Trans_avg(y4_loc,x4_loc);

    a = (x2-x1)/2; b = (y3-y2)/2;
```

```
    xi= (xfea-0.5*(x1+x2))/a ; eta=(yfea-0.5*(y3+y2))/b;

    N1 = 0.25*(1-xi)*(1-eta);
    N2 = 0.25*(1+xi)*(1-eta);
    N3 = 0.25*(1+xi)*(1+eta);
    N4 = 0.25*(1-xi)*(1+eta);

    N_sum(NodeIndex) = N1+N2+N3+N4;
    ufea(NodeIndex) = N1*u1+N2*u2+N3*u3+N4*u4;
    vfea(NodeIndex) = N1*v1+N2*v2+N3*v3+N4*v4;
    % write csv file
    BC(((2*NodeIndex)-1),1) = NodesMatrix(NodeIndex,1);
    BC(((2*NodeIndex)-1),2) = 1;
    BC(((2*NodeIndex)-1),3) = 1;
    BC(((2*NodeIndex)-1),4) = ufea(NodeIndex);
    BC((2*NodeIndex),1) = NodesMatrix(NodeIndex,1);
    BC((2*NodeIndex),2) = 2;
    BC((2*NodeIndex),3) = 2;
    BC((2*NodeIndex),4) = vfea(NodeIndex);

end
zeroNode_indices = find(BC(:,1)==0);
BC(zeroNode_indices,:) = [];
xlswrite(['BC' num2str(Looper) '.xlsx'],BC);
```

```
Error using textscan
Invalid file identifier. Use fopen to generate a valid file identifier.

Error in importfile (line 37)
dataArray = textscan(fileID, formatSpec, endRow(1)-startRow(1)+1, 'Delimiter', delimiter, 'EmptyValue' ,NaN,'HeaderLines', startRow(1)-1, 'ReturnOnError', false);
            ^^^^^^^^^^^^^^^^^^^^^^^^^^^^^^^^^^^^^^^^^^^^^^^^^^^^^^^^^^^^^^^^^^^^^^^^^^^^^^^^^^^^^^^^^^^^^^^^^^^^^^^^^^^^^^^^^^^^^^^^^^^^^^^^^^^^^^^^^^^^^^^^^^
Error in DISP_MAPPING (line 6)
NodesMatrix = importfile(Nodefn, 1, inf);% Reads from ABAQUS input file format
              ^^^^^^^^^^^^^^^^^^^^^^^^^^
```

Published with MATLAB® R2024b